Dynamic Adaptive Concurrent Multi-Scale Simulation of Wave Propagation in 3D Media

Nicola Bombace

Exeter College

University of Oxford

A thesis submitted for the degree of

Doctor of Philosophy

Hilary Term, 2018

Acknowledgements

My deepest gratitude goes to Prof. Nik Petrinic and Dr. Ettore Barbieri for their patient guidance during these years. The knowledge they shared and their constant encouragement have been invaluable to solve the technical challenges we encountered throughout this dissertation.

My thanks to Prof. Alan Cocks and Prof. Antoine Jerusalem for the good advices and stimulating conversations during our meetings. Thank you to all the people in the Impact Engineering team who have always challenged me to approach my research from both numerical and experimental aspects. Thank you, in particular, to Dr. Sascha Knell for constantly sharing with me his knowledge and research activity on dynamic simulations and Dr. Antonio Pellegrino for showing me different methodologies to model Split Hopkinson Bar experiments by means of Finite Elements.

Thank you also to Francesco De Cola, Simone Falco, Mattia Montanari and Antonino Parrinello for making this experience unique and being great friends during these years.

Finally, I wanted to thank my family. My wife, Francisca, not only for her constant and unconditional love that has been and will always be my strength, but also for being a brilliant scientist who has helped me with invaluable suggestions. My father and my mother who will always be next to me, every day, no matter how far I am from home. My sister Sara and my brother Luca for showing me that our bond does not know temporal and spatial limits.

Dynamic Adaptive Concurrent Multi-Scale Simulation of Wave Propagation in 3D Media

Nicola Bombace, Exeter College, University of Oxford
For the degree of D.Phil. in Engineering Science, Hilary Term 2018

...

Over the last decades the use of numerical simulations to characterize the response of real structures has proven to be a valid tool that can accelerate the design process. However, the correct interpretation of the mechanical behaviour including stress localisations and geometrical features, requires the adoption of fine discretisations that drastically increase the computational cost. Even when using one numerical description for the mechanichal representation of the structure (e.g. continuum mechanics), the use of concurrent adaptive multi-scale frameworks in which finer temporal and/or spatial discretisation scales are generated during computation within the regions of interest and coupled both spatially and temporally to the original coarse scale, can lead to drastic reductions of the computation times. In this context, the challenge is the formulation of a stable coupling between the discretisation scales, which avoids the generation and propagation of numerical artefacts such as spurious wave reflection. Moreover, the detection of the error in dynamic simulations based on the the popular super-convergent patch recovery technique, even if formally correct, requires a substantial computational effort, that can result in a bottleneck for the whole simulation.

Based on these current limitations, the conducted research was to develop a novel numerically efficient concurrent dynamic finite element framework which automatically detects the regions of interest and simulates them in a finer time and length scales. In particular, this thesis investigates the concurrent coupling between domains with the same numerical description (i.e. Finite Elements for fine and coarse scales), where a scale is defined as a computational domain which presents a finer/coarser

temporal and spatial discretisation. The first main contribution of this work is the formulation of an error estimator based on an hermitian interpolation of the kinematic variables that is local to each element. The proposed procedure, avoids the need for neighbour searches and resolution of complex systems of equations. Another key feature of this methodology is that it can be used to directly transfer the variables from the coarse to the fine scale, resulting in smooth strain and stress field without the use of a balance step. Another key contribution of this thesis is represented by the coupling methodology, formulated in terms of nodal forces over an evolving coupling volume. This novel formulation enforces the kinematic link between the scales over a volume defined as the set composed by the first neighbours of the elements highlighted for refinement. The resulting coupling can be evaluated explicitly at every node of the coupled domain, resulting in a procedure numerically efficient and easy to implement.

The properties of the framework are demonstrated both analytically and through a set of numerical simulations, using the one dimensional wave propagation in elastic rods for validation. Firstly, the proposed error estimator is compared against the analytical error showing similar rate of convergence. The above hermitian strategy is used to transfer the variables to the finer scales, where the equilibrium among internal, external and inertial forces is respected without the use of an intermediate balance step. Subsequently, parametric studies have demonstrated the paramount importance of suitable coupling lengths and weighting parameters to avoid the formation of spurious wave reflections.

The novel mathematical findings, expanded in the three dimensional space, result in the fundamental building blocks of a novel dynamic adaptive recursive concurrent multi-scale framework. The proposed implementation idealises the relationship among scales as parent-child in which one coarse scale can generate several child scales based on the implemented refinement criteria. The validation of the framework has been proven in reversible and irreversible settings. Finally, after the rigorous demon-

stration of the validity of the methodology future research lines are suggested, based on the versatility of the framework.

Contents

1 Introduction **1**

1.1 Background and motivation 1

1.2 Aim and objectives 3

1.3 Research strategy 4

1.4 Thesis outline 5

2 Literature Review **6**

2.1 Multi-scale modelling strategies for heterogeneous materials 6

2.1.1 Multi-scale modelling for static simulations 6

2.1.2 Multi-scale Modelling for dynamic simulation 12

2.1.3 Adaptive concurrent multi-scale frameworks 20

2.1.4 Applications for heterogeneous materials 26

2.2 Concluding Remarks 27

3 A novel dynamic adaptive concurrent multi-scale framework for wave propagation **29**

3.1 Strong form of the dynamic wave propagation in continuum media . . 29

3.1.1 Weak form and fully discretised Finite Elements 30

3.2 A novel efficient adaptive framework for the coupling of differently discretised domains 34

3.2.1 Determination of the critical time step for the novel framework 39

3.2.2 Resolution Algorithm 42

3.2.3 Stability analysis 45
3.2.4 Error estimation 47
3.2.5 A local spatial error estimator based on hermitian interpolations 47
3.2.6 Mesh kinetic and kinematic data transfer based on hermitian interpolation 50
3.2.7 Adaptive Framework 53
3.3 Verification 55
3.3.1 Analytical Approach 56
3.3.2 Hermitian interpolation based error estimator for one-dimensional mesh 58
3.3.3 Coupling Properties 62
3.3.4 Parametric study of the coupling properties 65
3.3.5 Adaptive dynamic concurrent multi-scale 1D framework 70
3.4 Concluding remarks 76

4 A novel dynamic adaptive concurrent multi-scale framework for 3D wave propagation in homogeneous media 81

4.1 Uniform strain hexahedron element for explicit simulations 81
4.2 A local spatial error estimator based on 3D hermitian interpolation . 84
4.3 An efficient refinement algorithm for 3D hexahedral meshes 88
4.4 A novel 3D framework for dynamic adaptive concurrent multi-scale simulations 91
4.5 Applications 93
4.5.1 Square bar without lateral inertia 93
4.5.2 Lateral Inertia Effect in thick square bar 100
4.5.3 Slender Circular bar 107
4.5.4 Dynamic plastic localisation in dog-bone specimen 116
4.6 Concluding Remarks 122

5 Conclusions and further work **129**

5.1 Summary 129

5.2 Contributions 131

5.3 Limitations and proposed further work 134

A Hermitian interpolation in three dimensions **137**

A.1 Code implementation and verification 137

List of Figures

2.1 Principle of separation of scales. The two scales are fully separated when the condition $L_v >> \ell_v$ is respected. 7

2.2 Computational homogenisation scheme (adapted from [1]). The macro-scale deformation gradient $\boldsymbol{F}_M$ is transferred to a micro-scale BVP (Boundary Value Problem). The micro-scale communicates back the stress and the tangent stiffness matrix. 8

2.3 Non overlapping concurrent multi-scale Framework for Concrete. In this case a micro-scale domain is defined a priori to simulate the crack evolution. Reprinted with permission from [2] 10

2.4 Non overlapping concurrent multi-scale Framework for Composites, reprinted with permission from [3]. In composites the crack propagation is a result of different competing mechanism, that can only be corrected represented at the fibre-matrix level. 10

2.5 Overlapping Arlequin Concurrent multi-scale Framework. The fine scale Ω^{fs} and Ω^{cs} communicate through a transition layer of width ℓ_0. The blending of the energies among the scales is ensured by a weighting parameter $w = \frac{l}{\ell_0}$. reprinted with permission from [4]) 12

2.6 Principle of separation of scales for dynamic events. In dynamics a third scale λ connected to the boundary condition is introduced. The separation of scales is verified when $\lambda_v >> L_v >> \ell_v$. 13

2.7 Algorithm for time scale coupling, adapted from [5]. The one-dimensional mesh is divided in three sets. A purely explicit (blue), a purely implicit (orange) and a mixed implicit/explicit (green) domain. 13

2.8 Comparison between GC and PH framework (reprinted with permission from [6]). While the GC framework computes the Lagrangian multiplier at each micro time-step, the PH framework computes it only at macro time-steps, and interpolates this result on the micro-scale. Such methodology of the PH framework avoids the dissipation present in GC. This effect is achieved, in the PH framework, by coupling the coarse at the fine scale only at coarse time-steps, while in the classical GC the two domains are coupled at every fine time-step. . . 16

2.9 MST technique described in [7]. The domain is divided in a fine scale (blue) a coarse scale (green), and a transition layer (shaded). While at the interface the micro and macro scale communicate using the GC framework, in the transition layer the material properties are weighted similarly to the Arlequin method.(reprinted with permission) 17

2.10 Adaptive Concurrent Multi-scale Framework, reprinted with permission from [8]. In this case the crack propagation in composites is adaptively represented using different scales of approximation. 21

2.11 Data transfer procedure for integration point variables reprinted with permission from [9]. Firstly, the integration point variables are transferred on the nodes using the interpolation functions a). Subsequently using the same interpolation functions the interpolated nodal quantities are re-interpolated on the nodes of the new mesh b). Finally, such quantities are interpolated on the integration points of the new mesh c). 25

3.1 Domains Definition for strong form of dynamic problem 30

3.2 Domains definition in weak form of the Arlequin Model. The body Ω is split in three partitions: a coarse scale Ω_M, a fine scale Ω_m and a coupling domain Ω_c 34

3.3 Schematic representation of the recovery technique presented in [10], for one dimensional element with one integration point. The original stress σ^h is discontinuous at the nodal position. A continuous post-processed stress can be obtained averaging the contributions coming from different elements resulting in σ^*. At every integration point, the error, $\widetilde{e}_\sigma$, is defined as the difference between the two stresses. 48

3.4 Central difference temporal discretisation on the right. At every moment of the simulation, the solution is propagated from t^{n-1} to t^n. The velocities are always half time-step ahead of the accelerations. On the left, the multi-scale time stepping scheme proposed is depicted, for a refinement factor of 2. At every macro time-step the stresses, displacements and velocities at time t^{N-1} and $t^{N-\frac{1}{2}}$, are interpolated on the micro scale. Once the interpolation is complete, the micro-scale is updated 2 times and the corrective forces are sent back to the macro-scale, where a new $v_M^{N+\frac{1}{2}}$ is computed. 51

3.5 Comparison between hermitian and linear interpolation for refinement, in linear elastic elements. When using linear shape functions for the interpolation of the macro-displacements (blue arrows), the resulting elastic strain is constant over the micro-elements that share the same macro-element domain. When using hermitian shape functions, such situation is avoided, because of the use of nodal derivatives (orange arrows) resulting in a better interpolation of the elastic strain on the micro-mesh. 52

3.6 Transition of elements from macro to micro scale based on error detection. At every coarse time-step the error of every element is compared against a user input threshold. If any element has a high error it will be selected for refinement. The neighbouring elements of the original flagged ones are used for coupling purposes. 54

3.7 Reference Problem Configuration. A slender bar of length L, is subjected to a velocity boundary condition $V(t)$ while is free on the opposite face 56

3.8 Analytical solution to the elastic one-dimensional wave propagation problem. At any point in time the solution is the combination of a forward and a backward travelling wave 57

3.9 Element configuration for computation of error. The central node 2 can recover its nodal strain from its neighbouring elements. 58

3.10 Representation of the trapezoidal (left) and sinusoidal (right) applied boundary conditions. 60

3.11 Rate of convergence for different error estimators and trapezoidal boundary condition at $t = 0.8 * \frac{L}{c}$. The hermitian error estimator presents the same convergence rate of the ZZ estimator and is close to the analytical error on the considered mesh. 61

3.12 Rate of convergence for different error estimators and sinusoidal boundary condition at $t = 0.8 * \frac{L}{c}$. The hermitian error estimator presents the same convergence rate of the ZZ estimator and is close to the analytical error on the considered mesh. 62

3.13 Bar Coupled Model. The slender bar is partitioned a priori in a coarse Ω_M, fine Ω_m and coupling domain Ω_c 63

3.14 Elastic wave propagation at t= $0.5\frac{L}{c}$ for coupled model. The fine scale domain (left) is able to represent the low and high frequency content of the velocity boundary condition applied. 66

3.15 Elastic wave propagation at t= $0.8\frac{L}{c}$ for coupled model. The coarse scale domain (right) can only represent the low frequency content of the velocity boundary condition applied. However the high frequency is mostly dissipated through the coupling condition. 67

3.16 Evolution of the total energy for the coupled problem. The micro-scale total energy is initially zero, then it reaches a maximum and decreases when the energy is transferred to the coarse scale domain. The high frequency content of the energy is dissipated, but its contribution to the total energy is negligible. 68

3.17 Ratio of the Energy Spectral Density (ESD) of the dissipated and total power, for linear coupling and 16 coarse scale elements in the coupling zone. The dissipation is more important at frequencies closer to the cut-off frequency of the coarse domain. 69

3.18 Elastic wave propagation at t= $0.8\frac{L}{c}$ for linear weighting function at different coupling length. When the coupling length is increased the fine scale domain presents less spurious oscillations. At the same the trapezoidal pulse is better transferred to the coarse scale domain. . . 70

3.19 Total energy in coarse and fine scale domain when using a linear weighting function and different coupling lengths. The amount of energy trapped in the fine scale domain is negligible compared to the total energy, however when using small coupling lengths, there is a stronger energy dissipation. 71

3.20 Energy dissipation index as defined in equation 3.94 for linear weighting function at different coupling lengths. Increasing the length of the coupling zone has a double beneficial effect. On the one hand, the low frequency content is retained, because of the smaller dissipation at higher coupling lengths, leading to a better transfer of energies between macro and micro scale. On the other hand, the high frequency content is more effectively dissipated resulting in the absence of spurious wave generation. 72

3.21 Elastic wave propagation at t= $0.8\frac{L}{c}$ for power law weighting function at different coupling length. When increasing the coupling length, the fine scale domain presents less spurious oscillations. At the same time the trapezoidal pulse is better transferred to the coarse scale domain. 73

3.22 Total energy in coarse and fine scale domain when using a power law weighting function and different coupling lengths. The amount of energy trapped in the fine scale domain is negligible compared to the total energy, however when using small coupling lengths, there is a stronger energy dissipation. 73

3.23 Energy dissipation index as defined in equation 3.94 for power law weighting function at different coupling lengths. Increasing the length of the coupling zone has a double beneficial effect. On the one hand, the low frequency content is retained, because of the smaller dissipation at higher coupling lengths, leading to a better transfer of energies between macro and micro scale. On the other hand, the high frequency content is more effectively dissipated with resulting in the absence of spurious wave generation. 74

3.24 Elastic wave propagation at t= $0.8\frac{L}{c}$ for power law and linear weighting function using the same coupling length of $8^{*}\ell_M^e$. The use of the power law weighting function decreases the amount of spurious wave reflection and transfers more accurately the trapezoidal pulse at the coarse scale. 75

3.25 Total energy in coarse and fine scale domains when using power law and linear weighting functions. The use of the power law weighting function transfers more accurately the energy at the macro-scale domain, resulting in less energy dissipation. 75

3.26 Comparison of conventional and multi-scale analysis for trapezoidal pulse case. The multi-scale simulation presents qualitatively a smaller numerical error. 77

3.27 Comparison of conventional and multi-scale analysis for trapezoidal pulse case after the reflection from the free boundary. The simultaneous effect of data transfer and coupling does not affect the shape of the wave. 77

3.28 Comparison of conventional and multi-scale analysis for sinusoidal pulse case. The multi-scale simulation presents qualitatively a smaller numerical error. 78

3.29 Comparison of conventional and multi-scale analysis for sinusoidal pulse case after the reflection from the free boundary. The simultaneous effect of data transfer and coupling does not affect the shape of the wave. 78

3.30 Comparison of the error in the case of conventional and multi-scale simulation for trapezoidal pulse computed from analytical solution. The error of the multi-scale simulation is sensibly reduced. 79

3.31 Comparison of the error in the case of conventional and multi-scale simulation for sinusoidal pulse computed from analytical solution. The error of the multi-scale simulation is sensibly reduced 79

4.1 Configuration of hexahedron 8-nodes element in parent element domain. 82

4.2 Derivation of the approximation of the derivative terms in the vector $\mathbf{\Phi}$ for the node I. Employing a central difference scheme, an approximation for such terms can be computed only considering the neighbouring nodes. 88

4.3 The refinement procedure for 3D elements generates shared nodes between the original elements. This condition does not arise in 1D mesh. 89

4.4 Refinement procedure proposed in [11] where different element templates are used to generate a conforming mesh. 90

4.5 Schematic representation of the refinement algorithm proposed. The flagged elements (a) are firstly refined in their parent element domain (b), and then mapped on the deformed configuration (c) 91

4.6 Representation for the proposed adaptive concurrent multi-scale framework. The coarse scale Ω^M generates two micro-scales Ω^{m^1} and Ω^{m^2} that communicate only with their parent domain (the communication is represented by the dashed arrows). The child/fine scales can recursively generate finer domains, in this case Ω^{m^2} is the parent of Ω^{m^3}, which employ the same communication scheme. 93

4.7 Flowchart for the proposed adaptive concurrent multi-scale framework. The coarse scale Ω^M generates two micro-scales Ω^{m^1} and Ω^{m^2} that communicate only with their parent domain (the communication is represented by the dashed arrows). The child/fine scales can recursively generate finer domains, in this case Ω^{m^2} is the parent of Ω^{m^3}, which employ the same communication scheme. 94

4.8 Geometry of the square cross sectional bar. 95

4.9 Case of square bar without lateral inertia. Comparison between the mono-scale and multi-scale spatial distribution of σ_z at $t = 0.0789$ ms a) and $t = 0.1407$ b). The yellow line represents the axis over which the velocities will be plotted. On the lateral plane the analytical solution for this problem, at the same time, is depicted. The micro-scale simulation is activated for the entire portion of the domain that is interested by the wave. Its extension is dictated by the macro-scale elements that present a high error together with their neighbours. . . 97

4.10 Configuration of the coupling parameter α for the refined mesh at $t = 0.0789$ ms. The coupling parameter varies linearly over the length of one macro-scale element. 97

4.11 Case of square bar without lateral inertia. Comparison of stresses for conventional and multi-scale simulation at t = 0.0789 ms 98

4.12 Case of square bar without lateral inertia. Comparison of velocities for conventional and multi-scale simulation at t = 0.0789 ms 98

4.13 Case of square bar without lateral inertia. Comparison of stresses for conventional and multi-scale simulation at t = 0.1407 ms. 98

4.14 Case of square bar without lateral inertia. Comparison of velocities for conventional and multi-scale simulation at t = 0.1407 ms. 98

4.15 Case of square bar without lateral inertia. Comparison between the kinetic energy for both the mono-scale and multi-scale simulations. The two curves show very similar trends meaning that the energy is globally the same. 99

4.16 Case of square bar without lateral inertia. Comparison between the elastic energy for both the mono-scale and multi-scale simulations. The two curves show very similar trends meaning that the energy is globally the same. 99

4.17 Comparison among the mono-scale fine simulation, and the coarse simulation at t = 0.05 ms. The coarse scale can not capture the magnitude of the particle velocity along the bar 101

4.18 Comparison among the mono-scale fine simulation, and the coarse simulation at t = 0.125 ms. After the wave rebound the coarse scale can not track the particle velocity along the bar. 101

4.19 Contour plot of lateral velocity for coarse (top) and fine (bottom) simulation at t = 0.05 ms. The macro-scale simulation cannot capture the lateral motion of the bar. 102

4.20 Contour plot of lateral velocity for fine mono-scale (top) and multi-scale (bottom) simulation at t = 0.05 ms. The two simulations show similar results. 102

4.21 Comparison among the multi-scale simulation and the mono-scale fine simulation at t = 0.05 ms. The elements flagged for refinement are the ones behind the wave front. 104

4.22 Comparison among the multi-scale simulation and the mono-scale fine simulation at t = 0.125 ms (after the reflection). At this time-step the whole bar has been flagged for refinement. 104

4.23 Plot of the proposed weights for the parametric study of the weighting function α_m. 105

4.24 Comparison among the multi-scale simulations for two different weighting parameters, namely α_m^C and α_m^L at t = 0.05 ms. The constant coupling shows a significant amount of spurious wave reflections. . . . 106

4.25 Comparison among the multi-scale simulations for two different weighting parameters, namely α_m^L and α_m^P at t = 0.05 ms. The two couplings show very similar performances without the generation of spurious waves. 106

4.26 Geometrical divisions for a section of a square circular bar. The cross section mesh is defined by the number of divisions in the square n_{sq} and the number of divisions on the diagonal n_{diag}. 108

4.27 Comparison of the axial stress along the bar at $t = 0.05ms$. The coarser mesh present a higher amount of numerical error when compared to the solution with a finer mesh. 109

4.28 Cross section of the refined geometry and coarse scale. The proposed refinement algorithm can efficiently refine complex shapes, however it cannot represent the real geometry. 109

4.29 Comparison of the longitudinal stress at the small refined scale (upper mesh) and the coarse scale simulation (lower mesh) at t = 6.36e-2 ms. The refinement criterion highlights the elements interested by the wave, and triggers a multi-scale simulation whose results are reported in the top half of the image. Since the finer mesh can capture with a better resolution the evolution of the longitudinal stress over the computational domain, it is respresented with a smoother variation when compared with the coarse scale simulation in the bottom half. . 110

4.30 Case of slender circular bar. Comparison of longitudinal velocities for conventional and multi-scale simulation at t = 2.53e-2 ms 112

4.31 Case of slender circular bar. Comparison of longitudinal velocities for conventional and multi-scale simulation at t = 6.37e-2 ms 112

4.32 Case of slender circular bar. Comparison of longitudinal velocities for conventional and multi-scale simulation at t = 8.91e-2 ms. 113

4.33 Case of slender circular bar. Comparison of longitudinal velocities for conventional and multi-scale simulation at t = 1.40e-01 ms. 113

4.34 Elastic Energy for the whole domain as function of time, in the case of a slender bar. The similar trends show that the multi-scale simulation is stable. 114

4.35 Kinetic Energy for the whole domain as function of time, in the case of a slender bar. The similar trends show that the multi-scale simulation is stable. 114

4.36 Comparison between multi-scale simulation and mono-scale fine simulation in terms of longitudinal velocities at $t = 6.37e^{-2}\ ms$. The two simulations show perfect agreement, confirming the validity of the proposed framework. 115

4.37 Case of slender circular bar. Comparison of longitudinal velocities for conventional and multi-scale simulation at t = 1.4e-1 ms. 115

4.38 Split Hopkinson Bar apparatus configuration. A tensile pulse is generated in the incident bar which loads the specimen. The transmission bar serves as momentum trap for the apparatus. 116

4.39 Specimen design for the simulation of dynamic plastic localisation in dog-bone specimen, with dimensions in millimetres (above). The specimen is pulled from one face while axially supported on the opposite face (below). 117

4.40 Smoothed applied boundary condition for dog-bone dynamic plastic localisation. 118

4.41 Coarse mesh for dog-bone specimen with $\ell_M = 0.7\ mm$. 118

4.42 Comparison between the normal forces at the two opposite faces of the dog-bone specimen. When $t > 0.05\ ms$ the two forces are equal and opposite, therefore the condition of dynamic equilibrium is achieved. . 119

4.43 Results of the coarse scale simulation of the dog-bone specimen at t = 0.2 ms. The maximum displacement in the z direction is of 0.44 mm (above). The maximum value of equivalent plastic strain is registered in the middle of the specimen with a value of 0.64 (below). 122

4.44 Results of the fine scale simulation of the dog-bone specimen at t = 0.2 ms. The maximum displacement in the z direction is of 0.4926 mm (above). The maximum equivalent plastic strain is registered in the middle of the specimen with a value of 0.8436 (below). 123

4.45 Evolution of the plastic wave over time, alongside the refined mesh. On the left side the elements of the coarse scale are flagged over time, and the boundaries of the highlighted area are used to enforce the coupling at the micro-scale through α_m. 123

4.46 Results of the multi-scale simulation of the dog-bone specimen at t = 0.2 ms. The maximum displacement in the z direction is of 0.506 mm (above). The maximum equivalent plastic strain is registered in the middle of the specimen with a value of 0.8421 (below). The differences with the fine mono-scale simulation are less than 2%. 124

4.47 Comparison of the multi-scale simulation of the dog-bone specimen at t = 0.2 ms. The figure is obtained computing for every integration point the difference of the plastic equivalent strain between the fine mono-scale simulation and the multi-scale simulation. 124

4.48 Flagging process of the coarse domain with different choices of the threshold parameter ϵ_*^P. Increasing the threshold value the multi-scale process starts later in time. Moreover the highlighted portion of the domain becomes smaller. 125

4.49 Results of the multi-scale simulations with different values of ϵ_*^P at t = 0.2 ms. The highlighted are for refinement is smaller at higher values of the threshold, however the accuracy of the simulation decreases. . . 126

4.50 Parametric study of the Threshold parameter for the multi-scale simulation. Small values of ϵ_*^P result in high computational cost and low error. On the other hand high values result in an error close to the coarse mono-scale simulation. The non linear behaviour of the error highlights at optimum value of the threshold value of 0.2. 127

A.1 Validation of the proposed hermitian interpolation scheme. The methodology is validated since the sum of proposed functions have a value of 1 on the vertices of the hexahedron. 140

List of Symbols

$\boldsymbol{a}$	acceleration
α	weighting parameter
$\boldsymbol{B}$	spatial derivatives of shape functions
$\boldsymbol{B}^H$	spatial derivatives of hermitian shape functions
β	Courant number
c	sound propagation velocity in medium
c_e	sound propagation velocity in element
$(\cdot)^c$	coupling quantity
$\boldsymbol{D}$	rate of deformation
$\boldsymbol{\Delta}$	matrix of derivatives operators
$d\Omega$	external boundary of body Ω
dV	infinitesimal volume in the body
dV_{el}	infinitesimal volume in element
$\boldsymbol{det}(\cdot)$	matrix determinant operator
$\delta(\cdot)$	variational operator
Δt	computational time-step
Δt_{crit}	critical computational time-step
E	Young's modulus
$\dot{E}_{int}$	rate of internal energy
$\dot{E}_{kin}$	rate of kinetic energy
$\dot{E}_{tot}$	rate of total energy
E_T	tangent Young's Modulus
$\boldsymbol{e_\sigma}$	exact error in stress
$\tilde{\boldsymbol{e}}_{\boldsymbol{\sigma}}$	approximated error in stress
$\tilde{\boldsymbol{e}}_{\boldsymbol{\epsilon}}$	approximated error in strain
$\tilde{\boldsymbol{e}}_{\boldsymbol{v}}$	exact error in velocities
ϵ	1-d strain
f	frequency
$\boldsymbol{f}^{ext}$	external forces
$\boldsymbol{f}^{int}$	internal forces
$\boldsymbol{f}^{corr}$	corrective forces
$\boldsymbol{\Phi}$	hermitian kinematic vector
$\boldsymbol{G}$	hermitian polynomial matrix
Γ_t	region of space where traction is assigned
Γ_v	region of space where velocity is assigned

$H^n(\cdot)$	Sobolev space of order n
$\boldsymbol{H}$	hermitian interpolation matrix
$\boldsymbol{\mathcal{H}}$	restriction of the hermitian interpolation matrix to one component
$\boldsymbol{I}$	identity matrix
$\boldsymbol{K^{tan}}$	Linearised stiffness matrix
$\boldsymbol{L}$	lagrange multiplier matrix
L_v	characteristic length of the structure
ℓ_v	characteristic length of the material
ℓ_e	characteristic length of the element
λ_v	characteristic length of excitation
λ	lagrange multipiers
$\check{\Lambda}$, $\mathring{\Lambda}$	square of eigenfrequencies
$\boldsymbol{M}$	mass matrix
$(\cdot)^M$	macro scale quantity
$(\cdot)^m$	micro scale quantity
$(\cdot)^{M\to m}$	macro to micro scale projection
$(\cdot)^{m\to M}$	micro to macro scale projection
$\boldsymbol{n}$	normal to a given direction
η	second component of the spatial coordinates
η	substitution variable in D'Alembert's method
$\bar{\boldsymbol{N}}$	shape functions
$\boldsymbol{\mathcal{N}}$	restriction of the shape function to one component
$\boldsymbol{N}_\lambda$	shape functions for lagrange multipliers
p	first component of the displacements
$\boldsymbol{p}^e$	first component of the displacement in one element
$\mathcal{P}_{tot}$	Fourier transform total power
$\mathcal{P}_{diss}$	Fourier transform dissipated power
P	sum of power contributions
P_{int}	internal power
P_λ	power associated to lagrange multipliers
P_{kin}	kinetic power
$\boldsymbol{Q}$	sum of internal and inertial forces
q	second component of the displacements
$\boldsymbol{q}^e$	second component of the displacements in one element
r	third component of the displacements
$\boldsymbol{r}^e$	third component of the displacements in one element
r_f	refinement factor
ρ	density
S	dissipation index energy spectral density
S_{tot}	energy spectral density of the total power
S_{diss}	energy spectral density of the dissipated power

$\boldsymbol{S}$	compliance matrix of the material
$\boldsymbol{\sigma}$	stress matrix
$\boldsymbol{\sigma_0}$	initial stress
σ_{Y0}	yield stress
t	time
T	maximum time of interest
$\boldsymbol{t}$	assigned traction
$\boldsymbol{U}$	unity vector
$\boldsymbol{u}$	displacement
$\boldsymbol{v}$	velocity
$\widehat{\boldsymbol{v}}$	assigned velocity
$\mathcal{V}_0$	space of velocity test functions
$\boldsymbol{X}$	initial spatial configuration
X	first component initial spatial configuration
$\boldsymbol{\mathcal{X}}$	hermitian constant parameter matrix
$\boldsymbol{x}$	present spatial configuration
x	first component present spatial configuration
$\boldsymbol{\xi}$	spatial coordinates in parent element domain
ξ	first component of the spatial coordinates in parent element domain
$\underline{\xi}$	substitution variable in D'Alembert's method.
Y	second component initial spatial configuration
y	second component present spatial configuration
Z	second component initial spatial configuration
z	second component present spatial configuration
ω	eigenfrequency
Ω	generic body
ζ	third component of the spatial coordinates in parent element domain
$\bar{(\cdot)}$	trial parameter
$\check{(\cdot)}$	perturbed parameter
$\tilde{(\cdot)}$	weighted parameter

In this thesis bold symbols, such as $\boldsymbol{\sigma}$, represent a matrix, while italic symbols such as t, represent a scalar quantity.

Chapter 1

Introduction

This chapter introduces the proposed adaptive concurrent multi-scale framework which has been developed during the research which preceded writing this thesis. It summarizes the main relevant background information and the related motivation for the conducted research together with its objectives and research strategies before providing the thesis outline and justifying the invested effort by the corresponding literature review in the subsequent chapter.

1.1 Background and motivation

The reversible and irreversible behaviour of structures is strongly affected by the mechanical properties and arrangement of the single constituents of the material as well as by the geometry of the component and the loading regime. In quasi-static loading cases, where the main frequencies of excitation are well below the vibrational period of the structure, the body has enough time to adjust to the applied load and the external energy is balanced mainly by elastic/plastic mechanisms. At the same time, the excited spectrum is far from the one which triggers micro-structural failure modes, and as a consequence, the heterogeneous material responds as an homogenised medium. On the other hand, the application of dynamic loads generates significant localised inertia effects in which, at any time, the interaction among the stress waves travelling through the bulk could trigger different failure micro-mechanisms. The

macroscopic result of such loadings could be unexpected, such as the formation of damage away from the impact zone.

Even if seemingly different, these physical mechanisms are governed by the same fundamental principles of conservation of energy and momentum. Hence the Finite Element Method (FEM) provides a valid tool for the prediction and validation of different designs of structural components [12]. When simulating structural behaviour two different formulation of FEM are available: Implicit and Explicit. Both methods lead to similar solutions, but for events that have a short duration in time such as wave propagation, an explicit scheme is generally used, because is considerably more efficient (without sacrificing accuracy) than an implicit scheme. The biggest disadvantage of an explicit method is its conditional stability, based on a minimum time-step dependent on the smallest eigenvalue of a combination of mass and stiffness matrix. Therefore the computational time of an explicit simulation is not proportional to the total number of degrees of freedom but it is also connected to a smaller time-step.

However, fine and uniform meshes are required in a variety of applications. As an example, stress wave propagation simulations require the use of fine meshes to capture high stress gradients produced during wave propagation or impact, like the one which is generated during impact between two collinear rods. In this case, the analytical solution predicts an infinite gradient in the stress wave and real experiment show very sharp rising times of the pulse. Another example of limitations in the maximum characteristic length size can be found in the field of continuum damage mechanics. In particular the softening behaviour, after the onset of damage, is regularised to avoid mesh dependent results. However, the regularisation process leads to a maximum characteristic length above which the model will not dissipate the correct amount of energy. This non exhaustive set of limiting conditions for the coarsest mesh translates in very detailed computational meshes that hinder the simulation of real structures, due to their high computational cost.

Mesh adaptivity represents a well known and valid technique to lower the cost of large simulations. The main idea is that the mesh adapts in space, increasing the number of nodes in zones where the solution exhibits high concentration of error. Such technique has been developed and validated mostly for static problems, however it is still an open research field for dynamic applications. The main problems are connected to non physical responses associated with the juxtaposition of meshes with different characteristic lengths. In particular, at the interface between the two meshes the total energy is only partially transmitted from the coarse to the fine scale (and vice-versa) creating a numerical impedance [13]. At the same time, the high frequency content of the fine mesh that cannot be represented at the coarse mesh generates numerical oscillations known as spurious wave reflection [14]. Moreover, the coupling of different temporal scales among the various domains can lead to the generation and propagation of non-physical forces, whose accumulation over time can introduce artificial energy in the simulation, making it unstable [15].

Another important limitation in the coupling of dynamic simulations in which different time and length scales are represented concurrently, is connected to the quantification of a correct measure of the error, to automatically highlight the elements that need refinement. Finally, an open research field is represented by the definition of transfer operators for kinetic and kinematic data among the different meshes, that avoids numerical pollution and presence of unbalanced forces both at the fine and at the coarse scale.

1.2 Aim and objectives

Given the limitations of the standard formulation of the explicit finite element method, the aim of this doctoral thesis has been to develop an adaptive and explicit finite element framework, capable of simulating dynamic events at a considerably improved computational cost, by automatically identifying the sub-domains of interest and by solving the equations at the corresponding time and length scale. At the

same time the proposed framework should be able to concurrently couple different constitutive models and/or discretisation techniques, both in time and space, allowing simulations with better accuracy at the minimum computational cost. Based on the aims of this work, the specific objectives have been

- The definition of consistent down-scale and up-scale operators to transfer the solutions in terms of kinetic and kinematic quantities among different scales conserving the energy as well as the dynamic equilibrium.
- The formulation of a coupling constraint that does not generate numerical errors (i.e. spurious wave propagation and numerical impedance) at the interfaces between differently discretised domains.
- The formulation of an efficient a posteriori error measure based on local interpolation, to highlight/flag the elements that present high error.

1.3 Research strategy

The aims and the objectives of the thesis were guided by an extensive literature review on multi-scale simulation in dynamic environments and adaptive coupling of different time and scale discretisations. The proposed novel framework is first tested in a one-dimensional elastic environment, where the different challenges and salient aspects are highlighted and solved.

First of all, a novel refinement criterion based on a norm of the estimated error is proposed and verified for one dimensional constant strain under-integrated elements. Subsequently, the use of a downscaling interpolation scheme based on Hermitian functions enforces the continuity of strain as opposed to the use of standard FEM interpolation functions. The coupling between the different scales, at each fine scale time-step, is achieved through the computation of nodal coupling forces, which ensure that a weighted equality constraint of the velocities in a predefined coupling area is respected. The communication among the two scales is executed by introducing a

coupling volume, where at each fine scale time-step the two simulations exchange information.

Subsequently, the formulation is expanded from 1 dimension to 3 dimensions where the performances of the resulting framework are firstly assessed in an elasto-dynamic setting. Finally, to prove the generality of the proposed methodology, the framework is applied to irreversible processes observed and quantified in actual experiments.

1.4 Thesis outline

This thesis is organized as follows. Chapter 2 will introduce the relevant literature review in the field of adaptivity and coupling of different computational models, justifying the aim of the objectives of this work. Chapter 3 introduces a novel adaptive multi-scale framework applied to one-dimensional elastic wave propagation, with emphasis on the stability and accuracy of the overall scheme in which a new definition of the numerical error is implemented to identify the regions to be refined. The new framework is compared with conventional coupling methods, showing the improvement in terms of spurious wave reflection. The extension to three dimensions of the developed framework, is shown in Chapter 4, studying the wave propagation with different mesh topologies and alignments, where all the elements at the refined scales are generated on the fly. In the last part of Chapter 4 the framework is demonstrated to be valid in elasto-plastic dynamic problems, where strain localisation is observed in form of necking. Finally, Chapter 5 draws the major conclusions of this thesis and the further directions of this work.

Chapter 2

Literature Review

This chapter reviews previously proposed theories relevant to the development of a novel multi-scale dynamic framework. In particular three main areas are discussed: error estimation, transfer of data variables from coarser to finer mesh and coupling at the interface of differently discretised meshes. At the end of the chapter the key opportunities for improvements are highlighted, with particular attention to the case of transient phenomena.

2.1 Multi-scale modelling strategies for heterogeneous materials

2.1.1 Multi-scale modelling for static simulations

All materials, regardless of their nature, present heterogeneities. The possibility of representing such materials at a continuum level is based on the principle of separation of scales, as introduced in [16]. Figure 2.1 gives an intuitive perspective of this principle. In a generic static problem there are two scales involved, the characteristic length of the structure L_v and the smallest characteristic length of the material ℓ_v .

When $L_v >> \ell_v$ the scales are fully separated, hence the behaviour at the smallest scale can be homogenised at the coarsest scale. Such techniques are classified as hierarchical, and in the early steps of multi-scale simulations they relied on closed forms of analytical solutions, such as the pioneering work of Voigt [17] and Reuss [18].

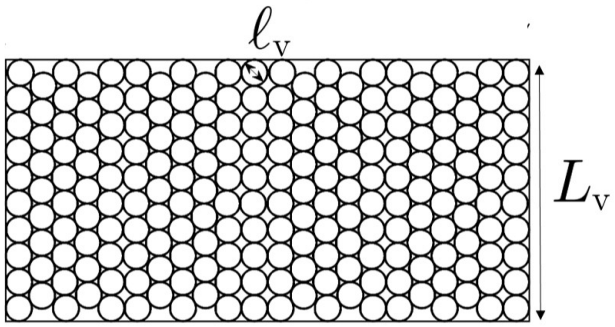

Figure 2.1: Principle of separation of scales. The two scales are fully separated when the condition $L_v >> \ell_v$ is respected.

These approaches have been extended to include different effects and several closed-form homogenization techniques have been proposed in this framework such as the Eshelby Mechanics [19], the Hashin-Strikman variational principle [20] and the self consistent method [21]. A comprehensive overview of hierarchical homogenisation methods can be consulted in the work carried out by Nemat-Nasser and Hori [22]. Hierarchical multi-scale approaches are very efficient, however they are restricted to relatively simple microscopic geometries and small strain analysis.

Semi-concurrent multi-scale approaches are used when the principle of separation of scales still holds but a closed form of the micro-mechanical solution is not available because of the geometry and/or loading effects. This technique is essentially based on the solution of nested boundary value problems, one for each scale. The main advantage of such methods is represented by the fact that the behaviour of the material at each scale is not assumed a priori. The basic idea of semi-concurrent multi-scale method is illustrated in figure 2.2. The approach relies on the use of a Representative Volume Element (RVE) defined as the minimum volume that can be used to determine the effective properties of a given material which can be adopted in a homogenised macroscopic problem [23]. The stress at each integration point of the macro-scale is computed solving a boundary value problem on the RVE at the micro-scale. The macro and micro scale boundary value problems have to be equivalent in the sense that the macro and micro mechanical energies have to respect the Hill-

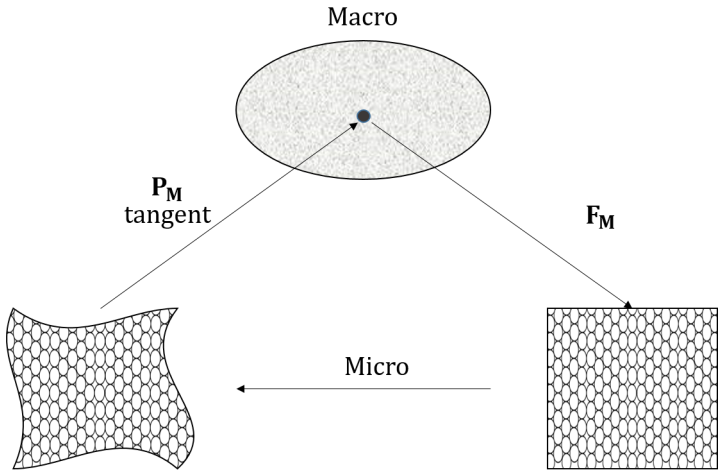

Figure 2.2: Computational homogenisation scheme (adapted from [1]). The macro-scale deformation gradient $\boldsymbol{F}_M$ is transferred to a micro-scale BVP (Boundary Value Problem). The micro-scale communicates back the stress and the tangent stiffness matrix.

Mandel principle [24]. Differently from hierarchical approaches, in semi-concurrent multi-scale methods there is a two way communication between the different scales. Examples of semi-concurrent multi-scale approaches can be found in [25–31] .

In cases in which damage and cracks evolve at the micro-scale, $L_{crack} \approx \ell_v$, the principle of separation of scales is violated, and standard homogenisation is no longer applicable as the formation and propagation of cracks break the periodicity of the micro-structure. The homogenisation is only valid locally because it is dependent on the local orientation of the crack at the micro-scale. The local solution near the crack tip is not representative of the general state of the material and therefore the RVE is substituted by a Microscrutural Volume Element (MVE). The main difference between RVE and MVE is the communication that is established among the scales. Bosco et al. in [32, 33], proposed a communication scheme where the macro-scale solution is based on the use of X-FEM enrichment [34, 35]. The presence of an enrichment, capable of representing discontinuities in displacement, allow the micro-scale solution to be up-scaled in presence of strain localisation regions. At the same time new boundary conditions are applied at the micro scale problem, to account for strain localization development at the micro-scale in a realistic direction. Finally the

micro-to-macro transition is based on a generalisation of the Hill-Mandel principle in case of strain localisation. Similarly, Loehnert and Belytschko [36] proposed the use of XFEM to track, at the macro-scale, the trajectory of the evolving micro-scale damage. Their approach uses two different MVEs: one that represents the localisation band, and another from which the continuum behaviour is extracted. Semi-concurrent methods in the presence of cracks offer little advantage with respect to concurrent multi-scale methods, mainly because the dimensions of the MVE are comparable with the coarse scale elements. A review of semi-concurrent approaches can be found in [37].

Another, more effective, approach that solves local effects in the presence of strong coupling between the scales, is the concurrent multi-scale framework. The main idea of this methodology is to circumvent the lack of scale separation by modelling simultaneously the different scales in the regions of interest of the computational domain that can adaptively grow or shrink depending on the damage evolution. The main idea of such framework is depicted in figures 2.3 and 2.4.

The computational domain is decomposed in different non-overlapping portions, based on the level of accuracy needed, and information are exchanged through the common boundaries. In [2], the damage caused by a crack growing in a concrete structure is simulated. The damaged zones represent explicitly the micro-structure while away from the crack tip, a homogenised constitutive model, based on the rule of mixtures is used. The enforcement of a displacement continuity condition at the common interface provides the communication among the scales. The approach used for the coupling of different meshes was first proposed by Farhat et al. in [38, 39] as Finite Element Tearing and Interconnecting (FETI), originally proposed for parallel implementation of the Finite Element Method. In this framework, different meshes and/or computational models share a common boundary on which a continuity on displacements is enforced using lagrangian multipliers. Despite the addition of new degrees of freedom, if the coupled area is small, the added computational time and

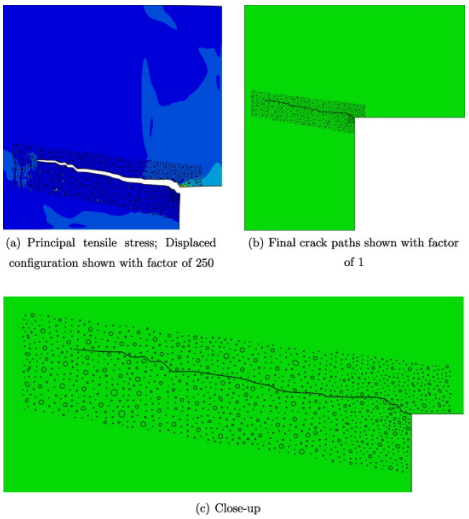

(a) Principal tensile stress; Displaced configuration shown with factor of 250

(b) Final crack paths shown with factor of 1

(c) Close-up

Figure 2.3: Non overlapping concurrent multi-scale Framework for Concrete. In this case a micro-scale domain is defined a priori to simulate the crack evolution. Reprinted with permission from [2]

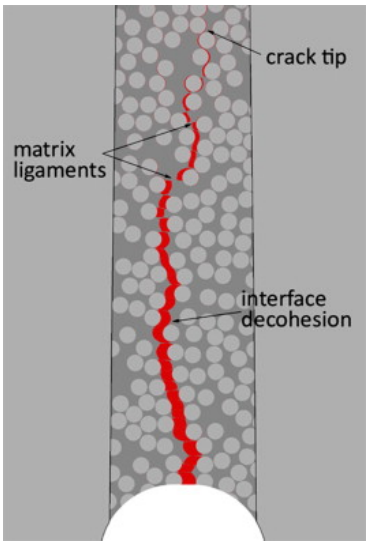

Figure 2.4: Non overlapping concurrent multi-scale Framework for Composites, reprinted with permission from [3]. In composites the crack propagation is a result of different competing mechanism, that can only be corrected represented at the fibre-matrix level.

storage requirement is minimum. The addition of new degrees of freedom can be avoided if the meshes are coincident at the interface, as proposed by Canal [3]. A homogenised model cannot represent the microscopic interaction among fibres and matrix in composite structures, therefore the zones where damage is expected are explicitly modelled. The concurrent multi-scale modelling of heterogeneous material in static conditions has been successfully applied in several works, for example [40–43].

Another class of concurrent multi-scale strategy decomposes the computational domain in several overlapping parts. The most known overlapping method is the Arlequin approach proposed by Ben-Dhia [44]. In addition to the micro and macro-scale domains, the Arlequin method proposes a transition layer as depicted in figure 2.5. In the overlapping region between the two domains the elastic energies of the macro and micro-scale are continuously blended through the use of a weighting parameter w. The coupling among the scales is established by adding to the variational statement a condition which ensures continuity of displacements, L2 coupling , or the continuity of both displacements and strains, H1 coupling, over the overlapping domain. The different couplings are enforced using lagrangian multipliers. Guidault and Belytschko in [45] conducted a study comparing different parameters of the Arlequin method for static problems. They found out that for the L2 coupling (in which continuity of displacements is enforced) the weighting parameter function has to be continuous, and surprisingly the lagrangian multipliers mesh has to be the coarser one. If these conditions are not met the solution will not converge to the correct one. On the other hand, H2 coupling (in which the continuity of displacements and strains is enforced) is more flexible. In this context the Finite Element Tearing and Interconnecting (FETI) method can be seen as a particular case of the Arlequin method, when $l_0 = 0$. It is clear that the Arlequin method is computationally more demanding than a FETI, given the same mesh, since it introduces more unknowns. However, in static formulation, it provides a flexible tool for the coupling of particle and continuum models as for example in [46–48].

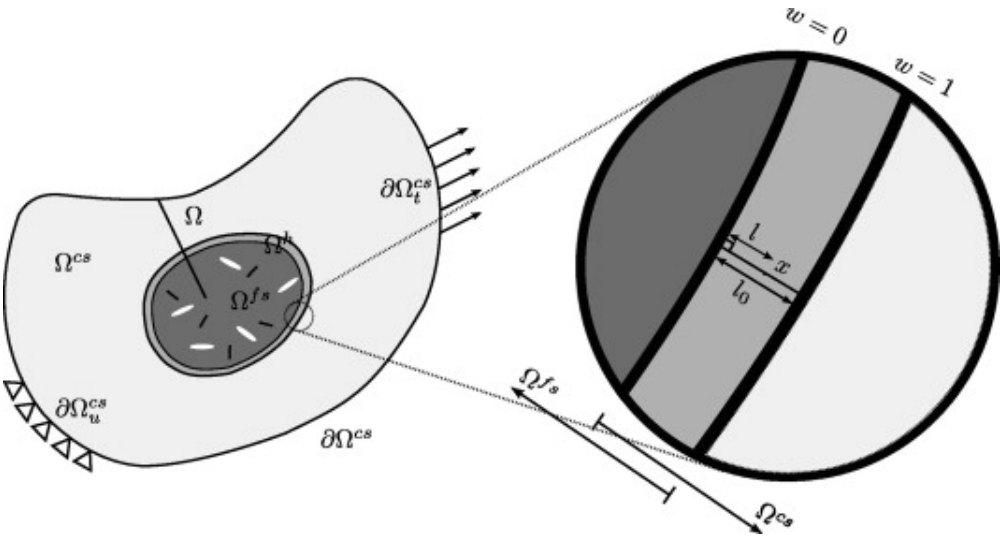

Figure 2.5: Overlapping Arlequin Concurrent multi-scale Framework. The fine scale Ω^{fs} and Ω^{cs} communicate through a transition layer of width ℓ_0. The blending of the energies among the scales is ensured by a weighting parameter $w = \frac{l}{\ell_0}$. reprinted with permission from [4])

2.1.2 Multi-scale Modelling for dynamic simulation

The simulation of dynamic events in heterogeneous materials involves an additional scale as depicted in figure 2.6. The new scale represented, λ, takes into account the spatial variation of the external applied forces over the structure. In particular the static condition can be obtained by imposing $\lambda >> L$. Therefore, in cases in which $\lambda_v >> L_v >> \ell_v$ either hierarchical or semi-concurrent methodologies can be used without any modification. When $\lambda_v \approx \ell_v$, local resonance effects, defined as micro-inertia, etc., take place in the micro-structure and classical homogenisation schemes lead to wrong results [49]. Different variations of the Hill-Mandel principle have been recently proposed to represent local resonance effects. In particular Pham et al. [50] and De Souza Neto [51] proposed an homogenisation scheme in which they demonstrate that the macro-scale stress is not only function of the deformation gradient, as in the classical scheme, but also on the macro-scale momentum. Recently Sridhar et al in [52] used the dynamic version of the Hill-Mandel principle from the previous works and solved the problem at the micro-scale, reducing the computational time at the micro-scale using the Craig Bampton Mode Synthesis [53].

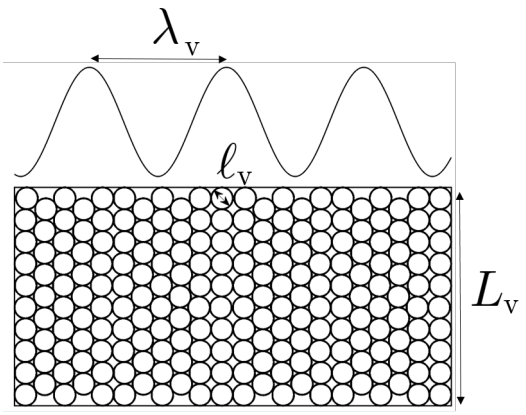

Figure 2.6: Principle of separation of scales for dynamic events. In dynamics a third scale λ connected to the boundary condition is introduced. The separation of scales is verified when $\lambda_v >> L_v >> \ell_v$.

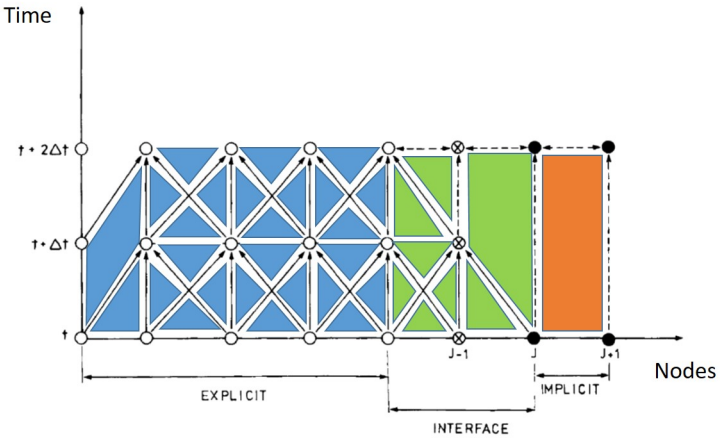

Figure 2.7: Algorithm for time scale coupling, adapted from [5]. The one-dimensional mesh is divided in three sets. A purely explicit (blue), a purely implicit (orange) and a mixed implicit/explicit (green) domain.

As for the static cases where the separation of scales is violated, concurrent multi-scale schemes offer a better solution for the explicit simulation of the micro-scale at a minimum computational cost. Dynamic problems are discretised both in space and time, and different frameworks looked at one or both aspects simultaneously. Belytschko and Mullen [5] were the first to propose an implicit-explicit coupling in different domains, for the coupling of different time-scales. The basic idea is depicted in figure 2.7 for one dimensional constant strain elements. The whole mesh is divided in explicit, interface and implicit zone represented as blue, green and orange respectively. In this example the time-step of the implicit domain is twice as big

as the time-step of the explicit domain. Firstly the solution of the explicit and the interface portions of the domain is propagated from time t to time $t + \Delta t$. The flow of information is such that the solution of node $J - 1$, cannot be propagated with an explicit integration at the next time-step $t + 2\Delta t$. However, its kinematic quantities can be used to update explicitly the solution of node $J - 2$, from time-step $t + \Delta t$ to $t + 2\Delta t$. Once the solution of the whole explicit portion is updated to time $t + 2\Delta t$, the displacement of node $J - 2$ is used as boundary condition to update the implicit part of the domain. Mullen and Belytschko demonstrated in [54] the stability of the methodology. An interesting result of the paper is that the coupled solutions, even if stable, show numerical oscillations known as spurious wave reflection [13].

Belytschko et al. subsequently in [55] extended the technique for the temporal coupling of explicitly integrated domains, where the ratio among the time-steps is an integer number. In particular the domain with a bigger time-step is integrated first and the interface displacement are interpolated linearly, when requested from the smaller time-step domain. In a successive work Neal and Belytschko [56] proposed a framework in which the different explicit partitions of the domain have a non-integer time-step ratio. The basic idea underlying this subcycling procedure is the presence of a nodal time-step and associated nodal clock together with a master time-step and associated master clock. The master time-step is computed as the least common multiple of its nodal counterparts, and the master clock is advanced only when all nodal clocks are at the same time. The proposed framework, even if still presents spurious wave reflection at the interface among different domains, is shown to be stable.

However the analysis of such technique by Klinisky in [57] and Daniel in [15] show that the proposed subcycling algorithms are not stable in a classical sense. The subcycling techniques proposed by Belytschko et al, are in fact probabilistically stable, meaning that for problems with a big number of elements instability is highly unlikely. This effect is mostly caused by the generation and accumulation of unbalanced forces due to the interpolation and extrapolation of nodal values, and it is significant

for extreme time-step differences. Modification of the subcycling techniques using a modified trapezoidal rule for the update of the displacements and the velocities have been proposed in [58, 59]. Casadei et al. in [60], proposed an integer subcycling technique in which every element can use its own time-step. The elements are separated in different levels, and the presence of integer time-step ratios avoids the need for interpolation.

Another approach for the coupling of time and space length scales simultaneously comes from the direct extension of FETI (which in statics only couples length scales) to the dynamic case. The dynamic version of the FETI framework is known in literature as Heterogeneous Asynchronous Time Integrator (HATI). Farhat et al. [61] proposed a first extension of the FETI algorithm to transient dynamics. In this framework the interface between the different meshes share the same node position (as in subcycling techniques). Differently from subcycling, the continuity at the interface is imposed on the nodal velocity rather than the nodal displacement. The coupling is achieved, as in the static FETI, applying lagrangian multipliers, in iterative form. Gravouil and Combescure in [62], proposed a different resolution technique, GC framework, for the general formulation of HATI. In this work, it is demonstrated that, to achieve stability in multi time-step methods, the velocity needs to be continuous at the interface between the differently integrated domains. Their approach is based on a predictor-corrector strategy. First the coarse scale is advanced in time of one time-step, without considering the interface constraint. Subsequently the fine scale is updated, imposing the constraint condition between the fine scale velocity and the linear interpolation in space and time of the coarse scale velocities. As pointed out, the algorithm is stable but dissipative due to the linear interpolation of the velocities at the interface.

Prakash and Hjelmstad in [6] modified the GC framework, proposing a different resolution procedure for the interface lagrangian multiplier condition. The new framework, named PH after the authors, has the main advantage of not being dis-

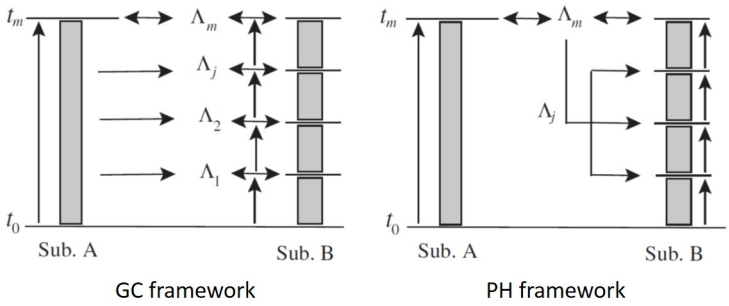

Figure 2.8: Comparison between GC and PH framework (reprinted with permission from [6]). While the GC framework computes the Lagrangian multiplier at each micro time-step, the PH framework computes it only at macro time-steps, and interpolates this result on the micro-scale. Such methodology of the PH framework avoids the dissipation present in GC. This effect is achieved, in the PH framework, by coupling the coarse at the fine scale only at coarse time-steps, while in the classical GC the two domains are coupled at every fine time-step.

sipative. The comparison among GC and PH is depicted figure 2.8. Suppose that two subdomains A and B communicate through a common interface. The subdomain (scale) A has a coarser time-step than the subdomain (scale) B. In the GC framework the interface condition is computed on the finer scale at each fine time-step of the simulation, while in the PH framework the interface continuity condition is computed only once when the times among the scales are the same. The resulting framework does not only preserve the energy of the computational domains but is also less computationally demanding. Mahjoubi, Gravouil, Combescure et al [63] extended the PH framework, to allow time coupling independently of the time-integrator. Differently from the PH, the new framework (MGC) solves the constraint in time in a weak sense. The Lagrangian multipliers are supposed to be constant over the coarse time scale, while they are discontinuous on the fine scale domain, and the integral over time of the lagrangian multipliers on the coarse and fine scale are imposed to be the same. The resolution of Lagrangian multipliers at the interface requires the resolution of a non linear system of equation, therefore an iterative solver is required, and this aspect of the computation is non desirable when two subdomains with explicit solvers are coupled in time and space. Nevertheless a faster convergence of the interface

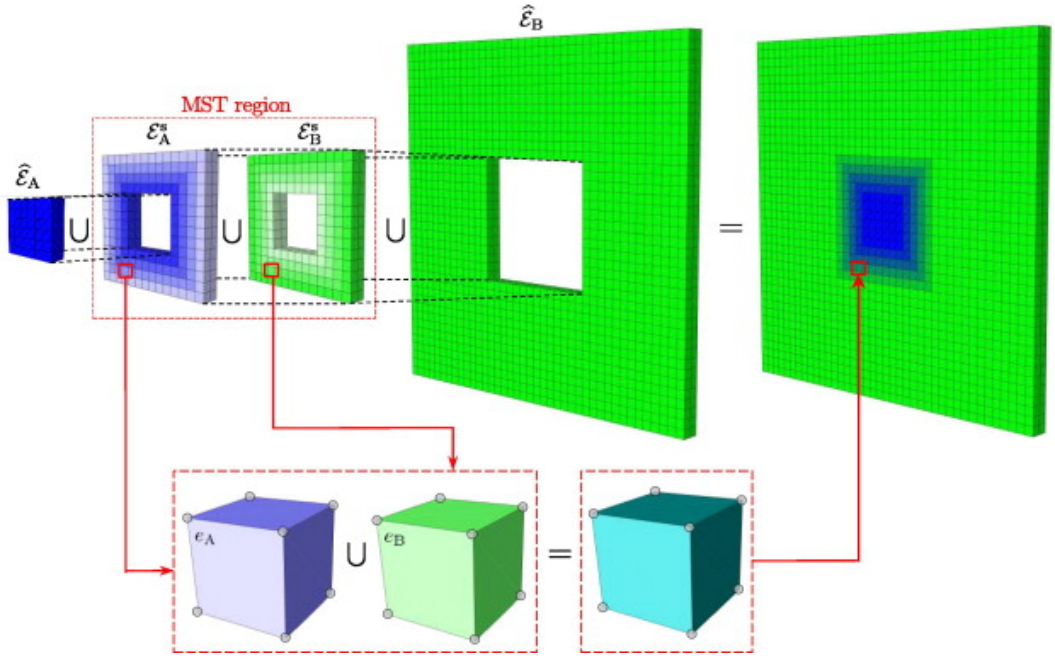

Figure 2.9: MST technique described in [7]. The domain is divided in a fine scale (blue) a coarse scale (green), and a transition layer (shaded). While at the interface the micro and macro scale communicate using the GC framework, in the transition layer the material properties are weighted similarly to the Arlequin method.(reprinted with permission)

problem can be achieved using Hermitian time interpolation of the velocity at the coarse scale at a finer time step as proposed by Bettinotti in [64]. In [65] Gravouil and Combescure point out that the coefficient matrix, to solve the non linear system for the Lagrangian multipliers is constant, and therefore, it can be pre-computed, but this condition holds only if the coupled domains are linear and elastic at the interface. On the other hand the juxtaposition of different computational models creates the propagation of numerical error, and in particular the formation an propagation of non-physical, spurious, waves due to the abrupt change in time and space resolution [13, 66, 67].

The most effective strategy to efficiently mitigate the spurious wave effect is to add a "transition" layer around the coupled interface. Such layer gradually adapts the wave as it travels from one domain to the next, effectively reducing, if not eliminating altogether, the formation of non-physical waves. Gigliotti and Pinho [7] proposed the use of a transition layer between two conforming meshes. The solid body is divided

in three parts as shown in figure 2.9: a micro-scale (blue), a macro-scale (green) and a region where the two of them coexist, called Mesh Superposition Technique (MST) Zone. In the MST zone the stiffness and mass properties of the elements are weighted with a parameter, that ensures partition of unity and energy blending in the overlap area. The definition of such parameter is exactly the same as in the Arlequin Method. The models are coupled at the interface using an explicit/implicit coupling in the GC framework. The simulations show a good level of accuracy compared with a micro mono-scale model, at a fraction of the total computational cost. The framework is however limited to conforming meshes, meaning that in the MST zone the micro and macro-scale mesh have to share the same nodes. Moreover, given the dynamic nature of the simulations it is not always possible to pre-determine the extension of the damaged area, and therefore adequately model the micro-scale.

Marchais et al [68], proposed a different one-dimensional approach for the construction of the transition layer. In the vicinity of the interface a filtering layer is constructed such that the part of the signal that cannot be represented by the coarser scale is damped out of the simulation. In particular at each time step of the fine scale, the solution at every node in terms of acceleration, displacement and velocity is split in two contributions: a macro contribution (representable by both the micro and the macro-scale) and a micro-scale contribution (representable only on the fine scale). The split of the solution is achieved using projection operators, that project the solution from the fine to the coarse scale and vice-versa. Such operators are constructed ad-hoc on the transition layer minimizing the difference between the micro and the projected macro scale kinetic energy. Several projection operators are proposed to ensure an easy computation of the resulting projection matrix. The difference between the projected micro-scale kinetic field on the coarse scale mesh and the actual field on the micro-scale is effectively the part of the micro-scale solution that cannot be represented on the macro-scale. The non representable field is damped out using a Perfectly Matched Layer (PML) [69, 70], a technique originally proposed to simulate

wave propagation in infinite medium. One dimensional elasto-dynamic simulations have shown that the technique is effective in annihilating the spurious wave reflection, providing at the same time a minimal energy loss thanks to the properly defined projection operator. The framework has not been extended to multiple dimensions, as research is still needed for the definition of projection operator and PML in three dimensions and on complex meshes.

Another approach to couple two or more computational domains with a transition layer is represented by the dynamic form of the Arlequin Method. Ghanem et al. [71] extended the static version of the Arlequin method to dynamics, with the possibility of coupling different time scale, while retaining the same spatial discretisation. The "gluing" condition over the overlapping zone is formulated in terms of displacement, and the lagrangian multiplier problem is solved every coarse scale time-step. While the stability of the framework is not demonstrated analytically, results are presented with ratios of fine to coarse scale time-step size of up to a 1000. Recently, Fernier et al. [72] proposed a stable Arlequin framework in which, differently from the previous works, attention is given to the stability of the gluing condition, while retaining the same time scale. In their work the explicit formulation of finite elements is used, and particular attention is given on the effect of the weighting parameter on the stability (CFL) condition, when an acceleration continuity over the gluing patch is enforced in the form of lagrangian multipliers. The major finding is that the use of the weighting parameter in the gluing zone, affects the stability condition decreasing the minimum stable time-step.

A dynamic form of the Arlequin method, known as bridging domain, capable of coupling different time and length scales has been proposed by Xiao and Belytschko [14] for the simulation of coupled particle and continuum models. The different communicating domains are both discretised using the explicit formulation of the finite elements with different spatial and temporal resolution. In the overlapping area the energies of the two domains are blended and a velocity continuity condition

is enforced using lagrangian multipliers, and are verified on the fine length scale mesh at each fine time-step. The resolution of the lagrangian multipliers is executed using the original coefficient matrix or its lumped form. The advantages of using the lumped form of the lagrangian multipliers are evident, since their values can be found without employing coupled system of equations. The most interesting feature of such lumping scheme is that it is more efficient in annihilating spurious wave reflections with respect to the consistent scheme. The influence of the coupling size and the weighting parameter function is also studied. The main drawback of the scheme is that it still needs to compute and lump a matrix whose size is equal to the number of fine nodes present in the coupling zone. Additionally, Talebi et al. [73] extended the bridging domain method to three dimensions.

In summary all the frameworks proposed for dynamic concurrent multi-scale simulation assume the presence of a fixed area of the whole computational domain where a more detailed model is needed. However it is not always possible to determine a priori the region of interest, therefore a number of simulations are needed to assess the influence of the size of the micro-scale with respect to the macro-scale. It is clear that especially in dynamics, the introduction of adaptivity, where the model estimates, on the fly, the size and the location of the micro-scale domain size is needed. The added complexities of a shrinking/expanding micro-scale domains, together with the issue of a moving interface boundary, highlighted in the next section, hinder the formulation of such adaptive concurrent dynamic multi-scale frameworks.

2.1.3 Adaptive concurrent multi-scale frameworks

Adaptive frameworks in concurrent multi-scale simulations do not assume the position and the size of a micro-scale domain a priori. The shape of the microscopic domain, instead, is computed on the fly based on the characteristics of the solution. Most of the work in this area concerns static analysis and the main challenges are highlighted in this section. Ghosh et al. [8] proposed an adaptive concurrent multi-

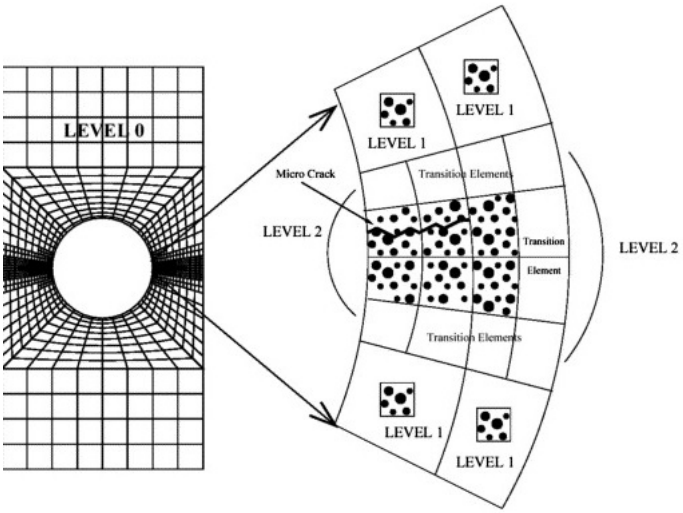

Figure 2.10: Adaptive Concurrent Multi-scale Framework, reprinted with permission from [8]. In this case the crack propagation in composites is adaptively represented using different scales of approximation.

scale framework in which the macro model adaptively transforms into a micro model through 4 levels in which different criteria are checked. In this framework three regions are identified. The first region (level 0) is the purely macroscopic region in which a hierarchical constitutive model is employed. The second region (level 1) is closer to the damaged area and is modelled through a semi-concurrent framework, while the localisation is explicitly represented at the third microscopic scale (level 2), surrounded by transition elements that gradually vary in size form level 2 to level 1.

The coupling in space among the scales is performed with a FETI engine. Particular attention in the framework is given to the transition criteria that are used to jump from one scale to the next. Such criteria can be based on the capability of the mesh employed to properly represent the steep gradients of displacements, and are employed in h or p-refinement schemes. In particular elements of the level 0 are refined where the traction jumps (at each element boundary) are bigger than the average traction jump computed on the whole mesh, as proposed in [74]. Other sets of criteria, instead of dealing with the quality of the mesh, assess whether the solution is exhibiting localisation and therefore other constitutive models need to be

used. Such criteria are used in the transition from level 0 to 1 and from level 1 to 2. Once the elements of level 2 are created, the state of stress and displacements history is simulated again to ensure that the energy is not dissipated during the switch of an element from level 1 to 2. Vernerey and Kabiri [75], proposed a similar scheme, however the proposed framework uses only macro and micro-scale. In this framework the coarse scale homogenised mesh is firstly refined employing a h-refinement scheme until the discretisation error is below a threshold. Such error is assessed by evaluating the first gradient of the displacement on the mesh an comparing it with the traction jumps among the element edges. When the size of the refined elements is comparable to the size of the RVE, the refined mesh will represent the explicit micro-structure. A similar technique has been proposed by Larsson et al. [76] in which the elements are refined in four different steps, using different constitutive models for composite material, starting from homogenised down to the actual micro-structure.

Greco et al. [77] proposed an adaptive FETI framework. Differently from the previous approaches the original mesh size is the same as one RVE. The criterion for which elements switch from a homogeneous constitutive model to the explicit micro-structure is based on the relative distance among the elements and the crack. The micro-structure is essential for tracking the correct crack path evolution, not well represented by using solely a homogeneous constitutive model.

Akbari Rahimabadi et al. [78] proposed a framework that accounts for both *discretisation* error (only dependent on the mesh coarseness) and *homogenisation* error (only dependent on the validity of the separation of scales principle). In particular the discretisation error of the mesh is evaluated adopting the Zinkiewicz-Zhu (ZZ) [10,79], error estimator. In the ZZ approach, an approximation for the exact solution is determined by defining a nodal continuous approximation of stress. This post-processed solution is subsequently compared with the original one, and their difference is used as an estimation of the discretisation error. Such error decreases when the nodal mesh density is increased. On the other hand, the homogenisation error is computed

based on the approach proposed by Temizer an Wriggers [80] who demonstrated that the second derivative of the displacement measures the deviation of the homogenised solution and the actual micro-scale. Differently from the discretisation error, the homogenisation error increases with the nodal mesh density. These two competing mechanisms determine whether an element needs to be simply refined or it should be switched to the next scale.

In dynamic analysis, together with discretisation and homogenisation error, another source of error has to be taken in consideration, namely the *temporal* error. This third source of error is generated from the discretisation of the temporal scale. Zinkiewicz [81] proposed a temporal error estimation technique for the Newmark time integrators. In particular Newmark time-stepping schemes are obtained expanding in Taylor series the value of the displacements ignoring third order terms. Therefore, Zinkiewicz proposed a technique to evaluate the third order derivative of the displacement in time to compute the temporal error. Another approach was proposed by Wiberg and Li [82], and it is considered as the temporal application of the ZZ estimator. The Newmark family time integrators present discontinuous acceleration between two time steps. The authors proposed a post-processing technique to obtain a continuous acceleration between two time steps and therefore estimate the temporal error from the comparison of the post-processed and original solution. Romero and Lacoma [83], proposed a more general approach that can be extended to any type of time integrators for all members of the Newmark integration family. The main idea is to construct an error estimation based on the explicit construction of a quadrature rule which can estimate the high order terms excluded in the time stepping procedure. The estimation of the error requires minimum computational cost and can be extended to different families of time integrators. Wiberg and Li [9] proposed a h-adaptive refinement technique for dynamic problems that simultaneously adapts the time-step and the mesh size (using the ZZ error estimator) to reduce the error in the solution. The resulting model, though, does not have multiple time scales, rather

the smallest time-step on the smallest mesh is used for the whole model. Moreover, since the meshes are simply refined and juxtaposed, the adaptive solution presents spurious wave oscillations. Yue and Robbins have proposed a similar approach for the estimation of temporal and special error and have applied their technique to elastic [84] and plastic dynamic [85] problems. Similarly to the precedent framework, a single time scale is adopted for the whole problem. The mesh size is adjusted using a s-refinement, where different meshes are superimposed and a continuity of displacement is enforced at the common boundary. The main advantage of this refinement scheme is that it does not need geometrical transition zones to adapt the fine mesh size to the coarse space. The main disadvantage of the framework is that it presents numerical spurious oscillations at the interface among different mesh.

The mitigation of numerical reflections due to the sudden change in mesh size can be achieved by using an adaptive formulation of the Arlequin/Bridging domain method. Gracie [86] proposed an adaptive formulation of the bridging domain method applied to the simulation of the propagation of dislocations. At every time step all the coarse scale elements that are at a certain distance from the dislocations are converted from coarse to fine scale. Moreover, at every time step a buffer zone is detected where a continuity of the velocity is enforced using the lumped formulation of the Lagrangian multipliers. The adaptive formulation of the bridging domain method has been extended by Moseley in [87], where in addition to the refinement criterion, a coarsening criterion is implemented to ensure computational efficiency. The main drawback of the proposed adaptive bridging domain framework is that a single time scale is used, meaning that the smaller time-step over the whole domain is used to advance all the nodal quantities in time. However, if the fine scale nodes are distributed over a small area, an improved computational time efficiency can be achieved using different time-steps for fine and coarse scales. This is because the effect of the time-step on the small fine scale portion of the domain, will not influence the time-step of the coarse scale domain. Another major drawback of the formulation

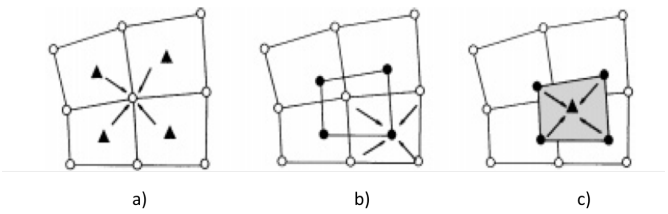

Figure 2.11: Data transfer procedure for integration point variables reprinted with permission from [9]. Firstly, the integration point variables are transferred on the nodes using the interpolation functions a). Subsequently using the same interpolation functions the interpolated nodal quantities are re-interpolated on the nodes of the new mesh b). Finally, such quantities are interpolated on the integration points of the new mesh c).

is the computation of a new mass matrix every time the velocity continuity condition is enforced over a new area.

A common issue of all the cited frameworks, both in static and dynamics, is what in literature is referred to as "data-transfer". Once the elements at the coarse scale have been flagged for refinement and have been refined, the coarse scale kinetic and kinematic variables have to be mapped from the old mesh to the new one. Peric et al. [88] pointed out that this process has to guarantee consistency in the energy transferred among the mesh, respect the equilibrium and minimise the diffusion of the interpolated state on the new mesh. One way to map the kinematic and kinetic variables is to apply the boundary conditions coming from the coarse scale on the fine scale and solve a boundary value problem for the newly generated mesh. This approach is more popular in static applications [74–78], and has the major drawback of being computationally expensive. Therefore a faster data transfer procedure that does not require the resolution of a boundary value problem, but instead makes use of interpolation functions to transfer nodal as well as integration point material state variables is required, as proposed in the work of Saksono and Peric [89] and Ortiz and Quigley [90]. The main idea of the procedure is to interpolate the nodal quantities on the new mesh using the standard definition of the interpolation functions. For the interpolation of the variables defined at the quadrature points a three stage procedure is adopted. Firstly the variables at the quadrature points are interpolated on the nodes

of the old mesh (utilising the ZZ procedure) as in figure 2.11a). Subsequently the obtained values are interpolated on the nodes of the new mesh 2.11b). Finally, using the interpolation functions of the new mesh the nodal quantities are transferred on the new integration points 2.11c). Even if the procedure is computationally effective it is highly diffusive due to the different interpolation stages involved. In the last type of data procedure approach, the value at one point (node or quadrature point) is computed from a higher order reconstruction of the field in the neighbourhood of this point. This type of remapping can be applied on unstructured meshes since it relies on clouds of points rather than on a mesh. Such algorithms have been applied in the works of Gracie [86] and Moseley [87]. Summarising it is clear that there is not a unique procedure for the transfer operation since every approach has its own advantages and drawbacks. For a review of data transfer operators consult the work of Bussetta et al. [91].

2.1.4 Applications for heterogeneous materials

Several frameworks mentioned in this section have been utilised in different applications involving evolution of damage for heterogeneous materials.

Gigliotti and Pinho in [7] applied the MST technique for the simulation of impact on a composite plate. The impact is simulated blending two different models: a detailed one with cohesive elements in the areas where delaminations are expected and a simplified discretisation without cohesive elements away from the damaged areas to simulate the bending of the plate. The models are coupled at the interface using an explicit/implicit coupling in the GC framework implemented in Abaqus. The simulations show a good level of accuracy compared with a micro mono-scale model, at a fraction of the total computational cost if the blending zone is far from the delamination boundaries. This effect can be mitigated using adaptive frameworks where the coarse scale is converted to micro-scale during the computation.

Another interesting applications regarding the study of damage in composite

plates are proposed in the work of Ghosh in [8], as depicted in figure 2.10. In particular a composite plate with a central hole is subjected to a tensile load until is damaged, and a crack appears in the domain. Similar applications are presented in Vernerey and Kabiry [75] Larsonn [76] and Greco et al. [77], where different RVEs and geometries are proposed for the validations of the frameworks. On the other hand, Akbari Rahimabadi in [78] studied the propagation of damage in plates of polycrystalline materials.

This range of applications justifies the use of adaptive frameworks for a more efficient simulation of damage in heterogeneous material, explicitly modelling the crack path only when and where needed in the computational domain. However, further research is needed to address several gaps, highlighted in the next section.

2.2 Concluding Remarks

From the previous section it is clear that there is a lack of a concurrent adaptive dynamic multi-scale framework that could couple different length scales and different time scales contrarily to [9, 84–87] where a single time-step is used for both fine and coarse scale domains. Moreover, the original formulation of the Arlequin [44] and bridging domain method [14], even if it is effective in the elimination of the spurious wave reflection at the interface of fine and coarse scale domains, it is computationally non-efficient in adaptive formulations since it requires the computation at each coarse scale time-step of the mass matrix and the lagrangian multiplier constraint matrix. Lastly, there is a gap in the literature on the formulation of an efficient transfer operator that can fulfil all the properties outlined in the work of Peric [88].

In the next chapter a novel framework will be proposed, able to capture the dynamic response of homogeneous materials through the coupling of subsequently refined scales. The main features of such framework will be the formulation of a novel and more efficient error estimator for the identification of zones that need refinement. Moreover, a novel coupling formulation for overlapping domains will be proposed and

analysed to ensure a stable framework. Lastly, particular attention will be given to the formulation of a consistent data transfer scheme. The framework will be validated in Chapter 3 with one-dimensional elastic wave propagation in rods. Subsequently three dimensional applications will be presented in Chapter 4, where the elastic wave propagation of complex mesh will be examined in the proposed multi-scale setting. Finally, the approach will be extended to irreversible wave propagation problems to explore the coupling using different constitutive models.

Chapter 3

A novel dynamic adaptive concurrent multi-scale framework for wave propagation

This chapter introduces a novel adaptive concurrent framework for dynamic problems. The first part of the chapter presents the mathematical formulation of the framework with particular attention to its novelties and its stability properties. Subsequently the novel methodology is validated by solving simple problems such as the propagation of elastic waves in slender bars, selected as reference problem. The performances of the novel framework are compared against non adaptive explicit finite formulations, showing improved accuracy.

3.1 Strong form of the dynamic wave propagation in continuum media

Let Ω be a body in the Euclidean space $\mathbb{R}^3$ and let $\partial\Omega$ be its boundary. At any instant in time, the deformation of the body is characterised by a smooth invertible function $\Phi(\boldsymbol{X}, t)$ which maps every point $\boldsymbol{X}$ from the initial configuration Ω_0 to the point $\boldsymbol{x}$ in the actual configuration Ω, as depicted in figure 3.1. Without loss of generality, neglecting the effect of body forces, denoting with $\boldsymbol{a}(\boldsymbol{x}, t)$, $\boldsymbol{v}(\boldsymbol{x}, t)$ and $\boldsymbol{u}(\boldsymbol{x}, t)$ the acceleration, velocity and displacement fields respectively, as well as the final time of interest T, the dynamic problem, as defined in [12] and [92] consists in

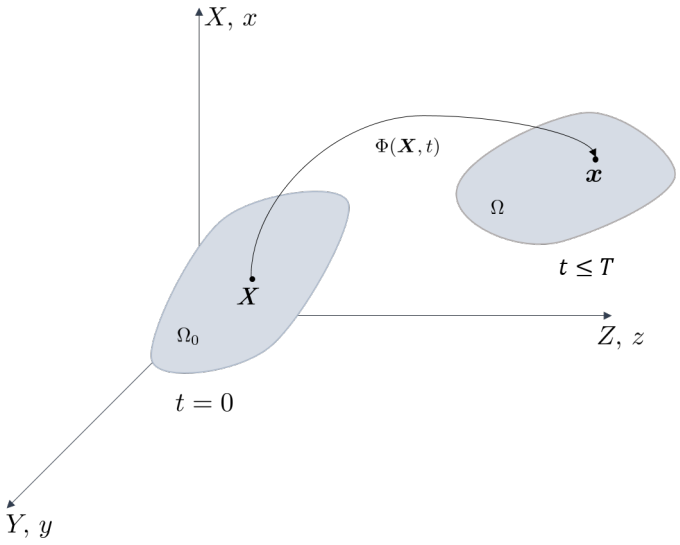

Figure 3.1: Domains Definition for strong form of dynamic problem

determining at every time $t \in [0, T]$, the velocity field and the Cauchy stress tensor $\boldsymbol{\sigma}(\boldsymbol{x}, t)$, for every point $\boldsymbol{x}$ of the body Ω such that:

$$\begin{cases} \rho \boldsymbol{a} = \nabla \cdot \boldsymbol{\sigma} \ \ in \ \ \Omega \ \ \mathrm{X} \ \ [0, T], & (3.1a) \\ \boldsymbol{v} = \widehat{\boldsymbol{v}} \ \ on \ \ \Gamma_v \ \ \mathrm{X} \ \ [0, T], & (3.1b) \\ \boldsymbol{\sigma} \cdot \boldsymbol{n} = \boldsymbol{t} \ \ on \ \ \Gamma_t \ \ \mathrm{X} \ \ [0, T], & (3.1c) \\ \boldsymbol{\sigma}(\boldsymbol{X}, 0) = \boldsymbol{\sigma}_0(\boldsymbol{X}) \ \ \boldsymbol{X} \in \Omega, & (3.1d) \\ \boldsymbol{v}(\boldsymbol{X}, 0) = \boldsymbol{v}_0(\boldsymbol{X}) \ \ \boldsymbol{X} \in \Omega, & (3.1e) \end{cases}$$

in which ρ is the material density and Γ_v and Γ_t are the portions of $\partial\Omega$, on which the stress and velocity boundary conditions are assigned to the values $\widehat{\boldsymbol{v}}$ and $\boldsymbol{t}$, respectively. Moreover, initial stress conditions $\boldsymbol{\sigma}_0(\boldsymbol{X})$ and $\boldsymbol{v}_0(\boldsymbol{X})$ are assigned over the body.

3.1.1 Weak form and fully discretised Finite Elements

The weak (variational) formulation of the dynamic problem is obtained as in [12], by multiplying equation 3.1a with a variation $\delta(\cdot)$ of a velocity *test function* field $\boldsymbol{v}$ and integrating it over the current configuration Ω, whose infinitesimal element is dV.

$$\int_{\Omega} (\rho \boldsymbol{a} - \nabla \cdot \boldsymbol{\sigma}) \cdot \delta \boldsymbol{v} \ \ dV = 0. \tag{3.2}$$

The test function $\boldsymbol{v}$ represents a field of velocities that are continuous over the domain and are zero on Γ_v, existing in the space $\mathcal{V}_0$.

$$\delta\boldsymbol{v} \in \mathcal{V}_0, \mathcal{V}_0 = \left\{\delta\boldsymbol{v}|\ \delta\boldsymbol{v} \in H^1(\Omega),\ \delta\boldsymbol{v} = 0\ on\ \Gamma_v\right\}, \tag{3.3}$$

in which $H^1(\Omega)$ is the Sobolev space of order 1. The integration by parts of the second contribution of the integral in 3.2 together with the vanishing property of the test function over the applied velocity boundary conditions leads to:

$$\int_\Omega \rho\boldsymbol{a}\cdot\delta\boldsymbol{v} + \boldsymbol{\sigma} : \delta\boldsymbol{D}\ \ dV - \int_{\Gamma_t} \boldsymbol{t}\cdot\delta\boldsymbol{v}\ \ dA = 0, \tag{3.4}$$

where $\boldsymbol{D}$ is the symmetric part of the gradient of velocity defined as $sym(\frac{\partial\boldsymbol{v}(\boldsymbol{x},t)}{\partial\boldsymbol{x}})$. Equation 3.4 represents the weak form of 3.1a, in which every term represents a variation of power with respect to $\boldsymbol{v}(t)$. In particular the different terms of 3.4 can be collected as:

$$\begin{cases} \delta P_{kin} = \int_\Omega \rho\boldsymbol{a}\cdot\delta\boldsymbol{v}\ \ dV, \\ \delta P_{int} = \int_\Omega \boldsymbol{\sigma} : \delta\boldsymbol{D}\ \ dV, \\ \delta P_{ext} = \int_{\Gamma_t} \boldsymbol{t}\cdot\delta\boldsymbol{v}\ \ dA, \end{cases} \tag{3.5}$$

in which δP_{kin}, δP_{int} and δP_{ext} represent the variation of kinetic, internal and external power, respectively and dA is the infinitesimal element of the surface Γ_t. Substituting 3.5 in 3.4 the final form of the weak form, known as the principle of virtual power is obtained as:

$$\delta P_{kin} + \delta P_{int} - \delta P_{ext} = 0. \tag{3.6}$$

The variational statement expressed in 3.6 can be solved by means of Finite Elements. To achieve this, the physical space Ω is substituted with a computational domain, generally referred as the "mesh", such that $\Omega \approx \sum_{e=1}^{N_{elem}} \Omega^e$, in which N_{elem} represents the number of elements in the computational domain. On the mesh, both the displacements and the test function velocities are expressed as:

$$\delta\boldsymbol{v}(\boldsymbol{X},t) = \boldsymbol{N}(\boldsymbol{X})\delta\boldsymbol{v}^e(t), \tag{3.7}$$

$$\boldsymbol{v}(\boldsymbol{X},t) = \boldsymbol{N}(\boldsymbol{X})\boldsymbol{v}^e(t), \tag{3.8}$$

in which $\delta\boldsymbol{v}^e$ and $\boldsymbol{v}^e$ represent the arrays containing the nodal values of the test function and the velocities grouped for each element, respectively. On the other

hand, $\boldsymbol{N}$ is the matrix of interpolation functions that are used to approximate the value of the kinematic variables between nodes. The semi-discretised weak form is obtained by substituting the expression for the approximated displacement and trial velocities from 3.7 in 3.4, and invoking the arbitrariness on the test function, leading to:

$$\boldsymbol{M}\boldsymbol{a} = \boldsymbol{f}^{\boldsymbol{ext}} - \boldsymbol{f}^{\boldsymbol{int}}, \tag{3.9}$$

where

$$\boldsymbol{M} = \sum_{e=1}^{Nelem} \int_{\Omega^e} \rho \boldsymbol{N}^T \boldsymbol{N} \ dV_{el}, \tag{3.10}$$

$$\boldsymbol{f}^{int} = \sum_{i=1}^{Nelem} \int_{\Omega^e} \boldsymbol{B}^T \boldsymbol{\sigma} \ dV_{el}, \tag{3.11}$$

$$\boldsymbol{f}^{ext} = \sum_{i=1}^{Nelem} \int_{\Omega^e} \boldsymbol{N}^T \boldsymbol{t} \ dV_{el}, \tag{3.12}$$

$$\boldsymbol{f} = \boldsymbol{f}^{ext} - \boldsymbol{f}^{int}. \tag{3.13}$$

In equation 3.11, $\boldsymbol{B}$ represents the matrix containing the derivative o the shape functions, with respect to the spatial variable $\boldsymbol{x}$. It is important to note that both the mass matrix $\boldsymbol{M}$ and the vector of forces $\boldsymbol{f}$ are evaluated over the current configuration. Also, when using the explicit form of Finite Elements, the mass matrix is diagonalised using lumping techniques such as the row sum technique [12].

The nodal acceleration $\boldsymbol{a}$ in equation 3.9 can be discretised in time using the central difference formula

$$\boldsymbol{a}^n = \frac{\boldsymbol{v}^{n+\frac{1}{2}} - \boldsymbol{v}^{n-\frac{1}{2}}}{\Delta t}. \tag{3.14}$$

Substituting equation 3.14 into 3.9, it is possible to obtain, the fully discretised explicit form of the Finite Elements, referred as the leap-frog marching scheme, as:

$$\boldsymbol{v}^{n+\frac{1}{2}} = \boldsymbol{M}^{-1}\Delta t \boldsymbol{f}^n + \boldsymbol{v}^{n-\frac{1}{2}}. \tag{3.15}$$

Given the lumped nature of the mass matrix and the central difference scheme used in time, the update of the nodal velocities from equation 3.15 can be accomplished without solving any system of equations, which is a great advantage in terms of computational time. The main drawback of such explicit scheme is that the solution

will grow unbounded if the time-step is too big. Such condition, known as conditional stability, sets the value for the maximum stable time step. As an example a stable time-step for linear elements is given by:

$$\Delta t = \beta \Delta t_{crit} \quad \Delta t_{crit} = \frac{2}{\omega_{max}} \leq \min_e \frac{\ell_e}{c_e}. \tag{3.16}$$

Equation 3.16 requires the time-step Δt for a whole mesh to be smaller of a critical value Δt_{crit}. The parameter β, known as Courant number, is generally smaller than 0.8, in practical FE simulations, to avoid potential instabilities growth due to complex phenomenon such as contact and damage. Even though the critical time-step should be evaluated through the use of the maximum eigenfrequency of the problem ω_{max}, a good approximation of the conditional stability is given by the inverse of the time that an elastic wave takes to travel the length of the smallest element in the mesh, computed as the minimum over the whole mesh of the length of an element ℓ_e and the sound propagation velocity in that element c_e. Finally the FE resolution of the dynamic problem is resumed in flowchart 1, and reported in [12, 92]. This will be referred in this thesis as *standard* explicit finite element formulation.

Flowchart 1. *Flowchart for standard explicit integration of Finite Elements*

1. *Initialise mesh: set* $\boldsymbol{v}_0$,$\boldsymbol{\sigma}_0$, $n = 0$, $t = 0$, *compute* $\boldsymbol{M}$
2. *Evaluate Nodal forces* $\boldsymbol{f}^n$ *from equation 3.13*
3. *Evaluate accelerations* $\boldsymbol{a^n} = \boldsymbol{M}^{-1}\boldsymbol{f}^n$
4. *Update Nodal Velocities* $\boldsymbol{v}^{n+\frac{1}{2}} = \boldsymbol{v}^{n+\frac{1}{2}-\eta} + \eta \Delta t \boldsymbol{a}^n$ *:* $\eta = \begin{cases} \frac{1}{2} & \text{if } n = 0 \\ 1 & \text{if } n > 0 \end{cases}$
5. *Overwrite nodal velocity for enforced boundary conditions*
6. *Update nodal displacements:* $\boldsymbol{u}^{n+1} = \boldsymbol{u}^n + \Delta t \boldsymbol{v}^{n+\frac{1}{2}}$
7. *Update counter and time*
8. *If simulation is not complete go to 2.*

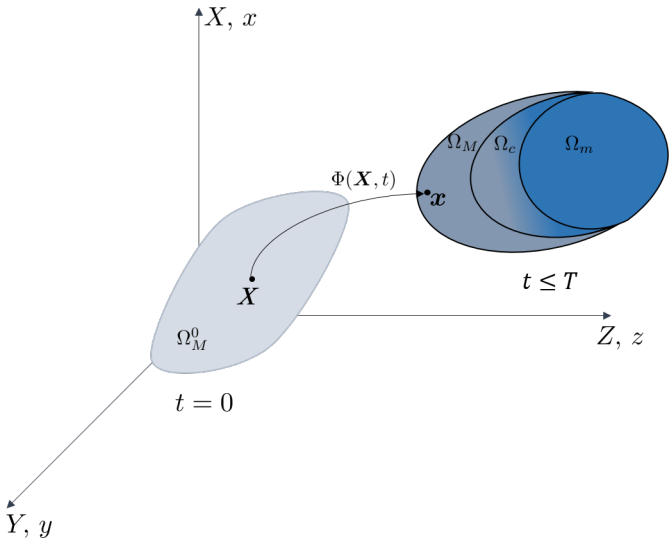

Figure 3.2: Domains definition in weak form of the Arlequin Model. The body Ω is split in three partitions: a coarse scale Ω_M, a fine scale Ω_m and a coupling domain Ω_c

3.2 A novel efficient adaptive framework for the coupling of differently discretised domains

As highlighted in the literature review section, the coupling of two discretisations, using different temporal and scale lengths, poses a challenge mainly linked with the generation of spurious waves at the coupled interface. The dynamic version of the Arlequin approach, that defines an overlapping area/volume between the two domains, is arguably the most effective methodology that can be found in open literature to couple different computational domains without generating spurious reflections. However, the high computational cost associated with the use of Lagrange multipliers over the coupling domain limits the use of this approach for relatively large simulations. In this section, a novel methodology, based on the expression of the coupling in terms of nodal corrective forces, is presented as an improvement of the dynamic Arlequin framework. In particular, the main advantage gained by the novel framework developed consists in avoiding assembling and inverting matrices connected to the coupling, substantially increasing the computational efficiency of the multi-scale approach, thus making it suitable for large simulations.

Let Ω_M, Ω_m and $\Omega_c = \Omega_M \cap \Omega_m$, in which the subscript M indicates the coarse (or macro) scale, m the fine (or micro) scale and c the coupling volume, be the partitions of Ω as represented in picture 3.2. The weak form of the dynamic coupled problem can be written as follows [71]:

$$\begin{cases} \int_{\Omega_M} \delta \boldsymbol{v}_{\boldsymbol{M}}^T \cdot \left(\alpha_M \rho \frac{\partial^2 \boldsymbol{u}_{\boldsymbol{M}}}{\partial t^2}\right) dV_M + \int_{\Omega_M} \frac{\partial \delta \boldsymbol{v}_{\boldsymbol{M}}^T}{\partial \boldsymbol{x}} : (\alpha_M \boldsymbol{\sigma}_{\boldsymbol{M}}) \, dV_M + \int_{\Omega_c} \delta \boldsymbol{v}_{\boldsymbol{M}}^T \cdot \boldsymbol{\lambda} \, dV_c = 0, \\ \int_{\Omega_m} \delta \boldsymbol{v}_{\boldsymbol{m}}^T \cdot \left(\alpha_m \rho \frac{\partial^2 \boldsymbol{u}_{\boldsymbol{m}}}{\partial t^2}\right) dV_m + \int_{\Omega_m} \frac{\partial \delta \boldsymbol{v}_{\boldsymbol{m}}^T}{\partial \boldsymbol{x}} : (\alpha_m \boldsymbol{\sigma}_{\boldsymbol{m}}) \, dV_m - \int_{\Omega_c} \delta \boldsymbol{v}_{\boldsymbol{m}}^T \cdot \boldsymbol{\lambda} dV_c = 0, \\ \int_{\Omega_c} \delta \boldsymbol{\lambda} (\boldsymbol{v}_{\boldsymbol{M}} - \boldsymbol{v}_{\boldsymbol{m}}) \, dV_c = 0. \end{cases} \tag{3.17}$$

The equations 3.17 have to be valid for every $\delta \boldsymbol{v}_M$ $\delta \boldsymbol{v}_m$ and $\delta \boldsymbol{\lambda}$, that satisfy:

$$\delta \boldsymbol{v}^M \in \mathcal{V}_0^M = \left\{ \delta \boldsymbol{v}^M \in H^1(\Omega^M) | \ \delta \boldsymbol{v}^M = 0 \ on \ \Gamma^M \right\}, \tag{3.18}$$

$$\delta \boldsymbol{v}^m \in \mathcal{V}_0^m = \left\{ \delta \boldsymbol{v}^m \in H^1(\Omega^m) | \ \delta \boldsymbol{v}^m = 0 \ on \ \Gamma^m \right\}, \tag{3.19}$$

$$\boldsymbol{v}^M \in \mathcal{V}^M = \left\{ \boldsymbol{v}^M \in H^1(\Omega^M) | \boldsymbol{v}^M = \widehat{\boldsymbol{v}^{\boldsymbol{M}}} \ on \ \Gamma^M \right\}, \tag{3.20}$$

$$\boldsymbol{v}^m \in \mathcal{V}^m = \left\{ \boldsymbol{v}^m \in H^1(\Omega^m) | \boldsymbol{v}^m = \widehat{\boldsymbol{v}^{\boldsymbol{m}}} \ on \ \Gamma^m \right\}, \tag{3.21}$$

$$\delta \boldsymbol{\lambda} \ , \boldsymbol{\lambda} \in H^1(\Omega^c), \tag{3.22}$$

in which $\widehat{\boldsymbol{v}^{\boldsymbol{M}}}$ and $\widehat{\boldsymbol{v}^{\boldsymbol{m}}}$ are the applied velocity boundary conditions on the macro and micro domain, respectively. In 3.17 the weighting functions ensure a partition of the unity for the energy in the gluing zone such that $\alpha_M + \alpha_m = 1$. The coupling is enforced imposing the continuity of velocities in the overlap domain, Ω_c using a Lagrangian multipliers field $\boldsymbol{\lambda}$. Such coupling is not respected locally at nodal locations, rather it is imposed in a weak form. Macro, micro and coupling domains are discretised in space using the classic definition of shape functions, defining in particular three different sets $\boldsymbol{N}_M$, $\boldsymbol{N}_m$, $\boldsymbol{N}_\lambda$ to approximate respectively the macro and micro kinematic variables as well as the Lagrange Multiplier. Based on these approximations the semi-discretised form is as follows

$$\begin{cases} \tilde{\boldsymbol{M}}^M \boldsymbol{a}^M + \tilde{\boldsymbol{f}}_{int}^M + \boldsymbol{L}^M \boldsymbol{\lambda} = 0, \\ \tilde{\boldsymbol{M}}^m \boldsymbol{a}^m + \tilde{\boldsymbol{f}}_{int}^m + \boldsymbol{L}^m \boldsymbol{\lambda} = 0, \\ \boldsymbol{L}^M \boldsymbol{v}^M + \boldsymbol{L}^m \boldsymbol{v}^m = 0, \end{cases} \tag{3.23}$$

in which $\tilde{\boldsymbol{M}}^M$ and $\tilde{\boldsymbol{M}}^m$, represent the lumped weighted mass matrices, similarly $\tilde{\boldsymbol{f}}_{int}^M$ and $\tilde{\boldsymbol{f}}_{int}^m$ are the weighted internal force vectors of the macro and micro scale respectively and $\boldsymbol{L}^M$ and $\boldsymbol{L}^m$ represent the Lagrange multiplier matrices.

It is clear from equation 3.23 that the original form of the Arlequin method requires the assembly of two matrices connected to the Lagrange multipliers, for the macro and micro domain. Moreover, the presence of the weighting functions in the integrals connected to the mass and force matrix, limits the use of under-integrated C^0 elements, common in explicit dynamics, since their integration rules should be modified to account for the weights. It has been demonstrated that while non-linear weighting on Ω_c have a beneficial effect in the reduction of spurious wave reflection, they introduce a significant reduction of the time-step in explicit simulations [72].

The first improvement with respect to the original framework looks at those two aspects related to the use of the weighting functions. In particular it can be noticed that partition of unity for the energies in Ω_c, can be achieved associating the weight at nodal positions after the spatial semi-discretisation. Therefore the first modification of the original framework applies the parameters $\boldsymbol{\alpha}^M$ and $\boldsymbol{\alpha}^m$ once the integrals in space are evaluated. This process formally leads to:

$$\begin{cases} \boldsymbol{\alpha^M} \boldsymbol{M}^M \boldsymbol{a}^M + \boldsymbol{\alpha^M} \boldsymbol{f}_{int}^M + \boldsymbol{L}^M \boldsymbol{\lambda} = 0, \\ \boldsymbol{\alpha^m} \boldsymbol{M}^m \boldsymbol{a}^m + \boldsymbol{\alpha^m} \boldsymbol{f}_{int}^m + \boldsymbol{L}^m \boldsymbol{\lambda} = 0, \\ \boldsymbol{L}^M \boldsymbol{v}^M + \boldsymbol{L}^m \boldsymbol{v}^m = 0, \end{cases} \tag{3.24}$$

in which $\boldsymbol{\alpha^M}$ and $\boldsymbol{\alpha^m}$ are the nodal diagonal matrices of the weights and $\boldsymbol{M}^m$, $\boldsymbol{f}_{int}^M$ and $\boldsymbol{f}_{int}^m$ are the original mass and internal forces matrices as if no coupling was applied. The advantage of this new formulation is twofold. Firstly, the elements do not need to use modified integration rules for the computation of mass matrices and internal forces, making suitable the use of under-integrated elements. Moreover, the

assignment of the weights directly to the nodes, does not change the eigenvalues of the system, not altering the wave propagation properties, and more importantly the time-step of the simulation as demonstrated in the next section. The second improvement of this new formulation looks at the way the coupling is imposed. In particular, in 3.17, the coupling is applied in a weak form, which will lead to the assembling and inverting of non-diagonal matrices. In the spirit of the explicit formulation of finite elements, such coupling can be applied in a strong sense. The continuity expressed as:

$$\boldsymbol{N}\boldsymbol{v}^M - \boldsymbol{v}^m = \boldsymbol{0}, \tag{3.25}$$

requires the velocities at the micro nodal positions to conform the projection of the macro velocities at the same nodal position at every time. Such constraint can be applied using the lagrangian multipliers, in which the power introduced on the discretised system by the coupling, P_λ, is expressed only using the coupled nodes as:

$$P_\lambda = \boldsymbol{\lambda}^T \cdot (\boldsymbol{N}\boldsymbol{v}^M - \boldsymbol{v}^m) = (\boldsymbol{f}^m_{corr})^T \cdot (\boldsymbol{N}\boldsymbol{v}^M - \boldsymbol{v}^m), \tag{3.26}$$

where a dimensional analysis reveals that the Lagrangian multipliers, can be treated as nodal forces $\boldsymbol{f}^m_{corr}$ acting on the nodes of the fine mesh. Equation 3.26 can be used to compute the variation of the power with respect to $\delta\boldsymbol{v}^M$, $\delta\boldsymbol{v}^m$ and $\delta\boldsymbol{f}^m_{corr}$ as:

$$\delta P_\lambda = \frac{\partial P_\lambda}{\partial \boldsymbol{v}^M}\delta\boldsymbol{v}^M + \frac{\partial P_\lambda}{\partial \boldsymbol{v}^m}\delta\boldsymbol{v}^m + \frac{\partial P_\lambda}{\partial \boldsymbol{f}^m_{corr}}\delta\boldsymbol{f}^m_{corr}. \tag{3.27}$$

The partial derivatives in 3.27 can be computed using 3.26 as:

$$\begin{cases} \frac{\partial P_\lambda}{\partial \boldsymbol{v}^M} = \boldsymbol{N}^T\boldsymbol{f}^m_{corr}, \\ \\ \frac{\partial P_\lambda}{\partial \boldsymbol{v}^m} = -\boldsymbol{I}\boldsymbol{f}^m_{corr} = -\boldsymbol{f}^m_{corr}, \\ \\ \frac{\partial P_\lambda}{\partial \boldsymbol{f}^m_{corr}} = \boldsymbol{N}\boldsymbol{v}^M - \boldsymbol{v}^m, \end{cases} \tag{3.28}$$

in which $\boldsymbol{I}$ represents the identity matrix. Using the principle of virtual power expressed in equation 3.6 it is possible to express the semi-discretised equations of

motion for the coupled system in terms of the variation of the macro, micro and coupling powers δP^M, δP^m and δP_λ. In particular:

$$\delta P = \delta P^M + \delta P^m + \delta P_\lambda = 0. \tag{3.29}$$

The contributions to the macro and micro powers, P^M and P^m considering the weights and the equations 3.5 discretised over the macro and micro domains can be defined as:

$$\begin{cases} \delta P^M = (\boldsymbol{\alpha}^M \boldsymbol{M}^M \boldsymbol{a}^{\boldsymbol{M}} + \boldsymbol{\alpha}^M \boldsymbol{f}^M_{int}) \cdot \delta \boldsymbol{v}^M, \\ \delta P^m = (\boldsymbol{\alpha}^m \boldsymbol{M}^m \boldsymbol{a}^m + \boldsymbol{\alpha}^m \boldsymbol{f}^m_{int}) \cdot \delta \boldsymbol{v}^m. \end{cases} \tag{3.30}$$

Invoking the arbitrariness of the functions $\delta \boldsymbol{v}^M$, $\delta \boldsymbol{v}^m$ and $\delta \boldsymbol{f}^m_{corr}$ the semi-discretised equations of motions, for this framework, can be written as:

$$\begin{cases} \boldsymbol{\alpha}^M \boldsymbol{M}^M \boldsymbol{a}^{\boldsymbol{M}} + \boldsymbol{\alpha}^M \boldsymbol{f}^M_{int} + \boldsymbol{N}^T \boldsymbol{f}^m_{corr} = \boldsymbol{0}, \\ \boldsymbol{\alpha}^m \boldsymbol{M}^m \boldsymbol{a}^m + \boldsymbol{\alpha}^m \boldsymbol{f}^m_{int} - \boldsymbol{f}^m_{corr} = \boldsymbol{0}, \\ \boldsymbol{N} \boldsymbol{v}^M - \boldsymbol{v}^m = \boldsymbol{0}. \end{cases} \tag{3.31}$$

The matrix $\boldsymbol{N}^T$ in the system of equation 3.31 represents the interpolation matrix form the fine scale to the coarse scale. It is interesting to note that at the fine scale the Lagrange multipliers have the physical interpretation of nodal forces, that are then interpolated on the coarse scale. Using the assumption of the linking condition stating that the nodal quantities on the fine scale have to be equal to the linear interpolation of the coarse scale kinematic quantities, it is possible to derive an explicit expression for the coupling forces:

$$\begin{cases} \boldsymbol{\alpha}^{M\to m} \boldsymbol{M}^{M\to m} \boldsymbol{a}^{M\to m} + \boldsymbol{\alpha}^{M\to m} \boldsymbol{f}^{M\to m}_{int} + \boldsymbol{f}^m_{\boldsymbol{corr}} = 0, \\ \boldsymbol{\alpha}^m \boldsymbol{M}^m \boldsymbol{a}^m + \boldsymbol{\alpha}^m \boldsymbol{f}^m_{int} - \boldsymbol{f}^m_{\boldsymbol{corr}} = 0, \\ \boldsymbol{v}^{M\to m} - \boldsymbol{v}^m = \boldsymbol{0}, \end{cases} \tag{3.32}$$

in which the operator $(\cdot)^{M\to m}$ is a shorthand for the projection of a generic variable $(\cdot)$ from the coarse to the fine scale domain. By definition the weights on the coarse scale can be expressed using the partition of unity condition leading to:

$$\boldsymbol{\alpha}^{M\to m} = 1 - \boldsymbol{\alpha}^m. \tag{3.33}$$

Before discretising in time the system of equations in 3.32, it is important to assess the effect of both the coupling forces and the weights on the critical time-step that will not lead to instabilities.

3.2.1 Determination of the critical time step for the novel framework

As stated in section 3.1.1 the major drawback of explicit time integration schemes is their conditional stability that limits the maximum time-step to a critical value. Such Δt_{crit} can be evaluated using the equation 3.16, in which ω_{max} represents the maximum eigenfrequency of the domain. The evaluation of such eigenvalue can be computationally expensive for large problems, considering that it requires assembling the global stiffness matrix, which is not contemplated in explicit numerical methodologies. It is clear that the determination of an estimation is crucial for the applicability of the proposed framework. Therefore, it is of paramount importance to establish the effect of the presence of weighting parameters and kinematic coupling on Δt_{crit}. To this purpose as suggested in [12], the linear stability of the system 3.31 will be investigated in this section.

The equilibrium configuration is perturbed by a small quantity, in this context represented with the symbol $\check{(\cdot)}$. Since the perturbations are assumed to be small, the dynamic equations are considered to be linear, that is a linearized model is used for the perturbed internal forces:

$$\begin{cases} \check{\boldsymbol{f}}_{int}^{M\to m} = \boldsymbol{K}^{M\to m,tan}\check{\boldsymbol{u}}^{M\to m}, \\ \check{\boldsymbol{f}}_{int}^{m} = \boldsymbol{K}^{m,tan}\check{\boldsymbol{u}}^{m}, \end{cases} \tag{3.34}$$

where in 3.34 $\boldsymbol{K}^{M\to m,tan}$ and $\boldsymbol{K}^{m,tan}$ represent the linearised (tangent) global stiffness matrices for the two different scales and $\check{\boldsymbol{u}}^{M\to m}$ and $\check{\boldsymbol{u}}^{m}$ the perturbed displacements. Moreover, it is clear that if the constraint in 3.31 expressed in terms of velocities is always verified, its validity will not change when expressed in terms of perturbed acceleration as:

$$\check{\boldsymbol{a}}^{M\to m} - \check{\boldsymbol{a}}^{m} = 0. \tag{3.35}$$

Perturbing the equation 3.35 and using the equations 3.34 and 3.31, simplifying the equilibrium state, it is possible to write the perturbed linearised form of the coupled system of equations as:

$$\begin{cases} \boldsymbol{\alpha}^{M\to m}\boldsymbol{M}^{M\to m}\check{\boldsymbol{a}}^{M\to m} + \boldsymbol{\alpha}^{M\to m}\boldsymbol{K}^{M\to m,tan}\check{\boldsymbol{u}}^{M\to m} + \check{\boldsymbol{f}}^{m}_{\boldsymbol{corr}} = 0, \\ \boldsymbol{\alpha}^{m}\boldsymbol{M}^{m}\check{\boldsymbol{a}}^{m} + \boldsymbol{\alpha}^{m}\boldsymbol{K}^{m,tan}\check{\boldsymbol{u}}^{m} - \check{\boldsymbol{f}}^{m}_{\boldsymbol{corr}} = 0, \\ \check{\boldsymbol{a}}^{M\to m} - \check{\boldsymbol{a}}^{m} = \boldsymbol{0}. \end{cases} \tag{3.36}$$

in which $\check{\boldsymbol{f}}^{m}_{\boldsymbol{corr}}$ represents the force necessary to enforce the coupling in the perturbed state. The linear system of ordinary differential equations in 3.36 admits a general solution in the exponential form:

$$\begin{cases} \check{\boldsymbol{u}}^{M\to m} = \boldsymbol{A}^{M\to m}e^{\sqrt{\check{\boldsymbol{\Lambda}}^{M\to m}}t}, \\ \check{\boldsymbol{u}}^{m} = \boldsymbol{A}^{m}e^{\sqrt{\check{\boldsymbol{\Lambda}}^{m}}t}, \end{cases} \tag{3.37}$$

in which $\boldsymbol{A}^{M\to m}$ and $\boldsymbol{A}^{m}$ are constant vectors containing the amplitudes, while $\sqrt{\check{\boldsymbol{\Lambda}}^{M\to m}}$ and $\sqrt{\check{\boldsymbol{\Lambda}}^{m}}$ represent the square of the eigenfrequencies ω for the two domains, respectively. From the equations in 3.37 it can be derived that the accelerations can be written as:

$$\begin{cases} \check{\boldsymbol{a}}^{M\to m} = \boldsymbol{A}^{M\to m}\check{\boldsymbol{\Lambda}}^{M\to m}e^{\sqrt{\check{\boldsymbol{\Lambda}}^{M\to m}}t}, \\ \check{\boldsymbol{a}}^{m} = \boldsymbol{A}^{m}\check{\boldsymbol{\Lambda}}^{m}e^{\sqrt{\check{\boldsymbol{\Lambda}}^{m}}t}. \end{cases} \tag{3.38}$$

The substituion of the equations 3.37 and 3.38 into 3.36 yields to:

$$\left[\begin{array}{cc|c} \check{\boldsymbol{Q}}^{M\to m} & \boldsymbol{0} & \boldsymbol{I} \\ \boldsymbol{0} & \check{\boldsymbol{Q}}^{m} & -\boldsymbol{I} \\ \hline \boldsymbol{I} & -\boldsymbol{I} & \boldsymbol{0} \end{array}\right] \left[\begin{array}{c} \boldsymbol{A}^{M\to m}e^{\sqrt{\check{\boldsymbol{\Lambda}}^{M\to m}}t} \\ \boldsymbol{A}^{m}e^{\sqrt{\check{\boldsymbol{\Lambda}}^{m}}t} \\ \hline \check{\boldsymbol{f}}^{m}_{\boldsymbol{corr}} \end{array}\right] = \left[\begin{array}{c} \boldsymbol{0} \\ \boldsymbol{0} \\ \hline \boldsymbol{0} \end{array}\right], \tag{3.39}$$

in which $\boldsymbol{I}$ represents the identity matrix, $\boldsymbol{0}$ a zero-entries matrix. It is important to note that the system is conveniently partitioned such that the upper left partition represents the uncoupled system. The matrices $\check{\boldsymbol{Q}}^{m}$ and $\check{\boldsymbol{Q}}^{M\to m}$ are defined as:

$$\check{\boldsymbol{Q}}^{M\to m} = \boldsymbol{\alpha}^{M\to m}\boldsymbol{K}^{M\to m,tan} + \boldsymbol{\alpha}^{M\to m}\check{\boldsymbol{\Lambda}}^{M\to m}\boldsymbol{M}^{M\to m}, \tag{3.40}$$

$$\check{\boldsymbol{Q}}^{m} = \boldsymbol{\alpha}^{m}\boldsymbol{K}^{m,tan} + \boldsymbol{\alpha}^{m}\check{\boldsymbol{\Lambda}}^{m}\boldsymbol{M}^{m}. \tag{3.41}$$

From 3.39 it is possible to notice that the unconstrained problem is bordered with constant matrices. For such system of equations, it is possible to invoke Rayleigh's

theorem for multiple constraint, whose proof is in [12], which states that the maximum eigenvalue of the constrained matrix is smaller or equal than the biggest eigenvalue of the unconstrained matrix. This is expressed as:

$$\check{\Lambda}_{max} \leq \mathring{\Lambda}_{max}, \tag{3.42}$$

in which $\mathring{\Lambda}_{max}$ represents the maximum eigenvalue of the system:

$$\begin{bmatrix} \mathring{\boldsymbol{Q}}^{M\to m} & \mathbf{0} \\ \mathbf{0} & \mathring{\boldsymbol{Q}}^{m} \end{bmatrix} \begin{bmatrix} \boldsymbol{A}^{M\to m} e^{\sqrt{\mathring{\boldsymbol{\Lambda}}^{M\to m}}t} \\ \boldsymbol{A}^{m} e^{\sqrt{\mathring{\boldsymbol{\Lambda}}^{m}}t} \end{bmatrix} = \begin{bmatrix} \mathbf{0} \\ \mathbf{0} \end{bmatrix}, \tag{3.43}$$

in which, using the same convention as in equation 3.40,

$$\mathring{\boldsymbol{Q}}^{M\to m} = \left(\boldsymbol{\alpha}^{M\to m}\boldsymbol{K}^{M\to m,tan} + \boldsymbol{\alpha}^{M\to m}\mathring{\boldsymbol{\Lambda}}^{M\to m}\boldsymbol{M}^{M\to m}\right), \tag{3.44}$$

$$\mathring{\boldsymbol{Q}}^{m} = \left(\boldsymbol{\alpha}^{m}\boldsymbol{K}^{m,tan} + \boldsymbol{\alpha}^{m}\mathring{\boldsymbol{\Lambda}}^{m}\boldsymbol{M}^{m}\right). \tag{3.45}$$

In virtue of 3.42 the critical time step can be evaluated using the matrix 3.43. For the system to be stable, the equations in 3.43 have to be valid for every value of the amplitude matrices. This condition can be expressed as:

$$\mathbf{det}\left(\begin{bmatrix} \mathring{\boldsymbol{Q}}^{M\to m} & \mathbf{0} \\ \mathbf{0} & \mathring{\boldsymbol{Q}}^{m} \end{bmatrix}\right) = 0, \tag{3.46}$$

in which the operator $\mathbf{det}([\cdot])$ indicates the computation of the determinant of the matrix $[\cdot]$. The determinant in equation 3.46 can be evaluated as:

$$\boldsymbol{det}\left(\mathring{\boldsymbol{Q}}^{M\to m}\mathring{\boldsymbol{Q}}^{m}\right) = \boldsymbol{det}\left(\mathring{\boldsymbol{Q}}^{M\to m}\right)\boldsymbol{det}\left(\mathring{\boldsymbol{Q}}^{m}\right) = 0. \tag{3.47}$$

By definition, the macro and micro portions of the domain, possess the same material properties and therefore $\boldsymbol{M}^{M\to m} = \boldsymbol{M}^{m}$. Moreover, due to the performed projection, the macro stiffness matrix can be simplified leading to $\boldsymbol{K}^{M\to m} = \boldsymbol{K}^{m}$. Using this assumption the condition in equation 3.47 is expressed as:

$$\begin{cases} \boldsymbol{det}\left(\boldsymbol{\alpha}^{M\to m}\boldsymbol{K}^{m,tan} + \boldsymbol{\alpha}^{m\to M}\mathring{\boldsymbol{\Lambda}}^{M\to m}\boldsymbol{M}^{m}\right) & = 0, \\ \boldsymbol{det}\left(\boldsymbol{\alpha}^{m}\boldsymbol{K}^{m,tan} + \boldsymbol{\alpha}^{m}\mathring{\boldsymbol{\Lambda}}^{m}\boldsymbol{M}^{m}\right) & = 0. \end{cases} \tag{3.48}$$

Using the linear property of the determinant operator in equation 3.48 the weight matrices can be collected, leading to:

$$\begin{cases} \boldsymbol{det}(\boldsymbol{\alpha}^{M\to m})\boldsymbol{det}\left(\boldsymbol{K}^{m,tan}+\mathring{\boldsymbol{\Lambda}}^{M\to m}\boldsymbol{M}^{m}\right) & =0, \\ \boldsymbol{det}(\boldsymbol{\alpha}^{m})\boldsymbol{det}\left(\boldsymbol{K}^{m,tan}+\mathring{\boldsymbol{\Lambda}}^{m}\boldsymbol{M}^{m}\right) & =0. \end{cases} \tag{3.49}$$

Assuming that the weight matrices for both equation are not null, the terms $\boldsymbol{det}\left(\boldsymbol{\alpha}^{M\to m}\right)$ and $\boldsymbol{det}\left(\boldsymbol{\alpha}^{m}\right)$ can be simplified leading to the final form of the eigenvalues system:

$$\begin{cases} \boldsymbol{det}\left(\boldsymbol{K}^{m,tan}+\mathring{\boldsymbol{\Lambda}}^{M\to m}\boldsymbol{M}^{m}\right) & =0, \\ \boldsymbol{det}\left(\boldsymbol{K}^{m,tan}+\mathring{\boldsymbol{\Lambda}}^{m}\boldsymbol{M}^{m}\right) & =0. \end{cases} \tag{3.50}$$

Clearly from 3.50 the matrices involved in the eigenvalues evaluations are the same for the two scales and therefore $\mathring{\Lambda}^{M\to m} = \mathring{\Lambda}^{m}$. Moreover, the stiffness and mass matrices are the same as if no weights was applied. For this reason, even in presence of weights the equation 3.16 still yields a valid critical time-step estimation. In the classical form of the Arlequin method, this condition does not necessarily hold true. In fact, as demonstrated in [72] the weights applied have an adverse effect on the critical time-step of the simulation.

3.2.2 Resolution Algorithm

The equations in 3.32 can be solved by defining a set of trial kinematic quantities, defined as $\bar{\cdot}$, that do not take in consideration the coupling condition, but are linked to the internal forces.

$$\begin{cases} \boldsymbol{\alpha}^{M}\boldsymbol{M}^{m}\boldsymbol{N}\bar{\boldsymbol{a}}^{M}+\boldsymbol{\alpha}^{M}\boldsymbol{f}_{int}^{M\to m}=0, \\ \boldsymbol{\alpha}^{m}\boldsymbol{M}^{m}\bar{\boldsymbol{a}}^{m}+\boldsymbol{\alpha}^{m}\boldsymbol{f}_{int}^{m}=0. \end{cases} \tag{3.51}$$

The weights in both equations can be simplified since they are non zero quantities. Substituting equations 3.51 in equation 3.32, and using central difference in time from equation 3.14, a new expression for the discretised coupled system is obtained.

$$\begin{cases} \boldsymbol{\alpha}^M \boldsymbol{M}^m \boldsymbol{N} \left(\frac{\boldsymbol{v}^M_{n+\frac{1}{2}} - \boldsymbol{v}^M_{n-\frac{1}{2}}}{\Delta t^m} \right) + \boldsymbol{\alpha}^M \boldsymbol{M}^m \boldsymbol{N} \left(\frac{\bar{\boldsymbol{v}}^M_{n+\frac{1}{2}} - \boldsymbol{v}^M_{n-\frac{1}{2}}}{\Delta t^m} \right) + \boldsymbol{f}^m_{corr} = \boldsymbol{0}, \\ \boldsymbol{\alpha}^m \boldsymbol{M}^m \left(\frac{\boldsymbol{v}^m_{n+\frac{1}{2}} - \boldsymbol{v}^m_{n-\frac{1}{2}}}{\Delta t^m} \right) + \boldsymbol{\alpha}^m \boldsymbol{M}^m \left(\frac{\bar{\boldsymbol{v}}^m_{n+\frac{1}{2}} - \boldsymbol{v}^m_{n-\frac{1}{2}}}{\Delta t^m} \right) - \boldsymbol{f}^m_{corr} = \boldsymbol{0}, \\ \boldsymbol{N} \boldsymbol{v}^M_{n+\frac{1}{2}} - \boldsymbol{v}^m_{n+\frac{1}{2}} = \boldsymbol{0}, \\ \boldsymbol{N} \boldsymbol{v}^M_{n-\frac{1}{2}} - \boldsymbol{v}^m_{n-\frac{1}{2}} = \boldsymbol{0}. \end{cases} \tag{3.52}$$

In equations 3.52 the velocities at the previous half time-step are not the trial ones, because they take in account the corrective forces of the previous time-step. In this system the only unknown is $\boldsymbol{f}^m_{corr}$ that can be solved for resulting in:

$$\boldsymbol{f}^m_{corr} = \frac{\boldsymbol{M}^m \boldsymbol{\alpha}^M \boldsymbol{\alpha}^m (\boldsymbol{N} \bar{\boldsymbol{v}}^M_{n+\frac{1}{2}} - \bar{\boldsymbol{v}}^m_{n+\frac{1}{2}})}{\Delta t^m}. \tag{3.53}$$

The equation 3.53 expresses the corrective forces needed to enforce the coupling on the two domains. The presence of the weight function at the micro-scale weights the effect of this force such that its contribution is scaled according to $\boldsymbol{\alpha}^m$ and $\boldsymbol{\alpha}^M$. In the next section, the influence of this scaling will be studied. It is important to notice, as well, that equation 3.53 requires the macro-scale velocity at micro-scale time-steps, therefore a linear interpolation in time can be used as:

$$\bar{\boldsymbol{v}}^M_{n+\frac{1}{2}} = \bar{\boldsymbol{v}}^M_{n-\frac{1}{2}} + \bar{\boldsymbol{a}}^M_N \Delta t^m, \tag{3.54}$$

in which n is the micro step and N is the macro step. The complete algorithm for the coupling of two simulations is outlined in box 2

Flowchart 2. *Flowchart for novel concurrent explicit framework*

1. *Initialise macro and micro mesh: set* $\boldsymbol{v}^M_0$,$\boldsymbol{\sigma}^M_0$, $\boldsymbol{v}^m_0$, $\boldsymbol{\sigma}^m_0$
   $t^M = 0$, $t^m = 0$ *compute* $\boldsymbol{M^M}$ *and* $\boldsymbol{M^m}$

   Macro Scale Update*:* $t^{N-1} \rightarrow t^N$, Δt^M

2. *Evaluate macro nodal forces* $\boldsymbol{f}^M_N$ *from equation 3.13*

3. *Evaluate macro trial accelerations*
$\bar{\boldsymbol{a}}_{\boldsymbol{N}}^{\boldsymbol{M}} = (\boldsymbol{M}^M)^{-1}(\boldsymbol{f}_N^{\boldsymbol{M,ext}} - \boldsymbol{f}_N^{\boldsymbol{M,int}})$

4. *Update macro trial nodal velocities*
$\bar{\boldsymbol{v}}_{N+\frac{1}{2}}^M = \boldsymbol{v}_{N+\frac{1}{2}-\eta}^M + \eta\Delta t^M \bar{\boldsymbol{a}}_N^M \; : \; \eta = \begin{cases} \frac{1}{2} & \text{if } N = 0 \\ 1 & \text{if } N > 0 \end{cases}$

5. *Overwrite trial macro nodal velocity for enforced boundary conditions*

6. *Update macro trial nodal displacements*
$\bar{\boldsymbol{u}}_{N+1}^M = \boldsymbol{u}_N^M + \Delta t^M \bar{\boldsymbol{v}}_{N+\frac{1}{2}}^M$

7. *Update macro nodal velocities*
$\bar{\boldsymbol{v}}_{n+\frac{1}{2}}^M = \bar{\boldsymbol{v}}_{n-\frac{1}{2}}^M + \Delta t^m \bar{\boldsymbol{a}}_n^M$

8. *Update macro counter and time*

***Micro Scale Update**: $t^{N-1} \rightarrow t^N$, Δt^m*

9. *Evaluate micro nodal forces $\boldsymbol{f}_n^m$ from equation 3.13*

10. *Evaluate micro trial accelerations*
$\bar{\boldsymbol{a}}_{\boldsymbol{n}}^{\boldsymbol{m}} = (\boldsymbol{M}^m)^{-1}(\boldsymbol{f}_n^{\boldsymbol{m,ext}} - \boldsymbol{f}_n^{\boldsymbol{m,int}})$

11. *Update micro trial nodal Velocities*
$\bar{\boldsymbol{v}}_{n+\frac{1}{2}}^m = \boldsymbol{v}_{n+\frac{1}{2}-\eta}^m + \eta\Delta t^m \bar{\boldsymbol{a}}_n^m \; : \; \eta = \begin{cases} \frac{1}{2} & \text{if } n = 0 \\ 1 & \text{if } n > 0 \end{cases}$

12. *Overwrite trial nodal velocity for enforced boundary conditions*

13. *Update micro trial nodal displacements*
$\bar{\boldsymbol{u}}_{n+1}^m = \boldsymbol{u}_n^m + \Delta t^m \bar{\boldsymbol{v}}_{n+\frac{1}{2}}^m$

Micro Scale Coupling

14. *Compute corrective forces from equation 3.53*

15. *Evaluate micro accelerations*
$\boldsymbol{a}_{\boldsymbol{n}}^{\boldsymbol{m}} = (\boldsymbol{M}^m)^{-1}(\boldsymbol{f}_n^{\boldsymbol{m,ext}} - \boldsymbol{f}_n^{\boldsymbol{m,int}} + \boldsymbol{f}_n^{\boldsymbol{m,corr}})$

16. *Update micro nodal Velocities*
$\boldsymbol{v}_{n+\frac{1}{2}}^m = \boldsymbol{v}_{n-\frac{1}{2}}^m + \Delta t^m \boldsymbol{a}_n^m$

17. *Update micro nodal displacements*
$\boldsymbol{u}_{n+1}^m = \boldsymbol{u}_n^m + \Delta t^m \boldsymbol{v}_{n+\frac{1}{2}}^m$

18. *Update micro scale counter and time*

19. *If micro scale simulation not complete go to 9.*

Macro Scale Coupling

20. *Evaluate macro accelerations*
$\boldsymbol{a_N^M} = (\boldsymbol{M}^M)^{-1}(\boldsymbol{f}_N^{\boldsymbol{M,ext}} - \boldsymbol{f}_N^{\boldsymbol{M,int}} - \boldsymbol{N}^T \boldsymbol{f}_N^{\boldsymbol{m,corr}})$

21. *Update macro nodal Velocities*
$\boldsymbol{v}^M_{N+\frac{1}{2}} = \boldsymbol{v}^M_{N-\frac{1}{2}} + \Delta t^M \boldsymbol{a}^M_N$

22. *Update macro nodal displacements*
$\boldsymbol{u}^M_{N+1} = \boldsymbol{u}^M_N + \Delta t^M \boldsymbol{v}^M_{N+\frac{1}{2}}$

23. *Update macro scale counter and time*

24. *If macro scale simulation not complete go to 2.*

3.2.3 Stability analysis

The macro and micro scale are coupled through the corrective forces, that can be directly evaluated using the equation 3.53. Employing the energy method introduced by Hughes in [93] and used in [6,63–65] it is possible to establish whether the coupling leads to a stable system or to the formation and propagation of instabilities. This approach studies the sign of the increment of mechanical energy in the discretised system over one time-step. When the increment of energy is positive the framework under examination is unstable, since the energy will grow boundlessly in time. On the other hand, if the increment is negative, the system will dissipate energy over time, but in a stable manner. Finally, if there is no increment of energy in one time-step the system is stable and conservative. The balance of the rate of energy $\dot{E}^{tot}$ can be split in different contributes from the macro and micro scale domains as in [94] as:

$$\dot{E}^{tot} = \dot{E}^M_{int} + \dot{E}^M_{kin} + \dot{E}^m_{int} + \dot{E}^m_{kin} \tag{3.55}$$

in which the contribution coming from the internal forces $\dot{E}^M_{int}$, $\dot{E}^m_{int}$ and kinetic contribution $\dot{E}^M_{kin}$, $\dot{E}^m_{kin}$ are defined as:

$$\dot{E}^M_{int} = \left(\boldsymbol{v}^M\right)^T \boldsymbol{\alpha}^M \sum_{i=1}^{Nelements^M} \int_{\Omega_i} \boldsymbol{B}^T \boldsymbol{\sigma}^M \; dV, \tag{3.56}$$

$$\dot{E}^m_{int} = \left(\boldsymbol{v}^m\right)^T \boldsymbol{\alpha}^m \sum_{i=1}^{Nelements^m} \int_{\Omega_i} \boldsymbol{B}^T \boldsymbol{\sigma}^m \; dV, \tag{3.57}$$

$$\dot{E}^M_{kin} = \left(\boldsymbol{v}^M\right)^T \boldsymbol{\alpha}^M \boldsymbol{M}^M \boldsymbol{a}^M, \tag{3.58}$$

$$\dot{E}^m_{kin} = \left(\boldsymbol{v}^m\right)^T \boldsymbol{\alpha}^m \boldsymbol{M}^m \boldsymbol{a}^m. \tag{3.59}$$

Substituting equation 3.31 and equations 3.56 to 3.59 in 3.57 the increment of total energy can be expressed as:

$$\begin{aligned} \dot{E}^{tot} = \left(\boldsymbol{v}^M\right)^T \left(-\boldsymbol{\alpha}^M \cancel{\boldsymbol{f}^M_{int}} - \boldsymbol{N}^T \boldsymbol{f}^m_{corr} + \boldsymbol{\alpha}^M \cancel{\sum_{i=1}^{Nelements^M} \int_{\Omega_i} \boldsymbol{B}^T \boldsymbol{\sigma}^M dV}\right) \\ + \left(\boldsymbol{v}^m\right)^T \left(-\boldsymbol{\alpha}^m \cancel{\boldsymbol{f}^m_{int}} + \boldsymbol{f}^m_{corr} + \boldsymbol{\alpha}^m \cancel{\sum_{i=1}^{Nelements^m} \int_{\Omega_i} \boldsymbol{B}^T \boldsymbol{\sigma}^m dV}\right), \end{aligned} \tag{3.60}$$

in which the contributions connected to the internal forces cancel out in virtue of the equation 3.11. The condition for which the framework ensures conservation or dissipation of energy can be then expressed as:

$$\dot{E}_{tot} \leq 0. \tag{3.61}$$

Such condition can be derived from 3.60 as:

$$\dot{E}_{tot} = -\left(\boldsymbol{v}^M\right)^T \boldsymbol{N}^T \boldsymbol{f}^m_{corr} + \left(\boldsymbol{v}^m\right)^T \boldsymbol{f}^m_{corr} \leq 0. \tag{3.62}$$

Equation 3.62 defines the power dissipated by the framework, due to the coupling. The inequality in 3.62 holds true because the projection operator $\boldsymbol{N}$ always subtracts energy from the fine scale, thus resulting in small dissipation. In particular the framework results dissipative at frequencies close to the cut-off frequency of the coarse scale domain. Such dissipation is beneficial for the spurious reflections. The magnitude of this dissipation at both macro and micro scales is studied in the next sections.

3.2.4 Error estimation

The adequacy of a mesh to resolve all the frequencies of the waves travelling the domain, can be analysed estimating the error committed at every time-step. The different techniques available in literature can be divided in two groups, namely a priori and a posteriori error estimation. A priori estimators are designed to provide information about the asymptotic behaviour of the discretisation error. On the other hand, a posteriori techniques make use of the finite element solution to estimate the actual error of a particular mesh. Grätsch and Bathe have reviewed different formulations of error estimators in [95]. In this thesis, a novel a posteriori error estimation technique will steer the error estimation based on a local higher order interpolation of the displacement in each element.

In dynamic problems the error is split in a temporal and a spatial contribution and they can be computed separately [9, 84, 85]. However, in explicit dynamics time and length scales are intimately connected through the conditional stability expressed in equation 3.16. This condition justifies the use of only the spatial error to adaptively refine a mesh, since the time-step (and therefore the temporal error), will be reduced accordingly. As highlighted in the literature review chapter in section 2.1.3 the most popular a posteriori technique for the error estimation is the super-convergent patch recovery (SPR) proposed by Zienkiewicz and Zhu [10]. This estimator requires the resolution system of equations associated to patch of elements, that could become computationally expensive for models that include several thousands of elements.

3.2.5 A local spatial error estimator based on hermitian interpolations

Following the approach presented in [10] extended to dynamic problems, at any time t, the local spatial error of in the stresses of a finite element solution can be expressed as the difference between the solution of the problem $\boldsymbol{\sigma}(\boldsymbol{x}, t)$ and the interpolated value of this solution using the finite element shape functions $\boldsymbol{\sigma_h}(\boldsymbol{x}, t)$

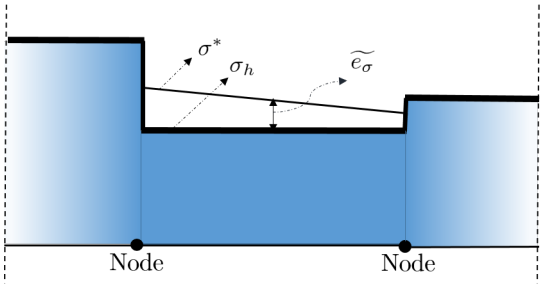

Figure 3.3: Schematic representation of the recovery technique presented in [10], for one dimensional element with one integration point. The original stress σ^h is discontinuous at the nodal position. A continuous post-processed stress can be obtained averaging the contributions coming from different elements resulting in σ^*. At every integration point, the error, $\widetilde{e}_\sigma$, is defined as the difference between the two stresses.

as:

$$\boldsymbol{e_\sigma}(\boldsymbol{x},t) = \boldsymbol{\sigma}(\boldsymbol{x},t) - \boldsymbol{\sigma_h}(\boldsymbol{x},t). \tag{3.63}$$

For convenience, the mesh locations over which the local errors are computed correspond to the position of the integration points of each element, in which the stress tensor is readily available. It is worth noticing that the local error $\boldsymbol{e_\sigma}(\boldsymbol{x},t)$ has the same dimensions of the stress vector. In practical finite element simulations the solution in terms of stress, is not known a priori, and the equation 3.63 is approximated as:

$$\widetilde{\boldsymbol{e}}_{\boldsymbol{\sigma}}(\boldsymbol{x},t) = \boldsymbol{\sigma}^*(\boldsymbol{x},t) - \boldsymbol{\sigma_h}(\boldsymbol{x},t), \tag{3.64}$$

in which $\widetilde{\boldsymbol{e}}_{\boldsymbol{\sigma}}(\boldsymbol{x},t)$ represents the approximated error and $\boldsymbol{\sigma}^*(\boldsymbol{x},t)$ is a recovered solution for the finite element problem.

In one-dimension, using linear elements, such post-processed solution is computed in two steps. In the first step the stress $\boldsymbol{\sigma_h}(\boldsymbol{x},t)$, originally discontinuous at nodal position as shown in figure 3.3 is smoothed averaging the contributions coming from the different elements. The recovered stress represents $\boldsymbol{\sigma}^*(\boldsymbol{x},t)$ that can be easily interpolated at the integration points to compute the local stress error. Since the error defined in 3.64 represents a stress, its energy norm, $||(\cdot)||$ can be computed as:

$$||\widetilde{\boldsymbol{e}}_{\boldsymbol{\sigma}}(\boldsymbol{x},t)|| = \sum_{i=1}^{N_{elements}} \int_{\Omega_i} \widetilde{\boldsymbol{e}}_{\boldsymbol{\sigma}}(\boldsymbol{x},t)\boldsymbol{S}(\boldsymbol{x},t)\widetilde{\boldsymbol{e}}_{\boldsymbol{\sigma}}(\boldsymbol{x},t)dV, \tag{3.65}$$

in which $\boldsymbol{S}(\boldsymbol{x}, t)$ represents the compliance matrix of the material, potentially dependent on time and position in the computational domain.

The same approach can be applied for the local error in strains rather than stresses, therefore the local error in stresses can be replaced by the local error in terms of strains:

$$\widetilde{\boldsymbol{e}}_{\boldsymbol{\epsilon}}(\boldsymbol{x}, t) = \boldsymbol{\epsilon}^*(\boldsymbol{x}, t) - \boldsymbol{\epsilon}_{\boldsymbol{h}}(\boldsymbol{x}, t). \tag{3.66}$$

In equation 3.66, a post-processed strain $\boldsymbol{\epsilon}^*(\boldsymbol{x}, t)$ is compared against the original strain in the element $\boldsymbol{\epsilon}_{\boldsymbol{h}}(\boldsymbol{x}, t)$ rather than a stress. The error in strains, differently from the one in stresses, can be computed from a higher order interpolation of the displacements. In particular, at every time t, one component of original displacements can be approximated as:

$$\boldsymbol{u}_h(\boldsymbol{x}, t) = \boldsymbol{N}(\boldsymbol{\xi}^e(\boldsymbol{x}))\boldsymbol{u}_h^e(t), \tag{3.67}$$

in which $\boldsymbol{u}_h^e(t)$ represents the collection of nodal displacements for the element e. Moreover, the interpolation functions $\boldsymbol{N}$ are computed in the parent element domain, whose coordinates are identified by $\boldsymbol{\xi}$, via the time-invariant mapping $\boldsymbol{\xi}^e$. In the context of linear under-integrated one dimensional elements, such mapping evaluates to -1 and 1 in nodal positions and to 0 on the location of integration point. The evaluation of the original strains is achieved using:

$$\boldsymbol{\epsilon}_{\boldsymbol{h}}(\boldsymbol{x}, t) = \boldsymbol{B}(\boldsymbol{\xi}^e(\boldsymbol{x}))\boldsymbol{u}_h^e(t), \tag{3.68}$$

in which $\boldsymbol{B}$ contains the derivative terms of the shape functions, with respect to the spatial derivatives in the physical domain. In this context, a higher order interpolation is represented by the Hermitian functions as:

$$\boldsymbol{u}^*(\boldsymbol{x}, t) = \boldsymbol{H}(\boldsymbol{\xi}^e(\boldsymbol{x}))\boldsymbol{\Phi}(t), \tag{3.69}$$

$$\boldsymbol{\Phi}(t) = \begin{Bmatrix} \boldsymbol{u}_h^e(t) \\ \dfrac{\partial \boldsymbol{u}_h^e(t)}{\partial \xi} \end{Bmatrix}. \tag{3.70}$$

In equation 3.69 $\boldsymbol{H}(\boldsymbol{\xi}^e(\boldsymbol{x}))$ represents a third order polynomial function obtained by imposing at every node not only the displacements $\boldsymbol{u}_{\boldsymbol{h}}(t)$ but also their derivative

$\frac{\partial \boldsymbol{u_h}(t)}{\partial \xi}$ in the parent domain to a fixed value. The main advantage of such interpolation is that is local, and does not depend on neighbour elements once the derivatives in the parent element domain are determined. Such interpolations have been used with success in 2D formulation of finite element, for the development of the Adini-Clough bending shell element [96,97]. However, they have never been used for error estimation and not been extended to three dimensions. The hermitian interpolation can be used to compute an augmented strain for every element as:

$$\boldsymbol{\epsilon}^*(\boldsymbol{x}, t) = \boldsymbol{\Delta H \Phi} = \boldsymbol{B}^H \boldsymbol{\Phi}, \tag{3.71}$$

in which $\boldsymbol{\Delta}$ contains the derivative operators, such as $\frac{d(\cdot)}{dx}$ for one-dimensional elements and $\boldsymbol{B}^H$ contains the spatial derivatives of the shape functions $\boldsymbol{H}$. Since the local error in 3.66 has the units of strains, defining $\boldsymbol{C}(\boldsymbol{x}, t)$ as the stiffness matrix of the material, its energy norm can be used to estimate the global error as:

$$||\widetilde{\boldsymbol{e}}_{\boldsymbol{\epsilon}}(\boldsymbol{x}, t)|| = \sum_{i=1}^{N_{elements}} \int_{\Omega_i} \widetilde{\boldsymbol{e}}_{\boldsymbol{\epsilon}}(\boldsymbol{x}, t) \boldsymbol{C}(\boldsymbol{x}, t) \widetilde{\boldsymbol{e}}_{\boldsymbol{\epsilon}}(\boldsymbol{x}, t) dV_{elem}. \tag{3.72}$$

The main advantage of this formulation of the error with respect to the ZZ formulation is that it can be used to compute not only a higher order strain, but also a higher order displacement.

3.2.6 Mesh kinetic and kinematic data transfer based on hermitian interpolation

Once the elements of the macro-scale are refined at lower scales, the elements at the micro-scale need initialisation of the kinetic and kinematic quantities. In the literature review section, it has been shown that such process is not trivial, since the new generated mesh needs a *consistent* transfer of the macro-scale state. In particular a consistent transfer has to ensure that

- The energies transferred do not alter the equilibrium state
- The diffusion of the interpolated quantities is negligible

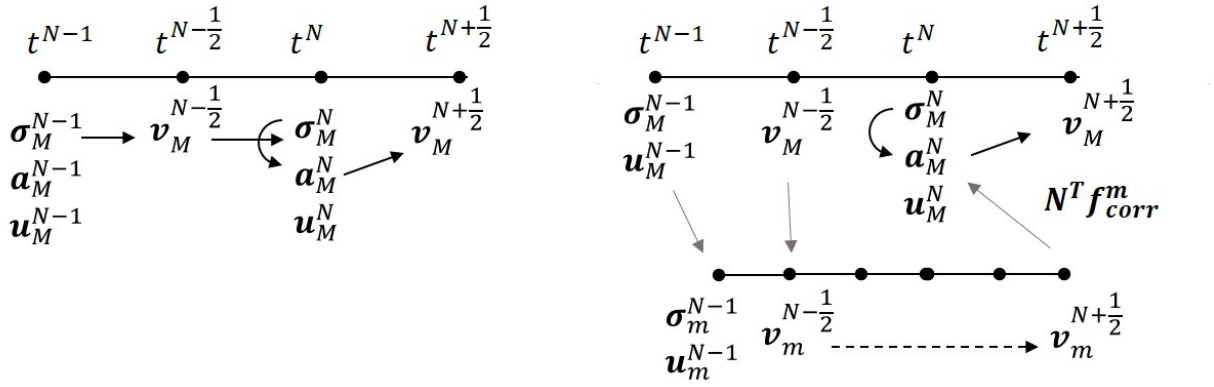

Figure 3.4: Central difference temporal discretisation on the right. At every moment of the simulation, the solution is propagated from t^{n-1} to t^n. The velocities are always half time-step ahead of the accelerations. On the left, the multi-scale time stepping scheme proposed is depicted, for a refinement factor of 2. At every macro time-step the stresses, displacements and velocities at time t^{N-1} and $t^{N-\frac{1}{2}}$, are interpolated on the micro scale. Once the interpolation is complete, the micro-scale is updated 2 times and the corrective forces are sent back to the macro-scale, where a new $v_M^{N+\frac{1}{2}}$ is computed.

For implicit schemes in which the equilibrium is sought iteratively, a balance step ensures that the data transferred is consistent, as in [9, 82, 88, 98]. In this section a different data transfer scheme based on hermitian interpolations is developed. Particular attention is given to the consistency of the interpolated states between the mesh, which is ensured without enforcing a balancing step.

The propagation of the solution at one macro-time step is depicted in figure 3.4. The main assumption of the central difference algorithm is that the acceleration is constant over half time-steps. Once the solution is computed at time t^N, the error is checked using equation 3.72. If the error is higher than an user input tolerance the time-step is rejected, and a refined mesh is created that will compute a new state of the mesh at time t^N. The kinematic constraint based on velocities of the last two equations in 3.52, prescribe the velocity $\boldsymbol{v}^{N-\frac{1}{2}}$ on the fine scale, while the main assumption of constant acceleration over one macro-time step prescribes the acceleration $\boldsymbol{a}^{N-1}$ on the micro-scale. However since the velocity is half-time step forward with respect to the acceleration, the starting time of the micro-scale simulation is $t^{N-1+\frac{\Delta t^M}{2r_f}}$, where r_f indicates the refinement factor. However, the accelerations $\boldsymbol{a}^{N-1}$, in absence of

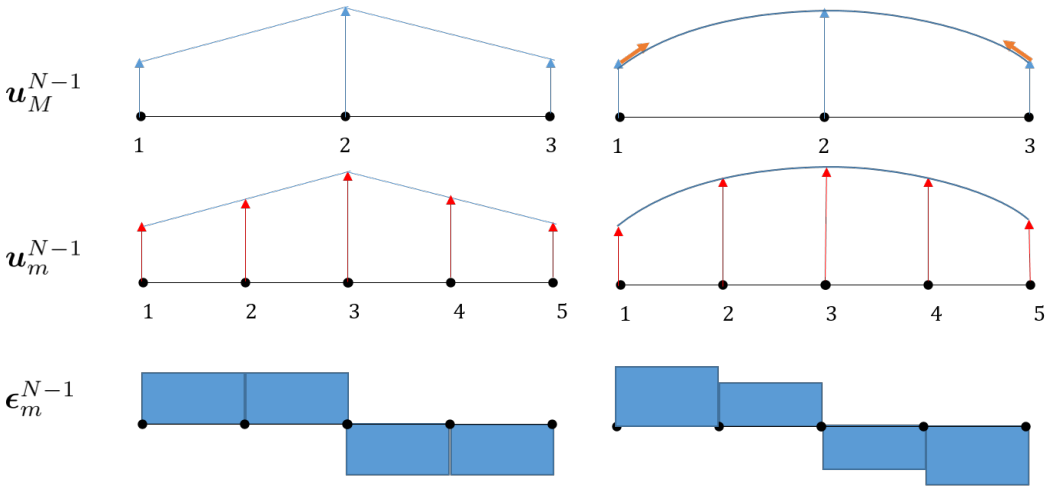

a) Linear shape Functions $\boldsymbol{N}$ a) Hermitian shape Functions $\boldsymbol{H}$

Figure 3.5: Comparison between hermitian and linear interpolation for refinement, in linear elastic elements. When using linear shape functions for the interpolation of the macro-displacements (blue arrows), the resulting elastic strain is constant over the micro-elements that share the same macro-element domain. When using hermitian shape functions, such situation is avoided, because of the use of nodal derivatives (orange arrows) resulting in a better interpolation of the elastic strain on the micro-mesh.

external forces, are computed from the stresses at $\boldsymbol{\sigma}^{N-1}$, therefore is legitimate to approximate the state at $t^{N-1+\frac{\Delta t^M}{2r}}$, with the one at t^{N-1}, as depicted in figure 3.4. To obtain consistent kinetic and kinematic quantities, one of the two sets has to be directly interpolated (e.g. kinematic), and the other one has to be derived (e.g. kinetic). This concept is clear with the example of figure 3.5. In this example two 1D elements with constant elastic strain are refined. If the displacement are linearly interpolated over the new mesh the elastic strain, and therefore the elastic stress will be constant over the refined elements that are contained in the same macro element as shown in picture 3.5a). This contradicts the hypothesis of linear interpolation of the stress. Using the hermitian interpolation proposed in the previous section, the lower scale elements can compute a C^3 displacements, and a C^2 elastic strain, which ensures a consistent interpolation of both kinetic and kinematic quantities, as shown in figure 3.5b) without the use of a balancing step.

At every macro-time step the dynamic nature of the problem is such that the macro-scale zones that present high error evolve in the macro-computational domain,

constantly shrinking or expanding. Such situation means that at the micro-scale there is a continuous addition and deletion of elements at each macro time-step. Therefore, the initialisation of the new data is needed only for the newly added elements, since the old micro-scale elements can inherit their previous solution. The computation of the coupling forces, at the end of every micro-scale update, both at the micro and macro scale over a coupling domain Ω_c, ensures the two ways communication between the domains. In particular the corrective forces $\boldsymbol{N}^T \boldsymbol{f}^m_{corr}$ are used to compute a corrected acceleration $\boldsymbol{a}^N_M$ and generate a corrected velocity $\boldsymbol{v}^{N+\frac{1}{2}}_M$.

3.2.7 Adaptive Framework

The proposed error estimation, data transfer and coupling scheme can be simultaneously used in a novel adaptive framework for concurrent multi-scale modelling of dynamic phenomena. The main advantages of the resulting methodology are multiple. To begin with, an efficient scheme is introduced to detect the size of the micro-scale domain based on the macro-scale solution, using only nodal quantities for each element. A consistent data transfer among the scales ensures the correct energy transfer, avoiding the use of a balance step solution. Finally, the proposed coupling scheme avoids the formation of numerical errors at the interfaces between the micro-scale mesh and the macro scale one. The proposed complete framework is outlined in box 3.

Flowchart 3. *Flowchart for adaptive concurrent explicit framework*

1. *Initialise macro mesh: set* $\boldsymbol{v}^M_0$,$\boldsymbol{\sigma}^M_0$
   $t^M = 0$, *compute* $\boldsymbol{M^M}$

   Macro Scale Update*:* $t^{N-1} \rightarrow t^N$, Δt^M

2. *Evaluate macro nodal forces* $\boldsymbol{f}^M_n$ *from equation 3.13*

3. *Evaluate macro accelerations*
   $\boldsymbol{a^M_N} = (\boldsymbol{M}^M)^{-1}(\boldsymbol{f}^{\boldsymbol{M,ext}}_N - \boldsymbol{f}^{\boldsymbol{M,int}}_N)$

4. *Update macro nodal velocities*
$$\boldsymbol{v}^M_{N+\frac{1}{2}} = \boldsymbol{v}^M_{N+\frac{1}{2}-\eta} + \eta \Delta t^M \{\boldsymbol{a}^M_N\} \; : \; \eta = \begin{cases} \frac{1}{2} & \text{if } N = 0 \\ 1 & \text{if } N > 0 \end{cases}$$

5. *Overwrite macro nodal velocity for enforced boundary conditions*

6. *Update macro nodal displacements*
$\boldsymbol{u}^M_{N+1} = \boldsymbol{u}^M_N + \Delta t^M \boldsymbol{v}^M_{N+\frac{1}{2}}$

7. *Check error condition for elements of macro scale*
$\frac{E_{el}}{U_{max}} > \zeta$

8. *Mark all elements that verify the error condition and their neighbours*

9. *If any element has been marked go to 10 otherwise go to 13*

10. *Generate micro-scale mesh*

11. *Inherit previous results or use Hermitian interpolation for the initialisation on the micro-scale of kinetic and kinematic quantities*
$\boldsymbol{u}^m_{n-1} = \boldsymbol{H}\boldsymbol{u}^M_{N-1}$
$\boldsymbol{v}^m_{n-\frac{1}{2}} = \boldsymbol{H}\boldsymbol{v}^M_{N-\frac{1}{2}}$
$\boldsymbol{\sigma}^m_{n-1} = \sum \int_{\Omega^m_e} \boldsymbol{E}\boldsymbol{B}\boldsymbol{u}^m_{n-1} dV$

***Micro Scale Update**: $t^{N-1} \rightarrow t^N$, Δt^m, refer to flowchart 2*

***Micro Scale Coupling over** Ω_C, refer to flowchart 2*

***Macro Scale Coupling over** Ω_C, refer to flowchart 2*

12. *Update macro scale counter and time*

13. *If macro scale simulation not complete go to 2.*

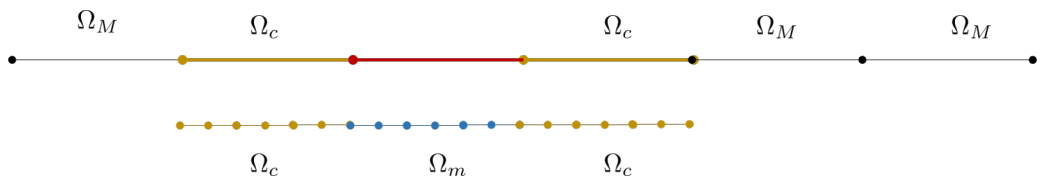

Figure 3.6: Transition of elements from macro to micro scale based on error detection. At every coarse time-step the error of every element is compared against a user input threshold. If any element has a high error it will be selected for refinement. The neighbouring elements of the original flagged ones are used for coupling purposes.

In summary at each macro scale time-step the error is computed over all the

elements of the macro-scale mesh. All those for which the error is higher than a predetermined threshold are refined at a smaller scale Ω_m, together with their neighbours that will be used to enforce the velocity continuity condition becoming the domain Ω_c. Such transition of coarse scale element from Ω_M to Ω_m or Ω_c is depicted in figure 3.6.

3.3 Verification

The reference problem that will be used to validate the numerical simulations in this chapter is depicted in figure 3.7.

It consists of a rod in which the cross sectional diameter D is smaller of its length L, loaded along its longitudinal axis. Under the hypothesis that each cross section of the rod remains plane during the motion an that the stress σ is uniform over it, the displacement of the particles along the rod can be expressed by a scalar function:

$$u = u(x, t), \tag{3.73}$$

in which u represents the displacement, x the position along the longitudinal axis and t is the time. The equilibrium of the body without considering body forces is given by Newton's second law:

$$\frac{\partial \sigma}{\partial x} = \rho \frac{\partial^2 u}{\partial t^2}, \tag{3.74}$$

in which ρ represents the material density. Under the assumption of elastic material, and relating the strain to the first spatial derivative of the displacement, the equilibrium equation can be expressed only as function of u:

$$c^2 \frac{\partial^2 u}{\partial x^2} = \frac{\partial^2 u}{\partial t^2}, \tag{3.75}$$

where

$$c = \sqrt{\frac{E}{\rho}}, \tag{3.76}$$

in which E represents the Young's Modulus of the material and c is the longitudinal wave speed in the material. The expression in 3.75 is a second-order linear hyperbolic

Figure 3.7: Reference Problem Configuration. A slender bar of length L, is subjected to a velocity boundary condition $V(t)$ while is free on the opposite face

partial differential equation for the description of wave propagation in longitudinal rods.

3.3.1 Analytical Approach

Equation 3.75, can be solved exactly by the D'Alembert's method. First, we introduce two new variables $\underline{\xi} = x - ct$ and $\underline{\eta} = x + ct$. The substitution of these variables in the original dynamic equilibrium equation leads to:

$$\frac{\partial^2 u}{\partial \underline{\xi} \partial \underline{\eta}} = 0. \tag{3.77}$$

The solution of the equation 3.77 can be expressed as:

$$u(\underline{\xi}, \underline{\eta}) = F(\underline{\xi}) + G(\underline{\eta}) = F(x - ct) + G(x + ct). \tag{3.78}$$

Equation 3.78, represents the general solution of the problem. The functions $F(x)$ and $G(x)$, can be obtained from the the boundary conditions. Before the reflection from the boundary it can be shown that the solution is:

$$v(x,t) = V(x - ct), \quad 0 \leq t \leq \frac{L}{c}; \tag{3.79}$$

where $V(t)$ represents the applied Neumann Boundary condition. The solution is therefore represented by a forward travelling wave with speed c. In particular, at any point in time and space the solution is represented by a shift of the initial conditions, as depicted in figure 3.8. For this reason the wave propagation in elastic rods is said to be non dispersive.

For forward travelling waves the stress can be derived as:

$$\sigma(x,t) = E\epsilon = E\frac{\partial u}{\partial x} = E[F'(x - ct)], \tag{3.80}$$

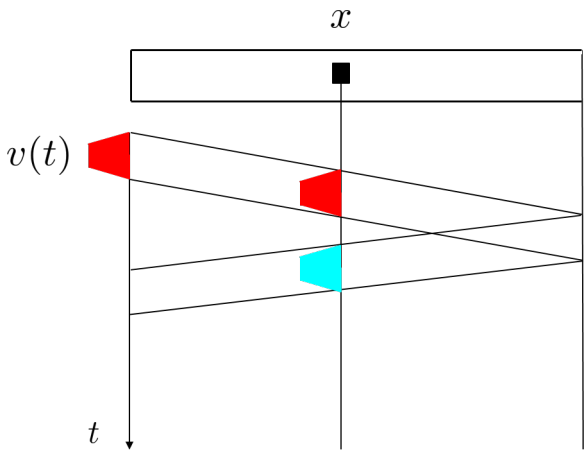

Figure 3.8: Analytical solution to the elastic one-dimensional wave propagation problem. At any point in time the solution is the combination of a forward and a backward travelling wave

.

while the velocity can be expressed as:

$$v(x,t) = \frac{\partial u}{\partial t} = -cF'(x-ct). \tag{3.81}$$

By eliminating $F'(x-ct)$ we obtain:

$$\sigma(x,t) = -\rho c v(x,t) \quad \text{for} \quad \frac{dx}{dt} = c. \tag{3.82}$$

Applying the same procedure for backward travelling wave we obtain:

$$\sigma(x,t) = -\rho c v(x,t) \quad \text{for} \quad \frac{dx}{dt} = -c. \tag{3.83}$$

Equations 3.82 and 3.83 describe the relationship between particle velocity and stress for forward and backward travelling waves. At the boundaries it is possible to show that:

- At a free end an incoming compressive (or tensile) stress wave is reflected as tensile (or compressive) stress wave of the same magnitude.

- At a fixed end an incoming compressive (or tensile) stress wave is reflected as compressive (or tensile) stress wave of the same magnitude.

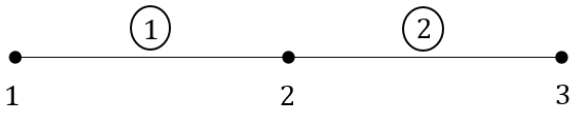

Figure 3.9: Element configuration for computation of error. The central node 2 can recover its nodal strain from its neighbouring elements.

Finally, the analytical solution can be summarized as follows: at any space and time the solution is represented by a forward compressive travelling wave, which is obtained shifting the initial condition with the variable $x - ct$. As a result of the boundary conditions, the wave will be reflected as tensile.

3.3.2 Hermitian interpolation based error estimator for one-dimensional mesh

In section 3.2.4 a novel hermitian interpolation based error estimator has been introduced. This section will validate the implementation and performances of such error estimator when applied one dimensional elements with constant strain and one integration point. At any moment in time, given the nature of the linear shape functions, the strains are constant over one element and discontinuous across element boundaries. A nodal continuous strain can be approximated considering two adjacent elements of length dx_1 and dx_2 comprised of the nodes 1,2,3 in element (1) and (2) as shown in figure 3.9.

Employing a classical central difference formula the nodal strain at location 2 can be approximated as:

$$\epsilon_2 = \frac{u_3 - u_1}{dx_1 + dx_2} = \frac{u_3 - u_1 + u_2 - u_2}{dx_1 + dx_2} = \frac{u_3 - u_2}{dx_1 + dx_2} + \frac{u_2 - u_1}{dx_1 + dx_2} = \epsilon_2^{(1)} + \epsilon_2^{(2)}, \quad (3.84)$$

in which the last equality in equation 3.84 is divided in the contributions coming solely from the elements (1) and (2) as $\epsilon_2^{(1)}$ and $\epsilon_2^{(2)}$ respectively. In such form the nodal strain is easier to compute and assemble. For every element i the nodal strain $\epsilon_j^{(i)}$ at node j can be transformed from the physical domain $x \in [x_j, x_{j+1}]$ to the physical element domain strain $\bar{\epsilon}_j^{(i)}(\xi),\ \xi \in [-1, 1]$ as:

$$\bar{\epsilon}_2^{\textcircled{1}} = \epsilon_2^{\textcircled{1}} detJ = \frac{u_2 - u_1}{2}\left(\frac{dx_1}{dx_2 + dx_1}\right), \tag{3.85}$$

in which $detJ = \frac{\ell_e}{2}$ represents the determinant of the Jacobian of the transformation from parent to physical domain, equal to half the element length ℓ_e. The nodal strain of equation 3.85 can be used to compute a higher order approximation of the displacement using an Hermitian interpolation, over the parent element domain, specialising equation 3.69 for one dimensional elements as:

$$u^*(\xi, t) = \{H_1 \quad H_2 \quad H_3 \quad H_4\} \begin{Bmatrix} u_1 \\ u_2 \\ \bar{\epsilon}_1 \\ \bar{\epsilon}_2 \end{Bmatrix}, \tag{3.86}$$

in which the hermitian interpolation matrix $\boldsymbol{H} = \{H_1 \quad H_2 \quad H_3 \quad H_4\}$ can be defined as:

$$\begin{cases} H_1 = \frac{1}{4}\xi^3 - \frac{3}{4}\xi + \frac{1}{2}, \\ H_2 = -\frac{1}{4}\xi^3 + \frac{3}{4}\xi + \frac{1}{2}, \\ H_3 = \frac{1}{4}\xi^3 - \frac{1}{4}\xi^2 - \frac{1}{4}\xi + \frac{1}{4}, \\ H_4 = \frac{1}{4}\xi^3 + \frac{1}{4}\xi^2 - \frac{1}{4}\xi - \frac{1}{4}. \end{cases} \tag{3.87}$$

Equation 3.86 represents a post-processed higher order displacement inside a element, from which a post-processed strain can be obtained by differentiation with respect to the variable ξ, computing the matrix $\boldsymbol{B}^H$ defined in equation 3.71 as:

$$\begin{cases} B_1^H = \frac{dH_1}{d\xi}\frac{d\xi}{dx} = (\frac{3}{4}\xi^2 - \frac{3}{4})\frac{d\xi}{dx}, \\ B_2^H = \frac{dH_2}{d\xi}\frac{d\xi}{dx} = (-\frac{3}{4}\xi^2 + \frac{3}{4})\frac{d\xi}{dx}, \\ B_3^H = \frac{dH_3}{d\xi}\frac{d\xi}{dx} = (\frac{3}{4}\xi^2 - \frac{1}{2}\xi - \frac{1}{4})\frac{d\xi}{dx}, \\ B_4^H = \frac{dH_4}{d\xi}\frac{d\xi}{dx} = (\frac{3}{4}\xi^2 + \frac{1}{2}\xi - \frac{1}{4})\frac{d\xi}{dx}. \end{cases} \tag{3.88}$$

For one dimensional element with a single integration point the equation 3.71 can be specialised computing 3.88 at the position of the integrations point (i.e. $\xi = 0$),

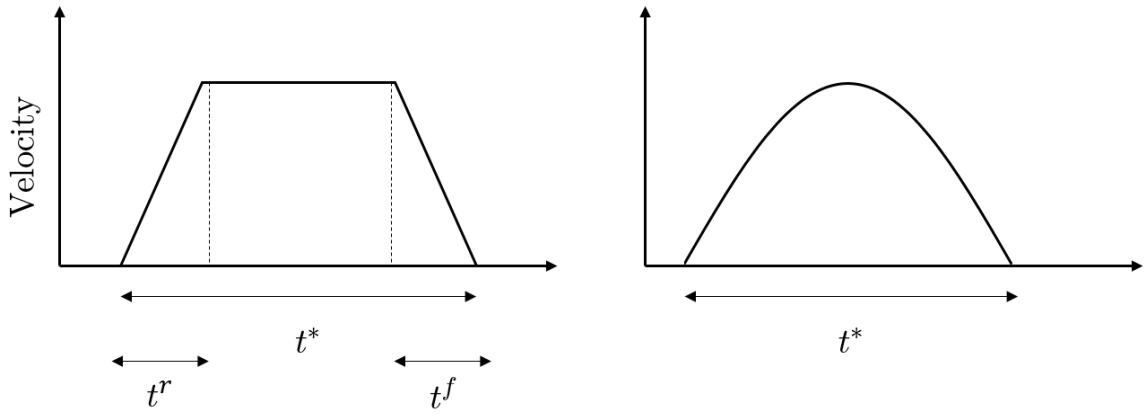

Figure 3.10: Representation of the trapezoidal (left) and sinusoidal (right) applied boundary conditions.

E	$207\,GPa$
ρ	$7.83e^{-6}\,\frac{kg}{mm^3}$
L	$1\,mm$

Table 3.1: Material and Geometrical properties used in the study of error estimation.

leading to:

$$\epsilon^* = \bar{\epsilon}^*(0,t)\frac{d\xi}{dx} = \begin{Bmatrix} B_1^H(0) & B_2^H(0) & B_3^H(0) & B_4^H(0) \end{Bmatrix} \begin{Bmatrix} u_1 \\ u_2 \\ \bar{\epsilon}_1 \\ \bar{\epsilon}_2 \end{Bmatrix} = \left(-\frac{3}{4}u_1 + \frac{3}{4}u_2 - \frac{1}{4}\bar{\epsilon}_1 - \frac{1}{4}\bar{\epsilon}_2\right)\frac{2}{\ell_e}. \tag{3.89}$$

The post-processed strain from equation 3.89 can be substituted in equation 3.66 to obtain the elemental error at time t. The energy norm of the error over the whole mesh is defined starting from the element contribution $\widetilde{e}_\epsilon(t)$ as in equation 3.72.

The proposed error estimation procedure is validated against the analytical solution of the reference problem using two different excitation functions $V(t)$, namely trapezoidal and sinusoidal pulse on the same system. The material and geometrical properties used for the simulations are summarised in table 3.1.

In the first case a trapezoidal velocity pulse whose total duration time is equal to $t^* = \frac{L}{8c}$ and its rise and fall time are equal $t^r = t^f = \frac{L}{80c}$, as depicted in figure 3.10. The wave is propagated through different mesh with increasing number of nodes and

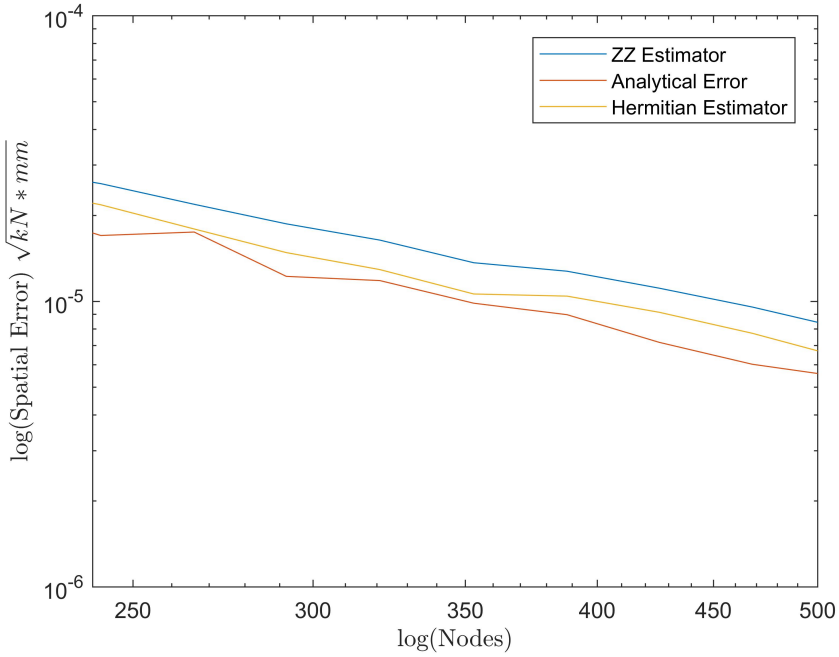

Figure 3.11: Rate of convergence for different error estimators and trapezoidal boundary condition at $t = 0.8 * \frac{L}{c}$. The hermitian error estimator presents the same convergence rate of the ZZ estimator and is close to the analytical error on the considered mesh.

E	$3.4\,GPa$
ρ	$1.2\,\frac{g}{cm^3}$
L	$1\,mm$

Table 3.2: Material and Geometrical properties used in the study of the coupling properties.

the error over the whole mesh is compared with different techniques. In particular, the analytical (true) error in figure 3.11 is relative to the difference between the finite element and the analytical solution of the problem. The ZZ estimator, computes the error between the finite element and the post-processed solution as in [79]. Finally, the novel hermitian estimator computes the error as the difference between the finite element solution and the hermitian post-processed interpolation of the strains in equation 3.89. The results reported in figure 3.11 at time $t^c = 0.8\frac{L}{c}$. In the second case a sinusoidal pulse whose total duration time is equal to $t^* = \frac{L}{16c}$, as depicted in figure 3.10, is analysed with the same technique and the results are resumed in figure 3.12. In both cases an increased number of nodes reduces the error against the

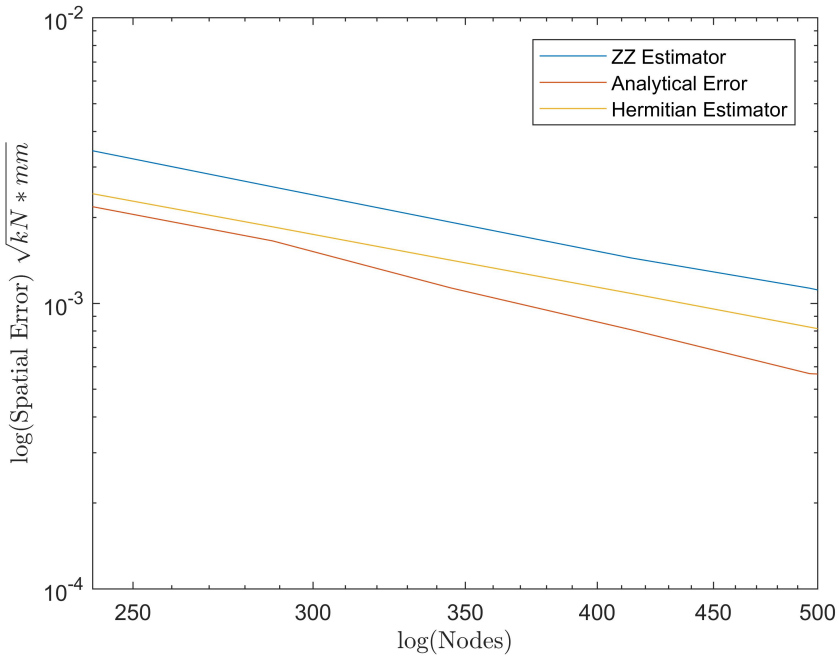

Figure 3.12: Rate of convergence for different error estimators and sinusoidal boundary condition at $t = 0.8 * \frac{L}{c}$. The hermitian error estimator presents the same convergence rate of the ZZ estimator and is close to the analytical error on the considered mesh.

analytical solution. From a quantitative point of view the rate of convergence was found to be of order $\mathcal{O}(N^{1.5})$, with N nodes in the mesh. Such convergence rate is equal to the ZZ estimator and the analytical one.

3.3.3 Coupling Properties

The high frequency dissipation of the framework, demonstrated analytically in section 3.2.3 can be evaluated numerically against the reference problem introduced in section 3.3.1. In this case the computational domain is divided in three different areas as depicted in figure 3.13. The material and geometrical properties for this simulations are reported in table 3.2. A half of the bar length is discretised with element of length $\ell_e^M = \frac{1}{100}L$, while the second half is discretised with finer elements of length $\ell_e^m = \frac{1}{1000}L$. The continuity condition in terms of velocities in enforced over a coupling length of size $16 * \ell_e^M$.

Between the two scales a coupling zone is defined a priori where the velocity

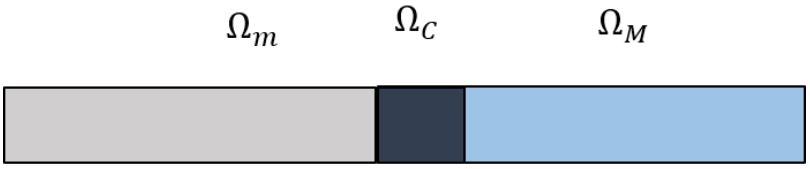

Figure 3.13: Bar Coupled Model. The slender bar is partitioned a priori in a coarse Ω_M, fine Ω_m and coupling domain Ω_c

continuity is enforced. In these examples a velocity boundary condition is applied on the last node of the fine scale, as:

$$V(t) = \bar{V(t)} + V(t)', \tag{3.90}$$

in which $\bar{V(t)}$ represents the low frequency content, a trapezoidal pulse whose total duration time is equal to $t^* = \frac{L}{24c}$ and its rise and fall time are equal $t^r = t^f = \frac{L}{8c}$. $V(t)'$ represents the high frequency content modelled as a sinusoidal pulse of same duration of the trapezoidal pulse, and frequency of $f = \frac{c}{10\ell_e^m}$. Since $\ell_e^M = 10\ell_e^m$, because of how the mesh is constructed we have that $f = \frac{c}{\ell_e^M} = f_c^M$ where f_c^M is the cut-off frequency of the coarse scale domain. Therefore the fine scale is able to represent both the low and the high frequencies content as shown in figure in 3.14, while the wave is moving in the fine part of the domain. The coupling zone effectively behaves like a filter on which the wave adapts to the coarse scale frequencies as shown in figure 3.15, when the wave has already passed through the coupling zone, and it is totally contained in the coarse scale domain.

The conservation properties of the coupling zone can be appreciated in figure 3.16, where the kinetic energy in the computational domain is divided in the coarse and fine scale contribution. The kinetic energy is computed as the sum of the contribution from the two domains, therefore its values are valid only when the wave its completely enclosed in the coarse or the fine scale. A correct interpretation of the values of the energies in the coupling zone should consider as well the weighting parameters. In particular the kinetic energy in the fine scale domain portion is zero, then it grows until it reaches a maximum and decreases when the energy is transferred to the coarse

scale domain. On the coarse scale domain the kinetic energy shows a similar trend, however the maximum value achieved is smaller than the original one from the fine scale domain. Such dissipation in the frequencies higher than the cut-off frequency of the coarse scale domain (high frequencies) is beneficial to avoid the generation of spurious wave reflections, however dissipation in the low frequency band regime, might alter significantly the energy transfer between the different domains. To assess the frequency band in which the dissipation is more predominant the power dissipated in the coupling zone will be compared to the power in the fine scale, in the frequency domain. The analysis of the velocity response of the nodes inside Ω_c can help assess the frequency bands in which the dissipation if predominant. The power dissipated in the coupling zone is defined in equation 3.62, while the sum of the internal and kinetic powers in the fine zone only can be derived from the equations 3.59 and 3.57. The energy spectral density spectrum of the dissipated power, as in [100], is defined as the square of the magnitude of the frequency spectrum, $\mathcal{P}_{diss}(f_k)$, in the discrete frequency f_k as:

$$S_{diss}(f_k) = ||\mathcal{P}_{diss}(f_k)||_c, \tag{3.91}$$

in which $||(\cdot)||_c$ represents the norm of the complex number $(\cdot)$. The computation of $\mathcal{P}_{diss}(f_k)$ in 3.91 is performed from the original discrete signal in time $P_{diss}(t)$. In particular, in the fine scale domain the dissipated is sampled with time Δt^m. The discrete Fourier transform of the power in the coupling zone can be expressed as:

$$\mathcal{P}_{diss}(f_k) = \sum_{j=0}^{j=N-1} P_{diss}((j+1)\cdot\Delta t^m) e^{-i2\pi f_k j \Delta t^m}, \tag{3.92}$$

in which i represents the imaginary unity, N the number of samples for the power $P_{diss}(t)$ and f_k represents a discrete frequency defined as

$$f_k = \frac{k}{N\Delta t^M} \quad k \in 0 \dots N-1. \tag{3.93}$$

The quantity $\frac{1}{N\Delta t^M}$ is defined as the resolution of the discrete Fourier transform, and for the analysis in this section it will be fixed and connected to the fine scale time

domain step domain. The computation of the discrete Fourier transform is performed using the Fast Fourier Transform (FFT) algorithm implemented in MATLAB. The same procedure can be applied to compute the Fourier transform of the total power $\mathcal{P}_{tot}(t)$, as the sum of the nternal and kinetic power, in Ω_f, to obtain $\mathcal{P}_{tot}(f_k)$ and subsequently the energy spectal density $S_{tot}(f_k)$. To assess the frequency band in which the dissipation is predominant, for every discrete frequency an index of dissipated power dissipated can be computed as:

$$S(f_k) = \frac{S_{diss}(f_k)}{S_{tot}(f_k)}, \tag{3.94}$$

in which $0 \leq S \leq 1$. A value of 0 means that there is no dissipation for that frequency, while a value of 1 means that all the energy in that frequency has been dissipated by the coupling. The percentage of the dissipated power at each frequency is shown in picture 3.17. The graph is clearly separated in two areas: a low frequency regime (generated by the trapezoidal pulse) and a high frequency regime close to the cut-off frequency of the coarse scale domain (generated by the truncated sinusoidal pulse). The FFT analysis is valid because the frequency of interests, where the energy is concentrated are in the coarse scale regime, while the sampling frequency is connected to the fine scale stable time-step. In the high frequency regime the strong dissipation confirms the absence of spurious wave reflections as shown in 3.15. At the same time, in the low frequency regime the dissipation is weaker but it still results in a smaller total energy transferred to the coarse scale domain as shown in 3.16.

3.3.4 Parametric study of the coupling properties

The parametric study conducted in this section shows the convergence properties of the coupling framework proposed. The relevant parameters for the coupling are the extension of the coupled section Ω_C and the weighting function α_m. The general shape of α_m is modelled as:

$$\alpha_m = \left(\frac{\xi_c}{\ell_c}\right)^{\gamma}, \tag{3.95}$$

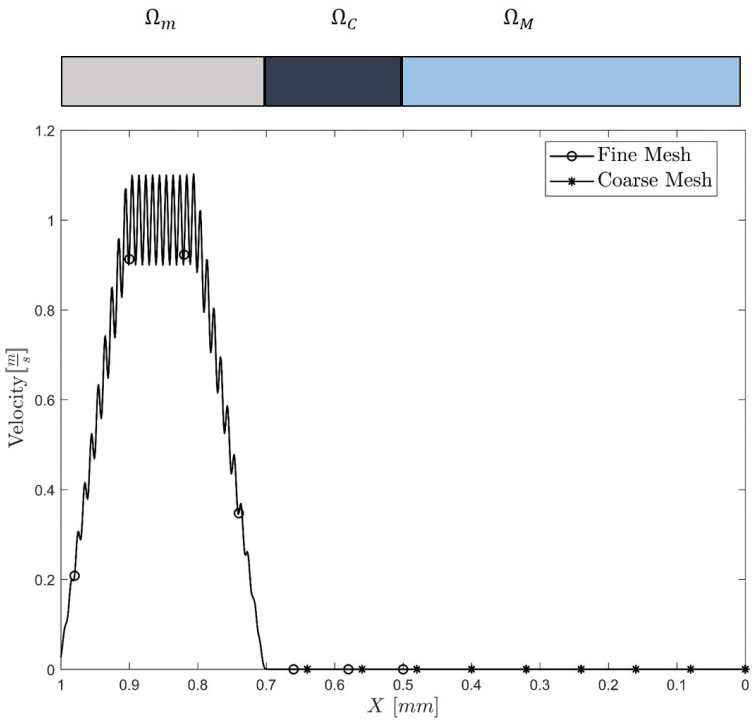

Figure 3.14: Elastic wave propagation at t= $0.5\frac{L}{c}$ for coupled model. The fine scale domain (left) is able to represent the low and high frequency content of the velocity boundary condition applied.

in which ξ_c is the axis who has its origin on the fine-to-coarse interface and points towards the coarse-to-fine interface and ℓ_c is the length associated to Ω_c. The particular of the form in equation 3.95 makes it suitable to describe a range of different couplings: constant when $\gamma = 0$, linear when $\gamma = 1$ and polynomial for $\gamma > 1$. In this study two different values of γ are examined; $\gamma = 1$ which corresponds to a linear weighting function α_m^L and $\gamma = 2$ which corresponds to a power-law weighting function α_m^P. Furthermore, for every α_m four different coupling lengths ℓ_c are selected corresponding to 2,4,8 and 16 times ℓ_e^M.

The simulations are compared in terms of particle velocity along the bar at t= $0.8\frac{L}{c}$ (figures 3.18 and 3.21), total energy of the system during the analysis (figures 3.19 and 3.22) and dissipation properties for linear and power coupling weighting functions respectively. Moreover following the approach presented in section 3.3.3, the simulations are compared in terms of the energy spectral density of the fine nodes

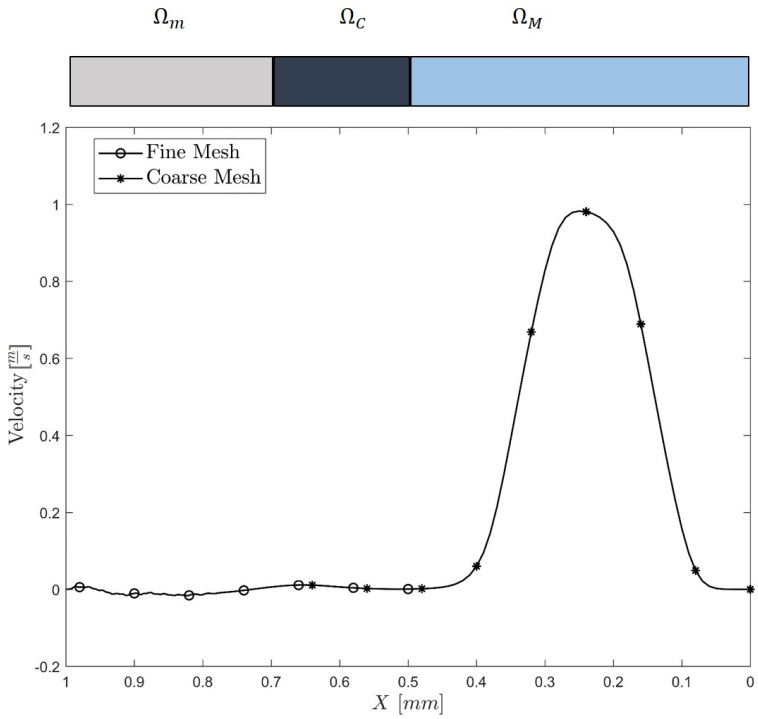

Figure 3.15: Elastic wave propagation at t= $0.8\frac{L}{c}$ for coupled model. The coarse scale domain (right) can only represent the low frequency content of the velocity boundary condition applied. However the high frequency is mostly dissipated through the coupling condition.

in the coupling and in the fine zone.

Figure 3.18 compares the predictions obtained for the linear weighting function over different coupling lengths and shows that there is a minimum value of coupling length required to properly filter the high frequency wave at the interface between the coarse and the fine scale and, therefore, to avoid the generation of a spurious wave reflection trapped in the fine scale domain. At the same time, while the rising and falling time of the trapezoidal pulse are correctly transferred, it is interesting to notice that the amplitude of the trapezoidal pulse is not correctly propagated to the coarse scale domain. This behaviour is reflected in the total energy as shown in picture 3.19, where the amount of energy transferred to the coarse scale decreases as the coupling length is shortened, and such energy is trapped in the fine scale domain, in the form of spurious wave reflections. Moreover, a bigger coupling length results simultaneously, in a better transfer of the low frequency content at coarse fine scale

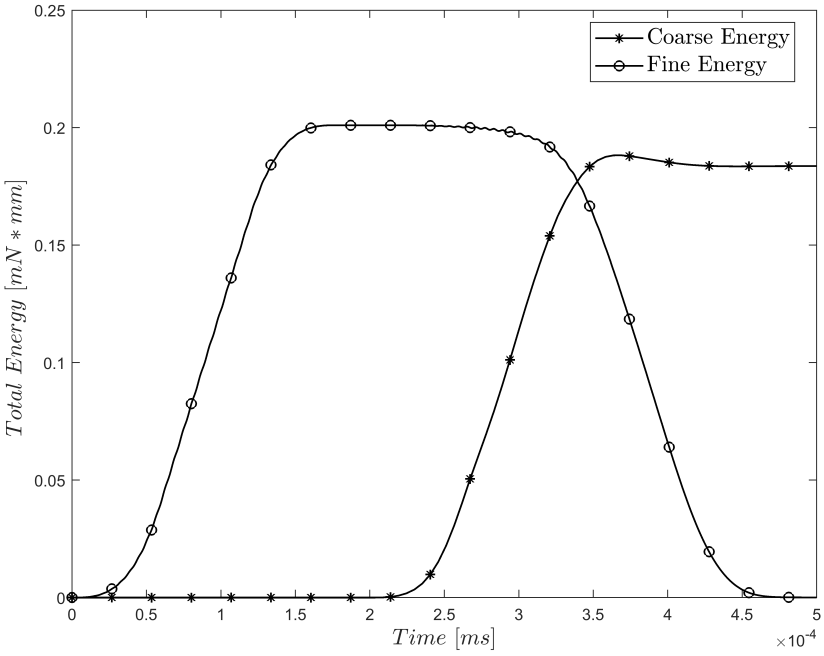

Figure 3.16: Evolution of the total energy for the coupled problem. The micro-scale total energy is initially zero, then it reaches a maximum and decreases when the energy is transferred to the coarse scale domain. The high frequency content of the energy is dissipated, but its contribution to the total energy is negligible.

and in a stronger dissipation in the coarse scale. Such effect however, is beneficial for the spurious wave reflection generation. Therefore, increasing the coupling length results in a clearly convergent framework where the energy dissipation only affects the high frequencies. The quantitative analysis of such dissipation can be carried out, for every coupling length, as outlined in section 3.3.3. The results are summarised in figure **??**, where different trends can be observed. In particular, increasing the coupling length the dissipation at low frequencies regime is weakened, enhancing the passage of low frequency content from fine to coarse scale. This behaviour can be observed in the spatial domain in figure 3.18, where the trapezoidal pulse at the coarse scale is better represented with increasing coupling length. At the some time the dissipation at frequencies close to the cut-off frequency of the coarse domain is more effective with bigger coupling lengths. This behaviour results in less spurious wave reflection in the fine scale domain as shown in picture 3.18.

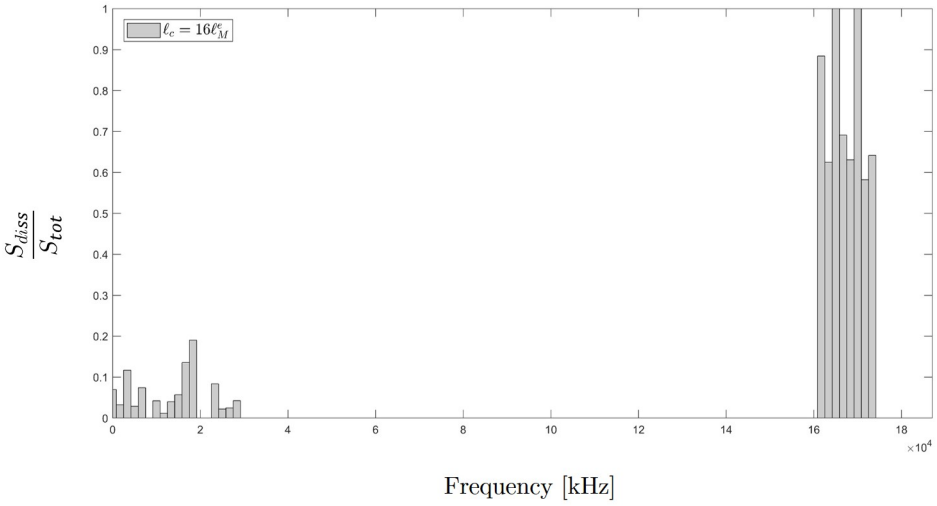

Figure 3.17: Ratio of the Energy Spectral Density (ESD) of the dissipated and total power, for linear coupling and 16 coarse scale elements in the coupling zone. The dissipation is more important at frequencies closer to the cut-off frequency of the coarse domain.

When using a weighting power law, similar trends are observed, therefore a bigger coupling length has a beneficial effect on the filtering of the high frequencies as shown in picture 3.21. Figure 3.22 shows that the transfer of total energy from micro to macro-scale is less affected by the coupling length when using a power law. Such effect is confirmed by the analysis in the frequency domain resumed in picture 3.23. The conclusions of such analysis is coherent with the previous observations: higher coupling lengths lead to smaller dissipation at the low frequency regime and to higher dissipation in the high frequency regime. However, when comparing the linear and the power law dissipation in the frequency domain, both of these behaviours are more pronounced, ultimately resulting in a better energy transfer and less spurious wave generation for the power law case.

Figure 3.24 compares power law and linear coupling for a coupling length of $8*\ell_e^M$ in which the use of the power law results in a better dissipation of the high frequencies as well as a better representation of the pulse at the coarse scale. When comparing the total energies in 3.25, this effect is clear at the macro scale where the artificial energy dissipation is lower when using the power function. The conclusion of the parametric study shows that the use of the coupling layer results always in a con-

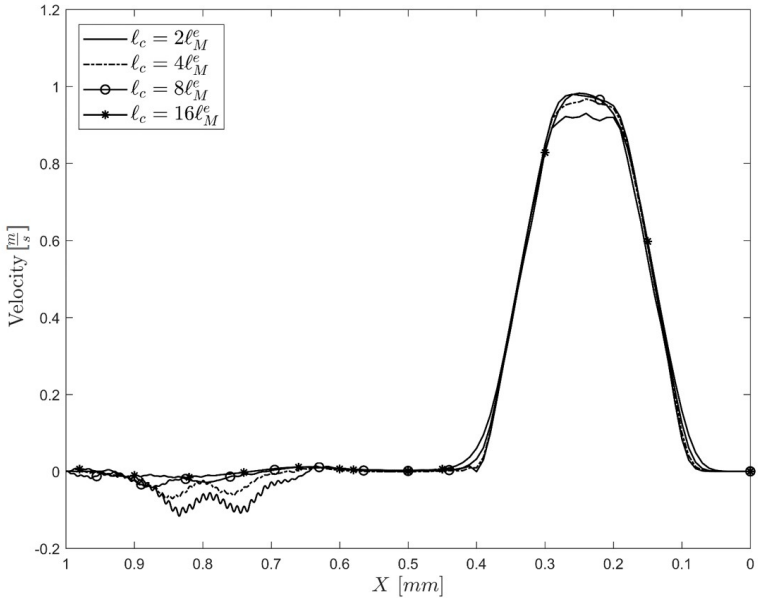

Figure 3.18: Elastic wave propagation at t= $0.8\frac{L}{c}$ for linear weighting function at different coupling length. When the coupling length is increased the fine scale domain presents less spurious oscillations. At the same the trapezoidal pulse is better transferred to the coarse scale domain.

vergent behaviour, dissipating only some relatively high frequencies that cannot be represented at the coarse scale. However the dissipative frequencies of the coupled domain can be tuned using an ad-hoc weighting function that can results in better transfer of the energies between the two domains.

3.3.5 Adaptive dynamic concurrent multi-scale 1D framework

The numerical implementations and performances of the building blocks of the dynamic concurrent multi-scale framework have been numerically investigated in section 3.3.3 and 3.3.2 for one dimensional elements with one integration point. The defined error estimator and the coupling among different scales can be used in the adaptive concurrent multi-scale framework defined in flowchart 3. The geometrical and material properties of the modelled bar are resumed in table 3.2, and the initial mesh has a constant element size of $\ell_e = \frac{1}{100}L$. The applied velocity boundary

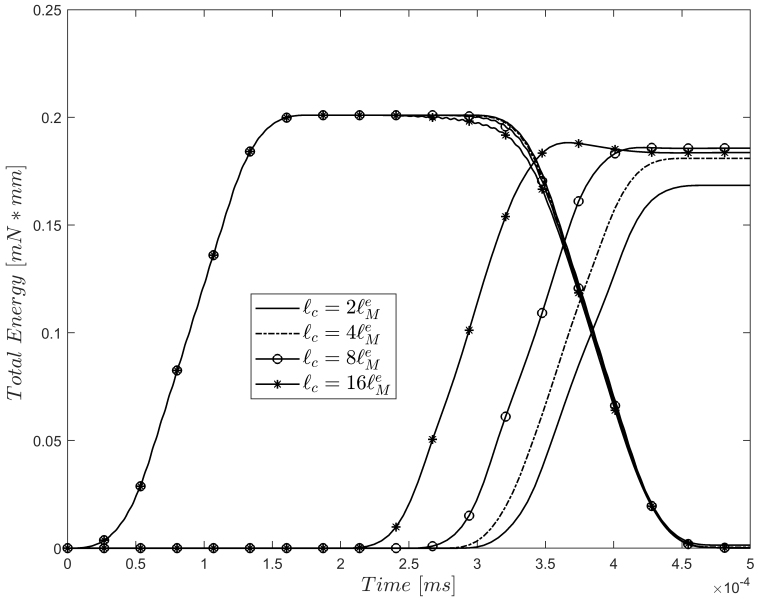

Figure 3.19: Total energy in coarse and fine scale domain when using a linear weighting function and different coupling lengths. The amount of energy trapped in the fine scale domain is negligible compared to the total energy, however when using small coupling lengths, there is a stronger energy dissipation.

conditions are defined in section 3.3.2 and correspond to two waveforms, namely a trapezoidal and a quarter of sinusoidal pulse.

At every coarse time-step of the simulation the error is assessed on the coarse scale based on the actual coarse scale kinetic properties. In figure 3.26, for the case of the trapezoidal pulse the single scale solution in red presents a significant amount of error in form of numerical oscillations. Such error is effectively captured by the devised error estimator, and corrected at a lower scale with a refinement factor of 10. The black dots in figures 3.26, 3.27, 3.28 and 3.29, show the size of the fine scale domain at that coarse scale time-step. The proposed data transfer schemes and coupling among the scales do not generate spurious wave oscillations, and retain the correct shape of the wave even after the reflection as shown in figure 3.27. Similar conclusions can be drawn in the case of a sinusoidal pulse in which the size of the fine scale domain generated at every coarse time-step is still comparable to the width of the pulse. In figure 3.28, even if the amount of numerical error is smaller, the fine

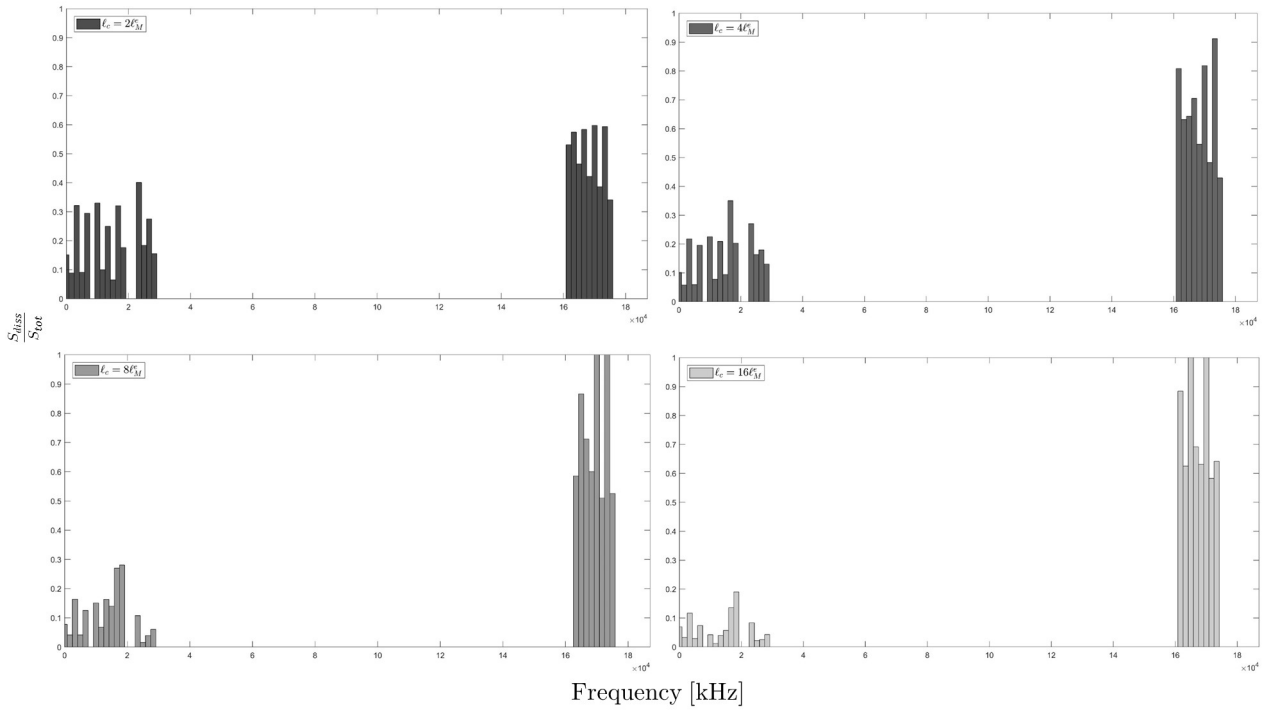

Figure 3.20: Energy dissipation index as defined in equation 3.94 for linear weighting function at different coupling lengths. Increasing the length of the coupling zone has a double beneficial effect. On the one hand, the low frequency content is retained, because of the smaller dissipation at higher coupling lengths, leading to a better transfer of energies between macro and micro scale. On the other hand, the high frequency content is more effectively dissipated resulting in the absence of spurious wave generation.

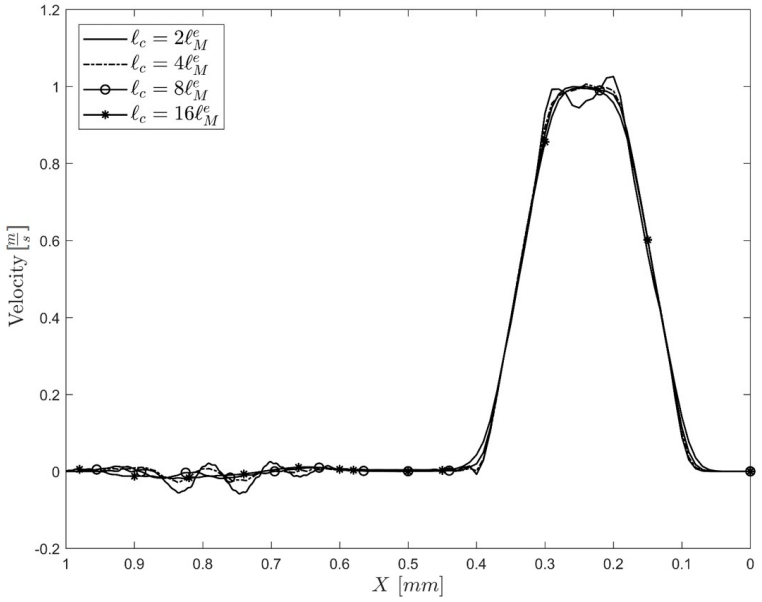

Figure 3.21: Elastic wave propagation at t= $0.8\frac{L}{c}$ for power law weighting function at different coupling length. When increasing the coupling length, the fine scale domain presents less spurious oscillations. At the same time the trapezoidal pulse is better transferred to the coarse scale domain.

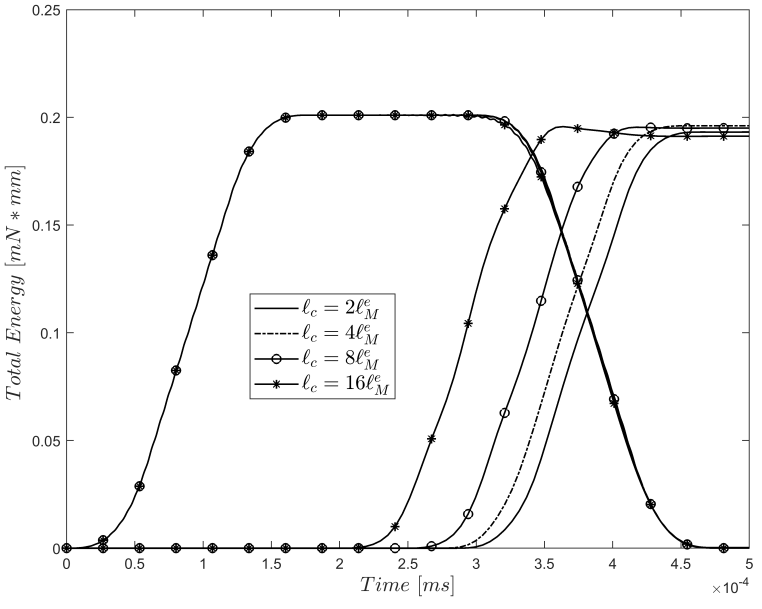

Figure 3.22: Total energy in coarse and fine scale domain when using a power law weighting function and different coupling lengths. The amount of energy trapped in the fine scale domain is negligible compared to the total energy, however when using small coupling lengths, there is a stronger energy dissipation.

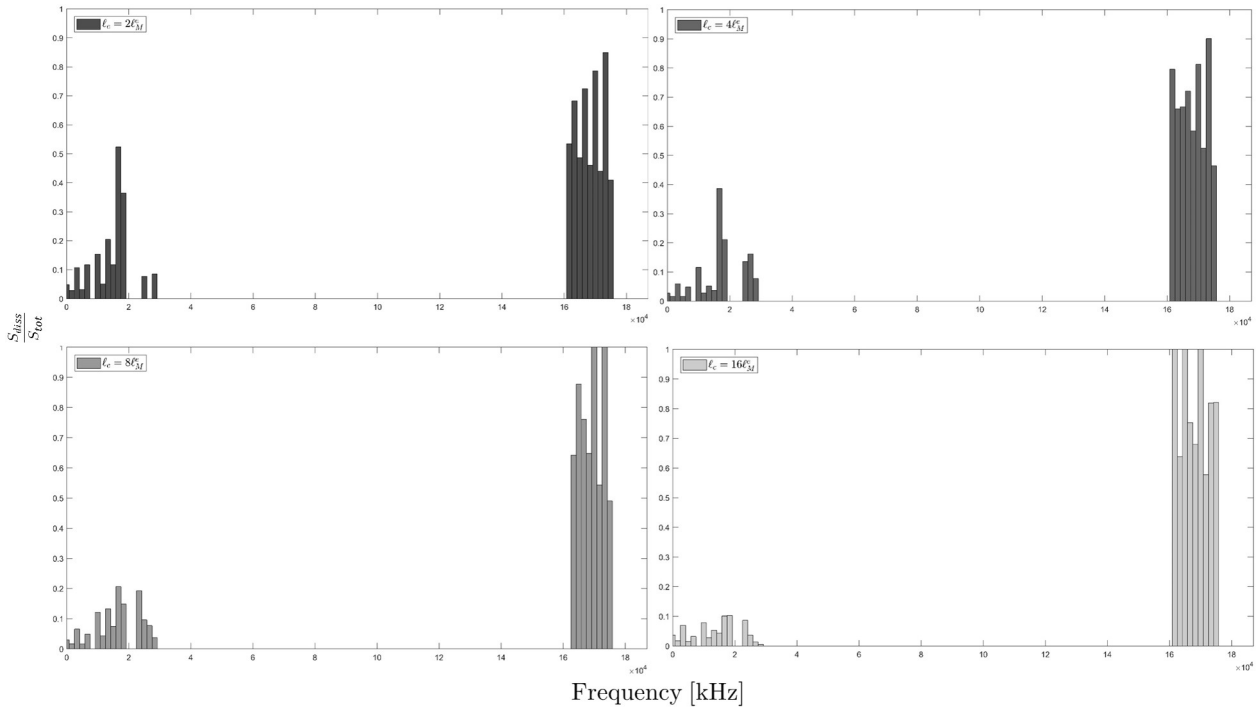

Figure 3.23: Energy dissipation index as defined in equation 3.94 for power law weighting function at different coupling lengths. Increasing the length of the coupling zone has a double beneficial effect. On the one hand, the low frequency content is retained, because of the smaller dissipation at higher coupling lengths, leading to a better transfer of energies between macro and micro scale. On the other hand, the high frequency content is more effectively dissipated with resulting in the absence of spurious wave generation.

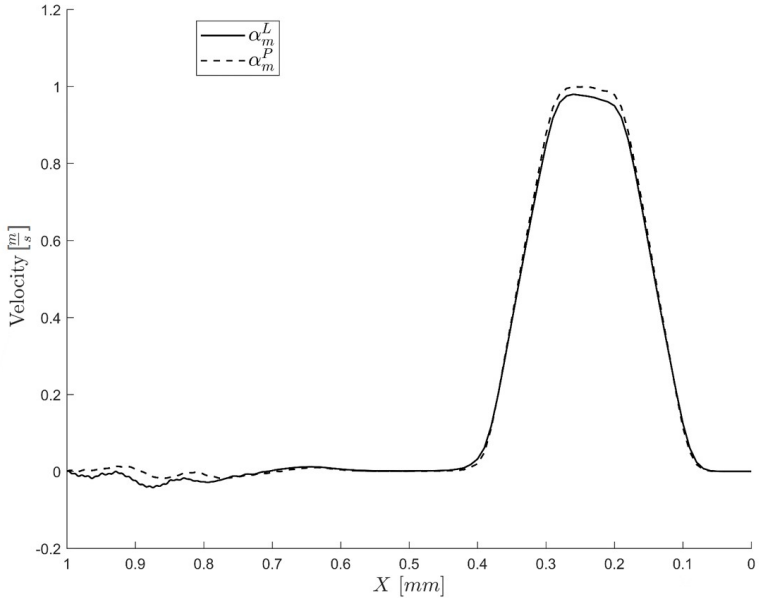

Figure 3.24: Elastic wave propagation at t= $0.8\frac{L}{c}$ for power law and linear weighting function using the same coupling length of $8^*\ell_M^e$. The use of the power law weighting function decreases the amount of spurious wave reflection and transfers more accurately the trapezoidal pulse at the coarse scale.

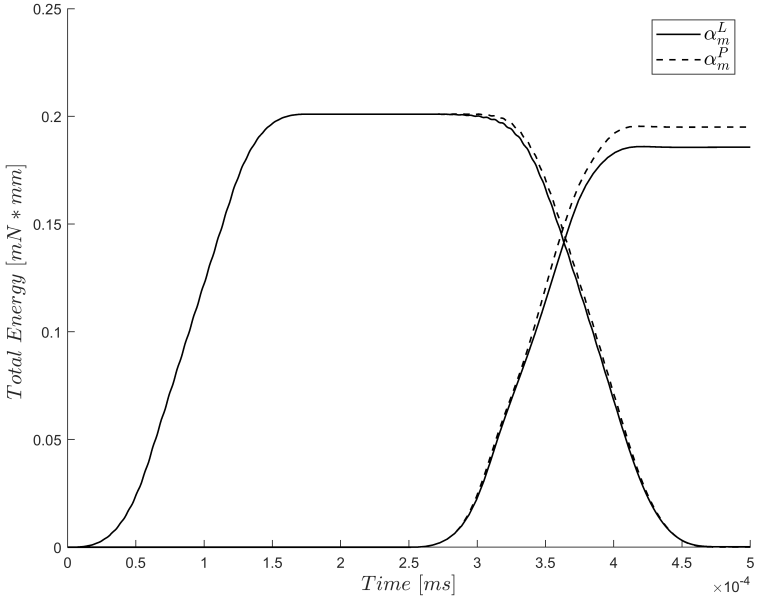

Figure 3.25: Total energy in coarse and fine scale domains when using power law and linear weighting functions. The use of the power law weighting function transfers more accurately the energy at the macro-scale domain, resulting in less energy dissipation.

scale is still activated and the error corrected, even after the reflection as shown in figure 3.29. Following the approach outlined in section 3.2.5, it is possible to define an error using the nodal velocities of the FEM solution and the analytical solution of equation 3.3.1. The error on the nodal velocities can be defined as:

$$\boldsymbol{e}_v(\boldsymbol{x},t) = \boldsymbol{v}(\boldsymbol{x},t) - \boldsymbol{v}_h(\boldsymbol{x},t), \tag{3.96}$$

in which $\boldsymbol{e}_v$ represents the error at every nodal position between the finite element solution $\boldsymbol{v}_h(\boldsymbol{x},t)$ and the analytical solution $\boldsymbol{v}(\boldsymbol{x},t)$. In this section non post-processing will be applied since the analytical solution is readily available. The energy norm of this error, $||(\cdot)||$, as defined in section 3.2.5, using matrix notation is equal to:

$$||\boldsymbol{e}_v(t)|| = \boldsymbol{e}_v(\boldsymbol{x},t)^T \boldsymbol{M} \boldsymbol{e}_v(\boldsymbol{x},t), \tag{3.97}$$

in which the norm has the dimensions of energy, and is zero when the FEM solution is equal to the analytical solution, and non-zero otherwise. It is important to notice that this error has only a time dependency since it encapsulates in the sum the spatial dependency. Equation 3.97 is computed for the mono and multi-scale simulations, using mono and multi-scale computed velocities, respectively. In figures 3.30 and 3.31 the improvement of the multi-scale simulation is noticeable. In particular, while the mono-scale simulation exhibits a growing error over time, the multi-scale simulation, in both cases, shows a smaller error almost constant over time.

3.4 Concluding remarks

This chapter has described the mathematical framework of a novel adaptive dynamic concurrent multi-scale approach. Wave propagation in solids can be treated mathematically as a hyperbolic partial differential equation in its strong form. However,when discretised in time and space, while the hyperbolic nature of the problem is preserved, numerical errors are introduced. While different methodologies have been proposed in literature to couple several computational domains using overlapping techniques, the formulation of an efficient coupling is still an open research field.

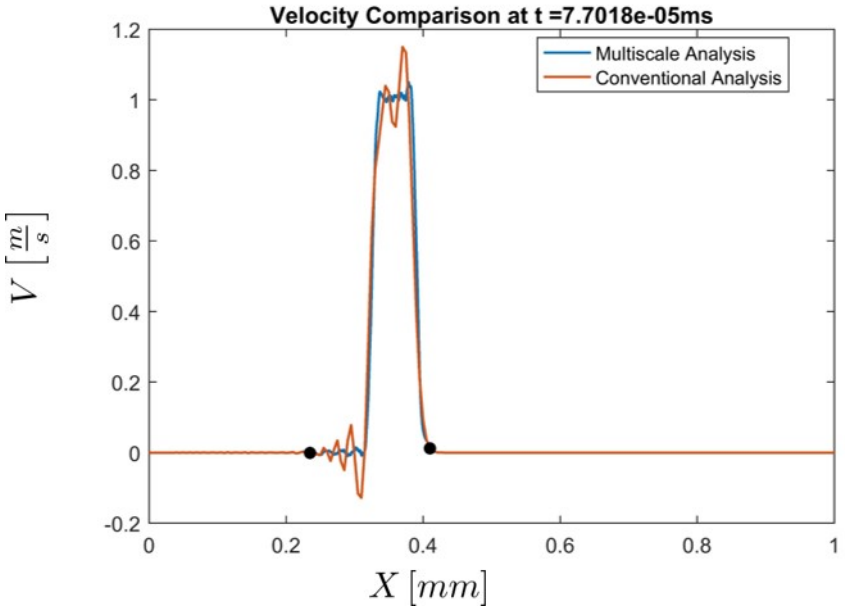

Figure 3.26: Comparison of conventional and multi-scale analysis for trapezoidal pulse case. The multi-scale simulation presents qualitatively a smaller numerical error.

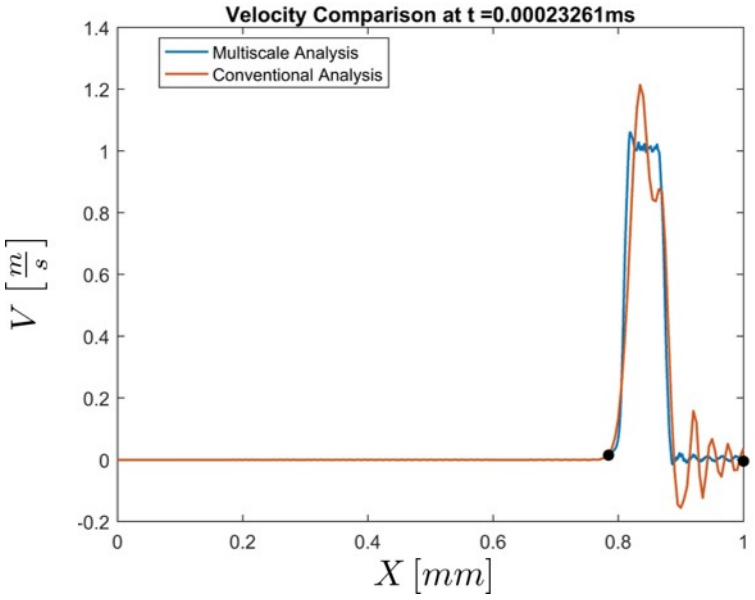

Figure 3.27: Comparison of conventional and multi-scale analysis for trapezoidal pulse case after the reflection from the free boundary. The simultaneous effect of data transfer and coupling does not affect the shape of the wave.

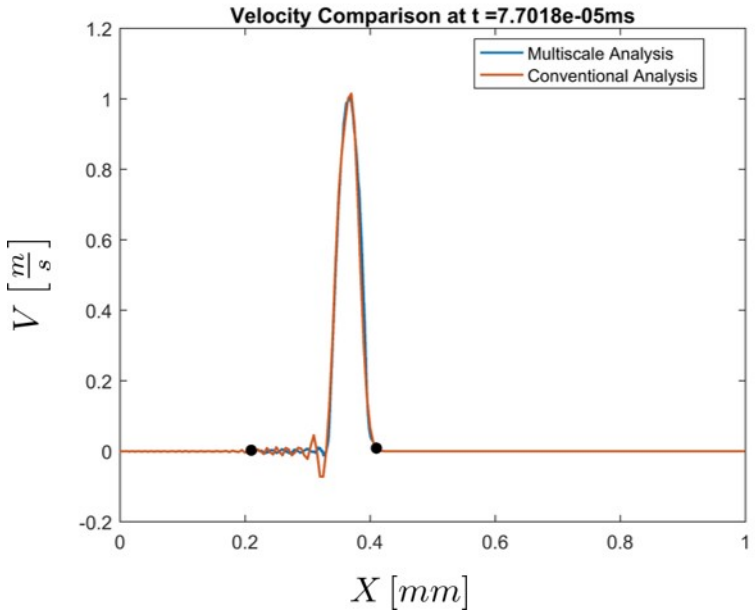

Figure 3.28: Comparison of conventional and multi-scale analysis for sinusoidal pulse case. The multi-scale simulation presents qualitatively a smaller numerical error.

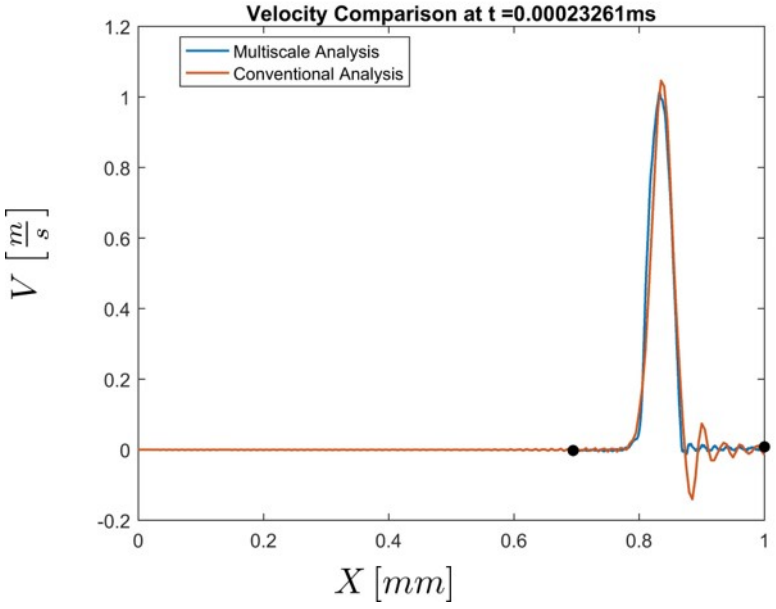

Figure 3.29: Comparison of conventional and multi-scale analysis for sinusoidal pulse case after the reflection from the free boundary. The simultaneous effect of data transfer and coupling does not affect the shape of the wave.

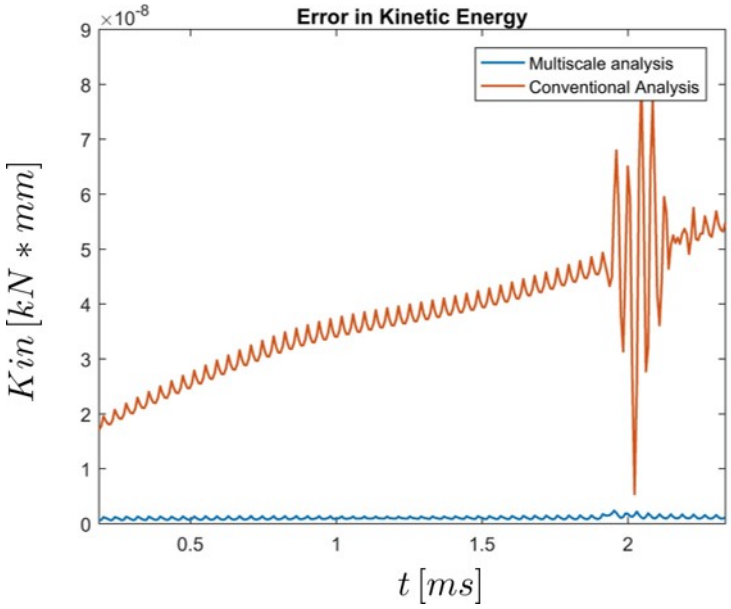

Figure 3.30: Comparison of the error in the case of conventional and multi-scale simulation for trapezoidal pulse computed from analytical solution. The error of the multi-scale simulation is sensibly reduced.

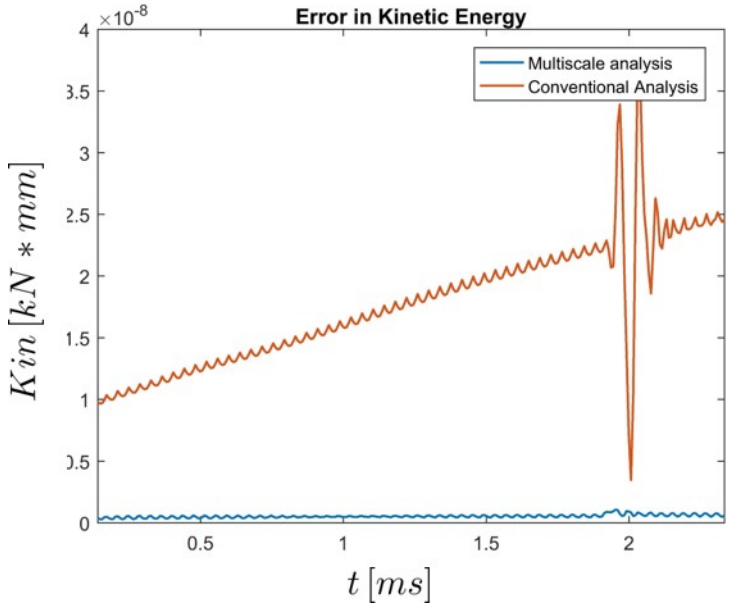

Figure 3.31: Comparison of the error in the case of conventional and multi-scale simulation for sinusoidal pulse computed from analytical solution. The error of the multi-scale simulation is sensibly reduced

In this chapter two main improvements have been presented for the formulation of a coupling condition between two differently discretised domains. The first one regards the application of the weighting functions after the discretisation in time and space, allowing the use of arbitrarily continuous elements while retaining the original eigenvalues (as well as conditional stability properties), of the computational mesh as if no coupling was applied. Subsequently an explicit formulation of the coupling is proposed that does not require the resolution of a system of equations. It is proved that such coupling is dissipative, with a stronger influence in the range of frequencies not representable by the coarsest scale in the model. The developed coupling scheme has been subsequently used in an adaptive framework in which a novel Hermitian interpolation based error estimator is used, allowing for a fast error detection on the computational mesh. The results on different simulations show that the proposed error estimation can be used to efficiently detect the areas of the coarse scale model that need refinement. Moreover the coupling among the scales avoids spurious wave oscillations intrinsic of adaptive dynamic finite element simulations. Lastly, the data transfer scheme constructed allows a consistent transfer of information among the micro and macro-scale reducing significantly the error of a conventional mono-scale simulation.

The implementation of this novel framework in a three-dimensional setting are not trivial. In first instance a complete third order polynomial in three dimensions is formed by 64 coefficients, while the combined conditions on the displacements and the derivatives of the displacements for a hexahedron sum up to only 32 coefficients. Moreover, the refinement of hexahedrons involves the generation of complex meshes that can result in heavily distorted elements. Lastly, further research is needed to assess the validity of the coupling in three dimensional simulations where different type of waves, such as longitudinal shear and Rayleigh waves interact simultaneously. In the next chapter these challenges will be tackled to formulate a three-dimensional dynamic concurrent adaptive framework.

Chapter 4

A novel dynamic adaptive concurrent multi-scale framework for 3D wave propagation in homogeneous media

In this chapter the previously described adaptive concurrent multi-scale framework is applied to 3D simulations. Particular attention is given to the methodology used for the generation of computational meshes during the computation and the definition of three-dimensional hermitian shape functions for the interpolation of kinematic quantities from different meshes. These contributions are implemented in a novel framework that, from a computational standpoint, privileges the possibility to include different refinement criteria as well as the efficient communication among different scales. The methodology is verified simulating elastic wave propagation in bars and validated against experimental results obtained on uniaxial tensile specimens involving strain localisation due to their inelastic deformation.

4.1 Uniform strain hexahedron element for explicit simulations

In the previous chapter a novel adaptive concurrent multi-scale framework has been introduced for the analysis of wave propagation in elastic media. In particular the general procedure is outlined in flowchart 3. In this chapter the full 3D form of

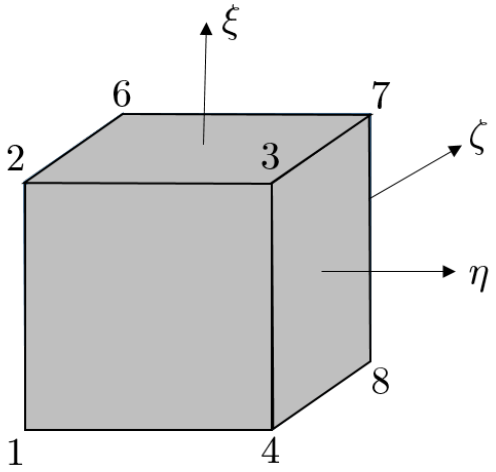

Figure 4.1: Configuration of hexahedron 8-nodes element in parent element domain.

Node Label	ξ	η	ζ
1	-1	-1	-1
2	1	-1	-1
3	1	1	-1
4	-1	1	-1
5	-1	-1	1
6	1	-1	1
7	1	1	1
8	-1	1	1

Table 4.1: Uniform strain Hexahedron node numbering and position

the proposed framework will be analysed and tested on hexahedral meshes.

The 8-node brick elements are widely used in explicit computational mechanics. When fully integrated they tend to present volumetric locking in which the displacements are unpredicted by large factors, therefore, a common solution for such behaviour is the use of selective integration in which the volumetric stress is integrated using a single quadrature point (reduced integration), while the deviatoric stress relies on full integration. However, the use of reduced integration for both deviatoric and volumetric stresses results in the appearance of zero energy spurious deformation modes, known as hourglassing. Flanagan and Belytschko [101] proposed an under-integrated hexahedron element in which the hourglassing is controlled by using an

artificial stiffness that opposes the zero energy modes. This element formulation, efficient and stable at the same time, will be used as well in this doctoral thesis.

The element configuration in the parent domain coordinate system is depicted in figure 4.1 and table 4.1. The element shape functions are represented by the product of linear shape functions in the directions ξ, η and ζ as reported in equation 4.1 in which ξ_i , η_i and ζ_i represent the coordinate of the node i in the parent element domain.

$$N_i = \frac{1}{8}(1 + \xi\xi_i)(1 + \eta\eta_i)(1 + \zeta\zeta_i). \tag{4.1}$$

In particular the equation 4.1 can be used to define a three dimensional interpolation, for the displacement field $\boldsymbol{u}(\boldsymbol{\xi}, t)$ as:

$$\boldsymbol{u}_{3x1} = \boldsymbol{N}_{3x24}\boldsymbol{u}^{\boldsymbol{e}}_{24x1}, \tag{4.2}$$

in which the dimensions of each matrix are reported as subscript *number of rows x number of columns*. The 24 rows of the right hand side of the equation 4.2, are given by the presence of 3 dimensions per every one of the 8 nodes of the hexahedron. Expanding the array $\boldsymbol{u}$ and $\boldsymbol{u}^{\boldsymbol{e}}$ along the three orthogonal directions as:

$$\begin{cases} \boldsymbol{u}_{3x1} = \begin{Bmatrix} p \\ q \\ r \end{Bmatrix}, \\ \boldsymbol{u}^{\boldsymbol{e}}_{24x1} = \begin{Bmatrix} \boldsymbol{p}^{\boldsymbol{e}}_{8x1} \\ \boldsymbol{q}^{\boldsymbol{e}}_{8x1} \\ \boldsymbol{r}^{\boldsymbol{e}}_{8x1} \end{Bmatrix}, \end{cases} \tag{4.3}$$

in which $\boldsymbol{p}^e$, $\boldsymbol{q}^e$ and $\boldsymbol{r}^e$ are column vector which store the nodal components of displacements along ξ, η and ζ, respectively. On the other hand p, q and r represent the interpolated values of the displacement in ξ, η and ζ. Equation 4.2 can be written in its expanded form as:

$$\begin{Bmatrix} p \\ q \\ r \end{Bmatrix} = \begin{bmatrix} \boldsymbol{\mathcal{N}}_{1x8} & \boldsymbol{0}_{1x8} & \boldsymbol{0}_{1x8} \\ \boldsymbol{0}_{1x8} & \boldsymbol{\mathcal{N}}_{1x8} & \boldsymbol{0}_{1x8} \\ \boldsymbol{0}_{1x8} & \boldsymbol{0}_{1x8} & \boldsymbol{\mathcal{N}}_{1x8} \end{bmatrix} \begin{Bmatrix} \boldsymbol{p}^{\boldsymbol{e}}_{8x1} \\ \boldsymbol{q}^{\boldsymbol{e}}_{8x1} \\ \boldsymbol{r}^{\boldsymbol{e}}_{8x1} \end{Bmatrix}. \tag{4.4}$$

In equation 4.4, $\mathbf{0}$ stands for a matrix with entries equal to 0, and $\boldsymbol{\mathcal{N}}$ is defined as:

$$\boldsymbol{\mathcal{N}} = \begin{Bmatrix} N_1 & \dots & N_i & \dots & N_8 \end{Bmatrix}, \tag{4.5}$$

in which the components N_i are defined in 4.1. This element presents several analogies with its 1D counterpart, however the refinement and error estimation procedures applied in the previous chapter are not directly applicable in a 3D context.

4.2 A local spatial error estimator based on 3D hermitian interpolation

Following the approach outlined in section 3.2.5 for linear 1D elements, a higher order hermitian interpolation is sought for the 3D hexahedron element. In particular, the equation 3.69 will be specialized for this element, both in terms of the matrix $\boldsymbol{H}(\boldsymbol{\xi})$ and $\boldsymbol{\Phi}(\boldsymbol{t})$. Following the approach of equation 4.4 an hermitian interpolation on an hexahedron can be defined as:

$$\begin{Bmatrix} p^* \\ q^* \\ r^* \end{Bmatrix} = \begin{bmatrix} \boldsymbol{\mathcal{H}}_{1x32} & \mathbf{0}_{1x32} & \mathbf{0}_{1x32} \\ \mathbf{0}_{1x32} & \boldsymbol{\mathcal{H}}_{1x32} & \mathbf{0}_{1x32} \\ \mathbf{0}_{1x32} & \mathbf{0}_{1x32} & \boldsymbol{\mathcal{H}}_{1x32} \end{bmatrix} \begin{Bmatrix} \boldsymbol{\Phi}^{\boldsymbol{p}}_{32x1} \\ \boldsymbol{\Phi}^{\boldsymbol{q}}_{32x1} \\ \boldsymbol{\Phi}^{\boldsymbol{r}}_{32x1} \end{Bmatrix}, \tag{4.6}$$

in which $\boldsymbol{\mathcal{H}}$ represents the hermitian interpolation matrix restricted to a single component $\boldsymbol{\Phi^p}$, $\boldsymbol{\Phi^q}$ and $\boldsymbol{\Phi^r}$ of the total vector of degrees of freedom $\boldsymbol{\Phi}$. Simultaneously, p^*, q^* and r^* represents the component of the interpolated hermitian displacement $\boldsymbol{u}^*$. Since the matrix $\boldsymbol{\mathcal{H}}$ is the same for every component, this section will focus on its definition. The analysis will be focus on a single component p of the nodal displacements, however the hermitian interpolation matrix $\boldsymbol{\mathcal{H}}(\boldsymbol{\xi})$ can be used for the other two components of the displacements in similar manner. Following the labelling defined in table 4.1 and the notation introduced in equation 4.1, for the hexahedron element depicted in 4.1 the vector $\boldsymbol{\Phi^p}(t)$ contains the nodal displacements and the derivatives of such displacement with respect to the parent spatial variables ξ, η and

ζ as a vector containing 32 entries as:

$$\boldsymbol{\Phi^p(t)} = \left\{ \begin{array}{c} \left(\begin{array}{c} p_1 \\ \vdots \\ p_8 \end{array} \right) \\ \hline \left(\begin{array}{c} \frac{dp_1}{d\xi} \\ \vdots \\ \frac{dp_8}{d\xi} \end{array} \right) \\ \hline \left(\begin{array}{c} \frac{dp_1}{d\eta} \\ \vdots \\ \frac{dp_8}{d\eta} \end{array} \right) \\ \hline \left(\begin{array}{c} \frac{dp_1}{d\zeta} \\ \vdots \\ \frac{dp_8}{d\zeta} \end{array} \right) \end{array} \right\}_{32x1} . \tag{4.7}$$

Using the equation 4.7 the equation 4.6 can be restricted to a single dimension as:

$$p^* = \boldsymbol{\mathcal{H}}_{1x32} \ \boldsymbol{\Phi^p}_{32x1}, \tag{4.8}$$

in which the spatial and time dependencies can be derived from 3.69.

The matrix $\boldsymbol{\mathcal{H}}$ can be expressed as the product of two matrices, one containing only the polynomial terms $\boldsymbol{G}$ expressed as $\xi^i\eta^j\zeta^k$ and a matrix of constant numerical coefficients $\boldsymbol{\mathcal{X}}$ leading to:

$$p^* = \boldsymbol{G}_{1x32}\boldsymbol{\mathcal{X}}_{32x32}\boldsymbol{\Phi^p}_{32x1}. \tag{4.9}$$

Therefore the hermitian interpolation will be fully defined defining the matrices $\boldsymbol{G}$ and $\boldsymbol{\mathcal{X}}$. Since the hermitian interpolation represents a third order polynomial in the spatial coordinates ξ, η and ζ the natural definition of the elements of $\boldsymbol{G}$ would be of all the terms that satisfy the condition:

$$G_{ijk} = \xi^i\eta^j\zeta^k \quad : \quad 0 \leq i, j, k \leq 3. \tag{4.10}$$

However the definition in 4.10 leads to a matrix $\boldsymbol{G}$ of dimensions 1x64, and therefore not adequate for the use in equation 4.9. An approach to define a suitable interpolation is to selectively reduce the order of coefficients used in equation 4.10 eliminating

higher order terms. This approach was proposed by Melkes and is known in the Finite Element Literature as the Adini-Clough element. Such approach has been proved efficient in 2D simulations, but this expansion has not been used in three dimensions. Melkes has proved that for every dimension d a *reduced* form of the polynomial 4.10 is characterized by terms having a degree less or equal than 3 in each dimension and degree larger than one in no more than one dimension. Such conditions lead to:

$$G_{ijk} = \xi^i \eta^j \zeta^k \quad : \quad 0 \leq i, j, k \leq 3 \quad \cup \quad i + j + k \leq 5. \tag{4.11}$$

With equation 4.11 at hand it is possible to define the array matrix $\boldsymbol{G}$ as:

$$\boldsymbol{G} = \left\{ G_{000} \quad \dots \quad G_{113} \right\}_{1x32}. \tag{4.12}$$

To completely define the matrix $\boldsymbol{\mathcal{H}}$, the numerical coefficients of $\boldsymbol{\mathcal{X}}$ must be determined. Such coefficients can be determined imposing the delta Kronecker condition at nodal positions, meaning that the hermitian shape functions should evaluate to one at nodal positions and zero elsewhere [12]. Such conditions lead to:

$$p^* = p_i = \boldsymbol{G}(\xi_i, \eta_i, \zeta_i) \boldsymbol{\mathcal{X}} \boldsymbol{\Phi^p} \quad i = \left\{ 1 \dots 8 \right\}, \tag{4.13}$$

in which the index i scrolls the eight nodes of the hexahedron. Imposing this condition to be valid for a generic $\boldsymbol{\Phi^p}$, equation 4.13 can be written as:

$$\boldsymbol{G}(\xi_i, \eta_i, \zeta_i) \boldsymbol{\mathcal{X}} = \boldsymbol{U^k} \quad i = k = \left\{ 1 \dots 8 \right\}, \tag{4.14}$$

in which $\boldsymbol{U^k}$ represents an array of 32 entries, which is zero everywhere but at position k, where it assumes a value of 1. For example for the node 1 equation, taking in consideration the table 4.1, the equation 4.14 can be expressed as:

$$\left\{ -1 \ \dots \ -1 \right\}_{1x32} \begin{bmatrix} \boldsymbol{\mathcal{X}}_{1\,1} & \dots & \boldsymbol{\mathcal{X}}_{1\,32} \\ \vdots & \ddots & \vdots \\ \boldsymbol{\mathcal{X}}_{32\,1} & \dots & \boldsymbol{\mathcal{X}}_{32\,32} \end{bmatrix}_{32x32} = \left\{ 1, \quad 0 \quad \dots \quad 0 \right\}_{1x32}. \tag{4.15}$$

Repeating the same procedure for the other seven nodes, it is possible to obtain a system of $8x32 = 256$ equations in $32x32 = 1024$ unknowns.

The remaining conditions can be found, imposing the delta Kronecker condition on the derivative of the displacement with respect to the three spatial directions to match the nodal values. These conditions can be expressed as:

$$\begin{cases} \dfrac{dp^*}{d\xi} = \dfrac{dp_i}{d\xi} = \dfrac{\boldsymbol{dG}}{d\xi}\boldsymbol{\mathcal{X}} = \boldsymbol{U^k} & i = \left\{1 \dots 8\right\} \quad k = \left\{9 \dots 16\right\}, \\ \dfrac{dp^*}{d\eta} = \dfrac{dp_i}{d\eta} = \dfrac{\boldsymbol{dG}}{d\eta}\boldsymbol{\mathcal{X}} = \boldsymbol{U^k} & i = \left\{1 \dots 8\right\} \quad k = \left\{17 \dots 25\right\}, \\ \dfrac{dp^*}{d\zeta} = \dfrac{dp_i}{d\zeta} = \dfrac{\boldsymbol{dG}}{d\zeta}\boldsymbol{\mathcal{X}} = \boldsymbol{U^k} & i = \left\{1 \dots 8\right\} \quad k = \left\{26 \dots 32\right\}, \end{cases} \tag{4.16}$$

in which the array $\boldsymbol{G}$ is differentiated with respect to the variables ξ, η and ζ using the expressions from equation 4.10. Similarly to the equation 4.14, each one of the equations in 4.16 lead to 8x32 conditions. Therefore the union of the conditions expressed in 4.14 and 4.10, leads to a system of 1024 equations in 1024 unknowns. The actual resolution of this system of linear equation is reported in Appendix A, using the software MATLAB. Once $\boldsymbol{\mathcal{X}}$ has been determined, $\boldsymbol{\mathcal{H}}$ can be computed as the product of $\boldsymbol{GX}$. Finally, the matrix $\boldsymbol{H}$, which defines the hermitian interpolation is assembled using the equation 4.6.

Once the matrix $\boldsymbol{H}$ has been determined the degrees of freedom in $\boldsymbol{\Phi}$ need to be evaluated. Since the operations are equivalent for each direction the array $\boldsymbol{\Phi^p}$ will be defined. The first 8 components of such array represent the standard degrees of freedom of the Standard under-integrated hexahedron $\boldsymbol{p^e}$. To determine the derivative terms the approach used in section 3.2.5 will be extended to the 3 dimensions space. As an example consider the 8 elements of figure 4.2, the aim is to determine the approximation for $\dfrac{dp}{d\xi}, \dfrac{dp}{d\eta}$ and $\dfrac{dp}{d\zeta}$ for the central node of the assembly, defined as the query node and labelled as I. The node I can be isolated from the assembly together with its neighbour nodes labelled from II to VII, and using a central difference approximation the derivatives of the displacement p_I, with respect to the parent

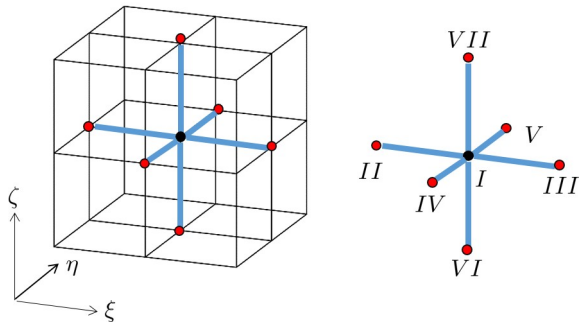

Figure 4.2: Derivation of the approximation of the derivative terms in the vector $\mathbf{\Phi}$ for the node I. Employing a central difference scheme, an approximation for such terms can be computed only considering the neighbouring nodes.

domain coordinates can be approximated as:

$$\begin{cases} \dfrac{\partial p_I}{\partial \xi} = \dfrac{p_{III} - p_{II}}{4}, \\ \dfrac{\partial p_I}{\partial \eta} = \dfrac{p_V - p_{IV}}{4}, \\ \dfrac{\partial p_I}{\partial \zeta} = \dfrac{p_{VII} - p_{VI}}{4}, \end{cases} \tag{4.17}$$

in which is recalled that the length of an edge in the parent element domain is equal to 2. In case of nodes on an external facet of the computational domain the same procedure can be adopted employing a backward or forward approximation formula. Once the derivatives at the nodal point are computed using 4.17, the array $\mathbf{\Phi}$ can be assembled and the hermitian interpolation of the displacement field computed.

4.3 An efficient refinement algorithm for 3D hexahedral meshes

The rate of error for elastic problems using hermitian interpolation has been discussed in section 3.3.2. Such rate is used for the evaluation of the refinement factor for the new finer mesh. In one dimension the refinement procedure is trivial, since two adjacent elements only share the original node. However this is not the case for 3D hexahedral meshes where two adjacent elements share newly generated nodes along edges and faces as depicted in figure 4.3. Moreover, in traditional refinement schemes the refined mesh is required to respect the conformity condition, meaning that two

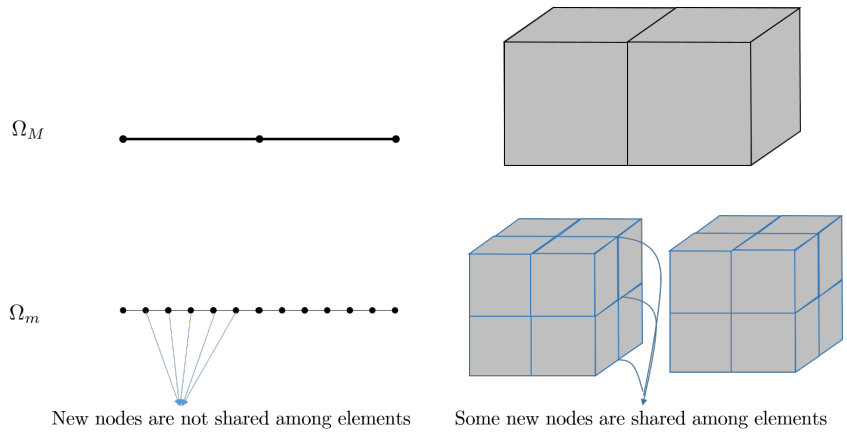

Figure 4.3: The refinement procedure for 3D elements generates shared nodes between the original elements. This condition does not arise in 1D mesh.

or more elements at the interface between the coarse and fine mesh, share a face a edge or a point as shown in picture 4.3.

Two different methods have been proposed in the literature to create meshes that respect such condition. In [11, 102], a octree-based refinement scheme is proposed, and depending on the position of element on the refinement level different transition elements are created between the coarse and fine scale mesh as shown in picture 4.4. The placing of the transition elements plays a crucial role in the generation of conformal meshes. On the other hand, Belytschko [103] and recently Bui et al. [104] proposed a method that does not use transition elements. The non conformal node degrees of freedom are forced to follow the displacement of the master original nodes. Both of these methods do not address the spurious wave generation and propagation at the interface between the newly created domains. In this work, the new mesh is generated during the computation according to the refinement factor assigned from the coarse scale computation without the use of transition elements. The coupling between the two non conformal meshes is obtained using the explicit formulation of the coupling forces described in section 3.2.

The refinement technique proposed in this work is based on an isotropic refinement in the parent element domain in the three orthogonal directions ξ, η and ζ. Once

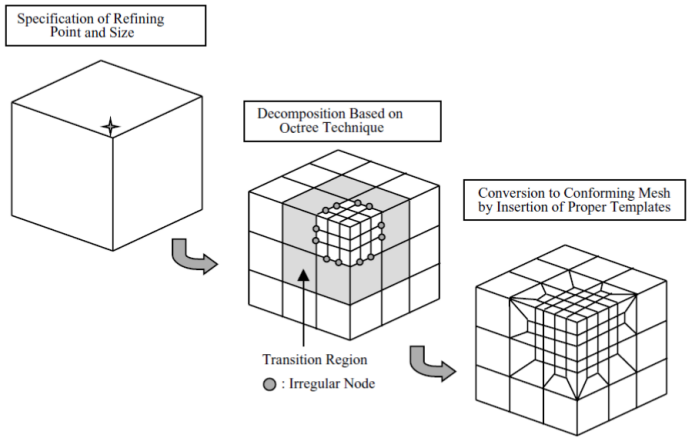

Figure 4.4: Refinement procedure proposed in [11] where different element templates are used to generate a conforming mesh.

the element has been refined in its parent domain, the position of the new nodes in the physical domain is mapped using the standard shape functions. Such technique avoids the creation of distorted elements at the finer scale as shown in figure 4.5. The computational efficiency of the algorithm, resides in the avoidance of merging and searches for repeated nodes at shared faces or edges between two or more elements. Such process is avoided by implementing two new entities for the faces and edges of the flagged elements. Every element will inherit or create new nodes over a face or an edge depending on whether or not such entities have been previously refined by a neighbouring element. The complete refinement algorithm is reported in flowchart 4.

Flowchart 4. *Flowchart for refinement of flagged elements*

1. *Loop over elements to refine*
2. *Create nodes in parent element domain according to refinement factor*
3. *Map new nodes on deformed configuration*
4. *If any face or edge of the selected element has been refined by another element, inherit labels*
5. *Create connectivity matrices for the fine scale elements*
6. *Go to 1*

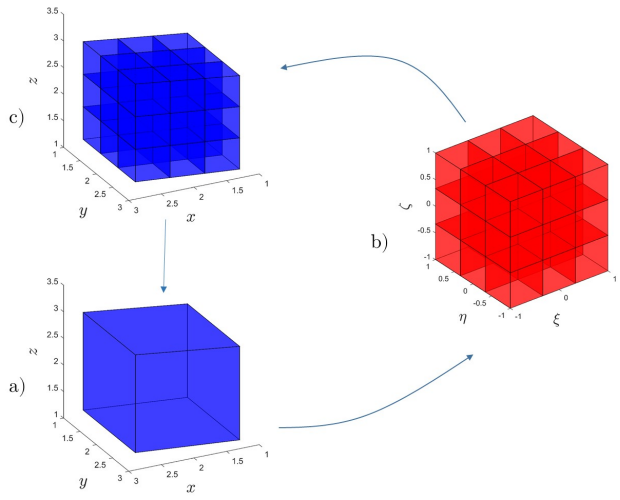

Figure 4.5: Schematic representation of the refinement algorithm proposed. The flagged elements (a) are firstly refined in their parent element domain (b), and then mapped on the deformed configuration (c)

4.4 A novel 3D framework for dynamic adaptive concurrent multi-scale simulations

In the previous sections the error estimation, mesh refinement, data transfer and communication among the different scales has been completely described in the three dimensional space. However, the efficiency of the dynamic adaptive concurrent multi-scale methodology depends heavily on its implementation, as described in this section.

On the one hand the novel framework has to guarantee excellent performances in terms of computational efficiency while on the other hand it has to be general enough to fulfil both the aim and objectives of the present research.

The fundamental block upon which such framework is built is the mono-scale explicit formulation of finite elements described in flowchart 1 in which the solution of a single length and time scale Ω^M is propagated in each time-step until a certain user defined end time is reached. The time integration over a single time-step is condensed in one block in figure 4.7 as $t^M \rightarrow t^{M+1}$. Once the simulation has advanced over a single time-step, the quality of the solution can be assessed through different algorithms such as error estimation or strain/stress localisation. Even if different, the criteria to highlight an element for refinement make use of the propagated solution

and the current configuration, therefore to guarantee the versatility of the framework this procedure is executed after one time increment.

If the different refinement criteria implemented highlight different portions of the the coarse domain Ω^M, different micro-scales Ω^{m^1} ... Ω^{m^n} will be generated. As an example in figure 4.6, Ω^M generates two micro-scales Ω^{m^1} and Ω^{m^2}. The refined meshes together with the assigned time-step, their data and the nodal weights constitute a *scale*. In terms of hierarchy Ω^M is thought as a parent for its child micro-scales. The communication between the scales allows one child domain to exchange information, over the coupling volume, only with its parent. Therefore the weighting parameter, will blend the energies between one child/finer domain and its parent as shown in flowchart 4.7. Every child micro-scale, after one increment with their own time-step, will enforce the velocity compatibility condition in equation 3.52, using as macro velocities the ones of their parent domain Ω_M. Once the finer scales reach the same time as their parent, the coupling term of equation 3.31 is applied on the parent domain on the different coupling volumes, allowing a two way communication. In the simplest configuration a coarse domain generates one or more fine-scales, however the general situation is that every domain at each scale can generate different child entities, using always the same communication scheme. As an example in flowchart 4.7 and figure 4.6 the domain Ω^{m^2} generates Ω^{m^3}, over which the same communication implemented above is established.

The proposed framework and hierarchy can couple different scales and discretisation schemes, resulting versatile, and easy to maintain. In this thesis, the coupling between one macro and one micro scale both discretised with the explicit formulation of the finite elements will be studied. This coupling will allow a better understanding of the stability properties and performances of the overall scheme.

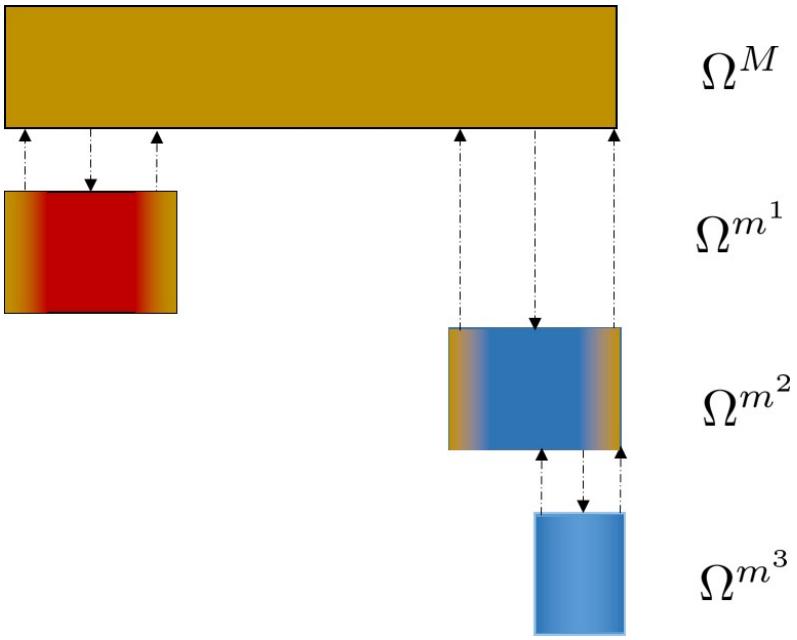

Figure 4.6: Representation for the proposed adaptive concurrent multi-scale framework. The coarse scale Ω^M generates two micro-scales Ω^{m^1} and Ω^{m^2} that communicate only with their parent domain (the communication is represented by the dashed arrows). The child/fine scales can recursively generate finer domains, in this case Ω^{m^2} is the parent of Ω^{m^3}, which employ the same communication scheme.

4.5 Applications

In this section different applications are examined using the proposed adaptive multi-level scheme in space and time. Particular attention is given at the results in terms of stability and generation of numerical artefacts at the interface between the differently discretised domains.

4.5.1 Square bar without lateral inertia

The first application is the direct 3D transformation of the problem examined in section 3.3.1. In this case the square bar is analysed ith a sequence of hexahedrons. The geometrical features of the bar and mesh are reported in table 4.2 and figure 4.8. The coarse scale is represented by elements of height $h = \frac{L}{50}$ and width $w = D$, thus one single element over the cross section is included. The bar is impacted from one side, and the contact is modelled as a half sinusoidal velocity boundary condition. The absence of the Poisson's ratio eliminates every lateral inertia effect, making it

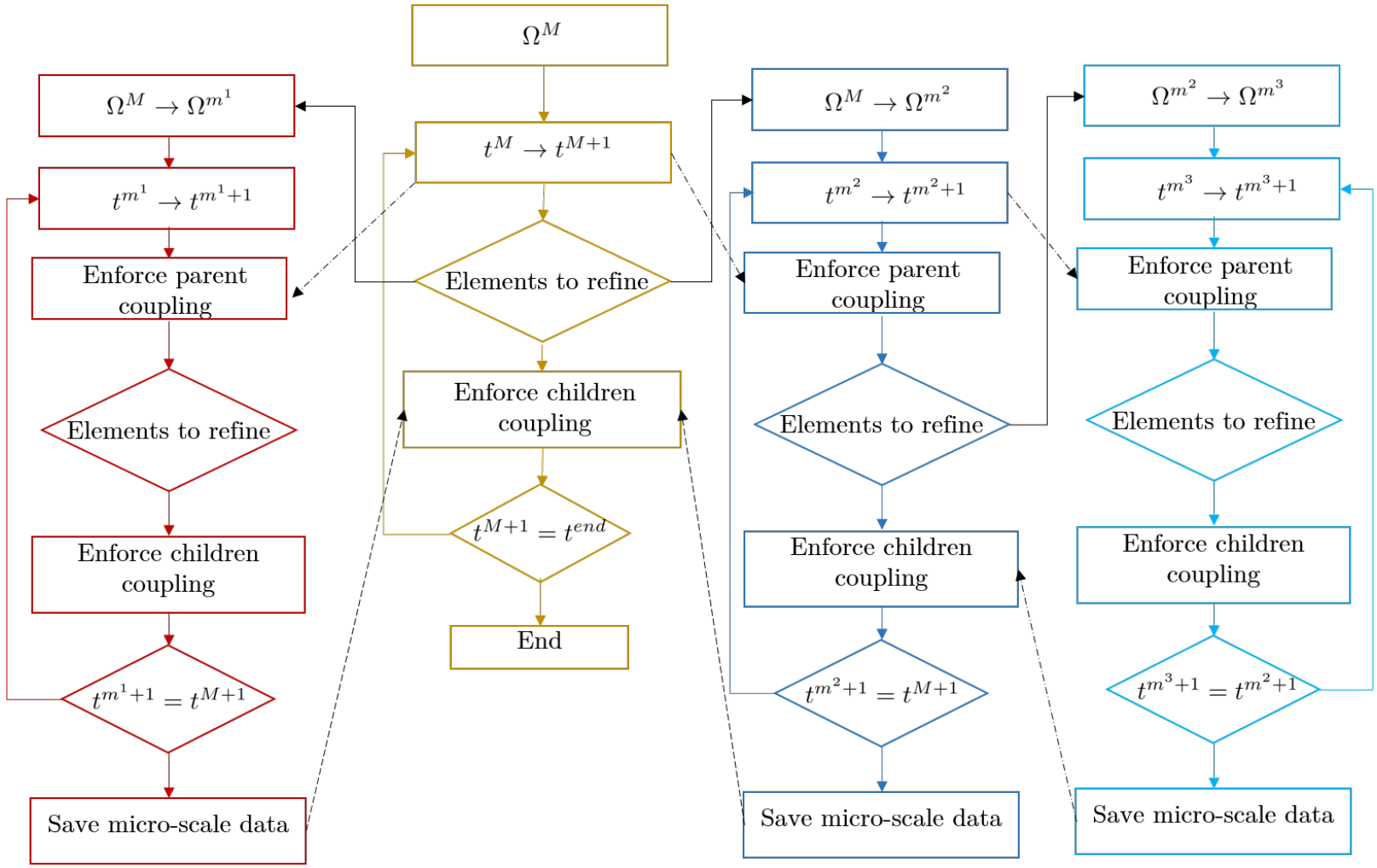

Figure 4.7: Flowchart for the proposed adaptive concurrent multi-scale framework. The coarse scale Ω^M generates two micro-scales Ω^{m^1} and Ω^{m^2} that communicate only with their parent domain (the communication is represented by the dashed arrows). The child/fine scales can recursively generate finer domains, in this case Ω^{m^2} is the parent of Ω^{m^3}, which employ the same communication scheme.

E	$210\,GPa$
ρ	$7.85e*10^{-6}\,\frac{kg}{mm^3}$
L	$500\,mm$
D	$80\,mm$

Table 4.2: Material and geometry used for the simulation of the square bar.

possible to assess the good implementation of the framework in a 3D setting. The fine scale is generated prescribing an error threshold which translates to a refinement factor of 5.

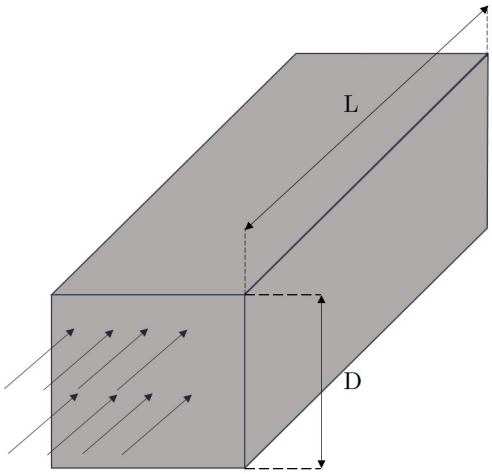

Figure 4.8: Geometry of the square cross sectional bar.

Figure 4.9 shows a qualitative comparison among the multi-scale and macro-scale simulation at different time-steps. At every macro-time steps, the error criterion flags almost all the elements affected by the wave which present an error higher that the user input threshold, and their neighbours for coupling purposes. In the left side of the figure the wave is represented over the computational domain at a certain macro time-step. These elements, and their neighbours are refined in the micro-scale simulation. The coupling between the micro and the macro-scale computational meshes is achieved using the already defined blending parameter α over the coupling elements as shown in picture 4.10. Such weights are linearly distributed over the coupling length, selected as one element of the coarse scale mesh. The distribution of the

weights over the micro-scale domain is shown in the upper part of picture 4.10. The quantitative comparison of the results in terms of longitudinal stresses and longitudinal velocities for the coarse solution and the fine multi-scale solution are compared in figure 4.11,4.12,4.13 and 4.14. The results of the multi-scale simulation show less numerical dispersion, present in the mono-scale simulation in form of oscillations behind the main pulse. The presence of the coupling parameter blends the frequencies close to the coupling zone annihilating the presence of spurious oscillations due the abrupt change in mesh resolution. At a global level, the solution of the multi-scale simulation results are stable as shown in picture 4.15 and 4.16, where the kinetic and elastic energies are compared in case of multi and mono-scale simulations. It is also important to highlight that the total energy of the system (after the pulse has been totally transmitted into the bar at t = $0.04ms$) is constant along the simulation, even during the rebound of the compression wave at the free end of the bar (t = $0.15ms$), and therefore, the non-dissipative implementation of the coupling is verified again through this validation case.

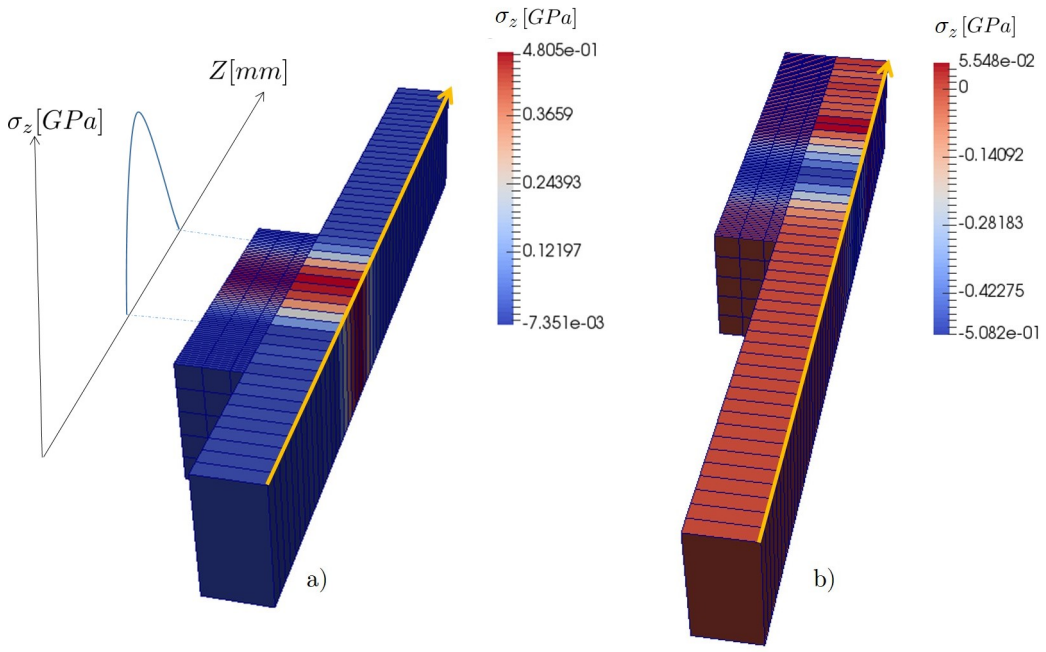

Figure 4.9: Case of square bar without lateral inertia. Comparison between the mono-scale and multi-scale spatial distribution of σ_z at $t = 0.0789$ ms a) and $t = 0.1407$ b). The yellow line represents the axis over which the velocities will be plotted. On the lateral plane the analytical solution for this problem, at the same time, is depicted. The micro-scale simulation is activated for the entire portion of the domain that is interested by the wave. Its extension is dictated by the macro-scale elements that present a high error together with their neighbours.

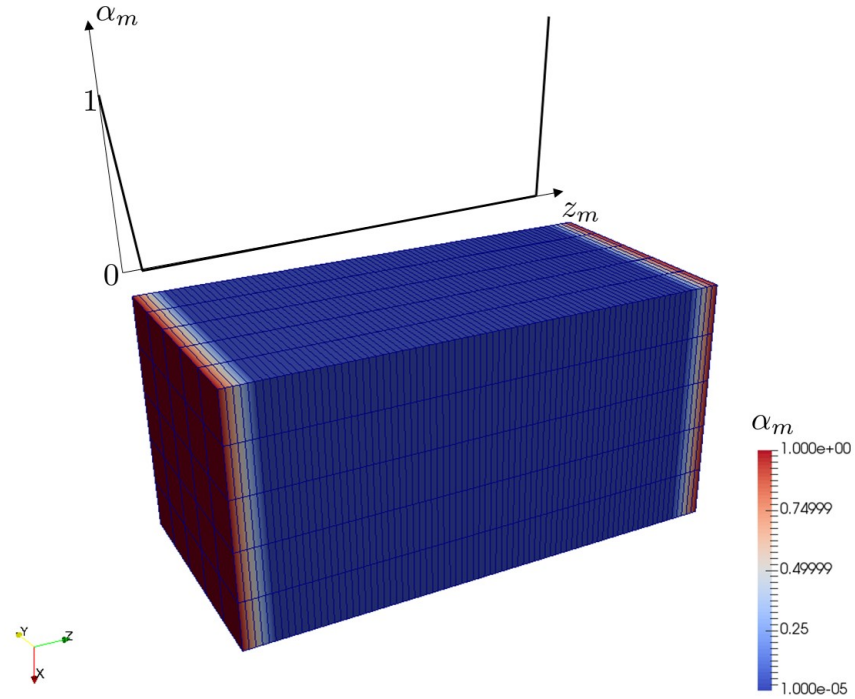

Figure 4.10: Configuration of the coupling parameter α for the refined mesh at $t = 0.0789$ ms. The coupling parameter varies linearly over the length of one macro-scale element.

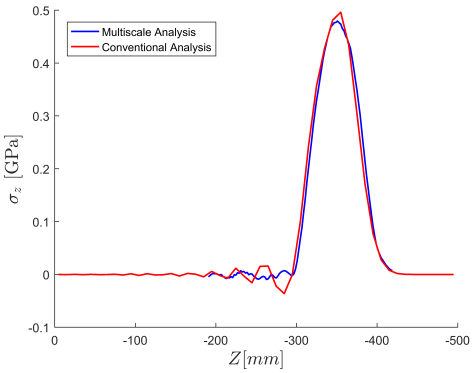

Figure 4.11: Case of square bar without lateral inertia. Comparison of stresses for conventional and multi-scale simulation at t = 0.0789 ms

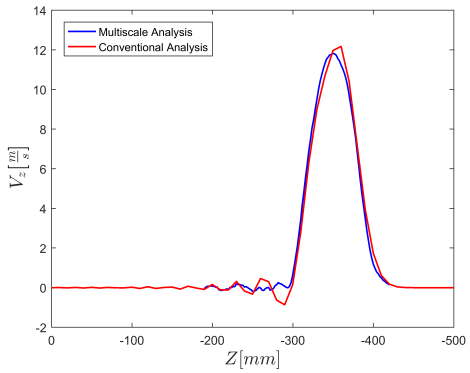

Figure 4.12: Case of square bar without lateral inertia. Comparison of velocities for conventional and multi-scale simulation at t = 0.0789 ms

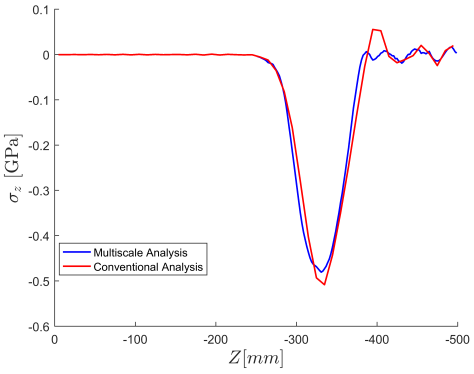

Figure 4.13: Case of square bar without lateral inertia. Comparison of stresses for conventional and multi-scale simulation at t = 0.1407 ms.

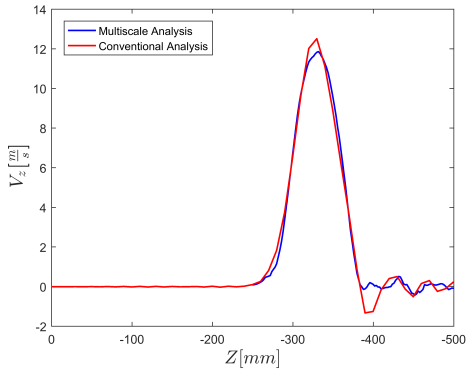

Figure 4.14: Case of square bar without lateral inertia. Comparison of velocities for conventional and multi-scale simulation at t = 0.1407 ms.

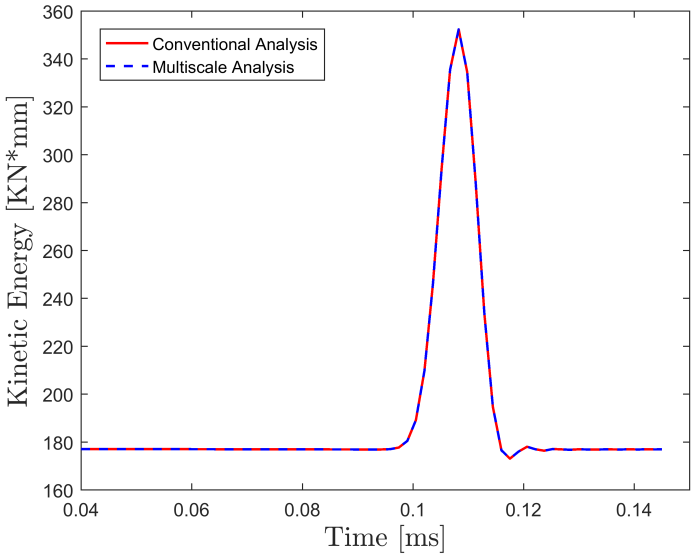

Figure 4.15: Case of square bar without lateral inertia. Comparison between the kinetic energy for both the mono-scale and multi-scale simulations. The two curves show very similar trends meaning that the energy is globally the same.

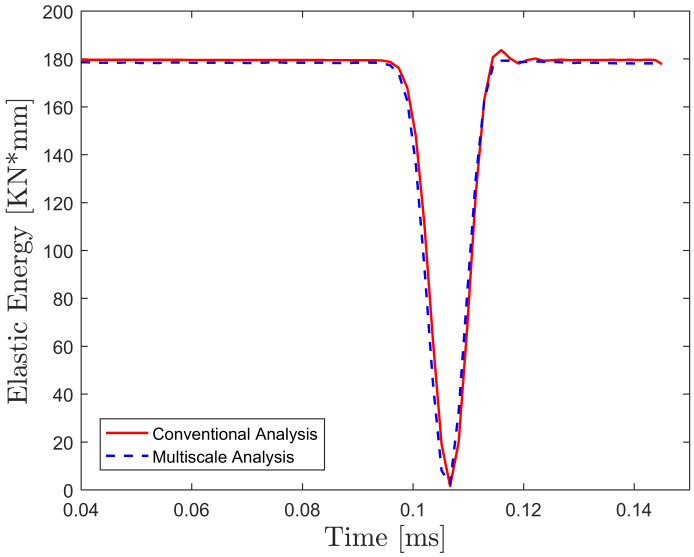

Figure 4.16: Case of square bar without lateral inertia. Comparison between the elastic energy for both the mono-scale and multi-scale simulations. The two curves show very similar trends meaning that the energy is globally the same.

4.5.2 Lateral Inertia Effect in thick square bar

The absence of Poisson's ratio in the previous loading case did not allow the formation and propagation of lateral inertia effects. Stress propagation in real bars always presents a component of lateral inertia that creates a physical wave dispersion. Such dispersive effect invalidate the planar and one dimensional propagation hypothesis, and they are more significant as the ratio between radius of the bar and the length of the loading pulse Λ_c is bigger than 0.2 [105]. In this section it will be proved that the proposed refinement scheme, together with the coupling, filters only the non-physical spurious wave reflection while retaining the physical dispersion due the lateral inertia effects.

The geometrical features of the bar are reported in table 4.2. Differently from the previous case a Poisson's ratio of $\nu = 0.33$ is included in the material properties. The coarse scale is represented by elements of height $h = \frac{L}{50}$ and width $w = \frac{D}{4}$, thus four elements over the cross section are included. The bar is impacted from one side, and the contact is modelled as a quarter sinusoidal velocity boundary condition of amplitude $A = 12\frac{m}{s}$ and period $T = 0.08ms$, while the opposite face is longitudinally constrained. The geometrical and loading condition lead to a ratio between radius of the bar and length of the loading pulse $\frac{r}{\Lambda_c} \approx 0.4$.

Since an analytical solution is not available for this simulation the mono-scale coarse simulation will be compared against a finer mesh where the elements presents height $h = \frac{L}{350}$ and width $w = \frac{D}{28}$, corresponding to a refinement factor of the coarse scale of 7. Figure 4.17 and 4.18 compare the velocities against the two simulations in terms of longitudinal velocities along the central axis of bar at two different times, namely before and after the rebound. Because of the symmetrical properties of the bar there are no significant lateral velocities along the central axis, but they are visualised in the contour plot of figure 4.19 at $t = 0.05ms$. The coarse scale is not able to represent well the lateral motion of the bar, because of its poor discretisation in the cross section.

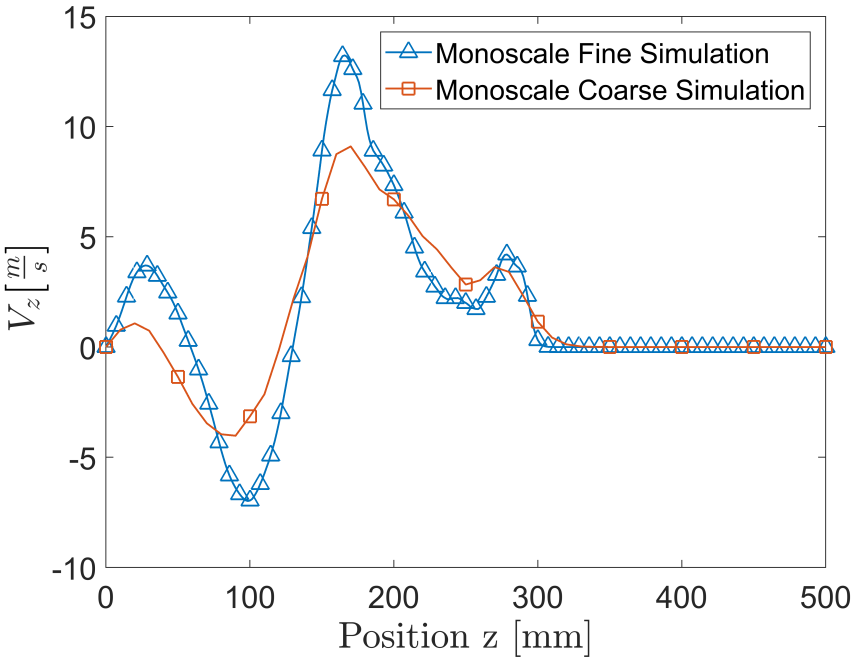

Figure 4.17: Comparison among the mono-scale fine simulation, and the coarse simulation at t = 0.05 ms. The coarse scale can not capture the magnitude of the particle velocity along the bar

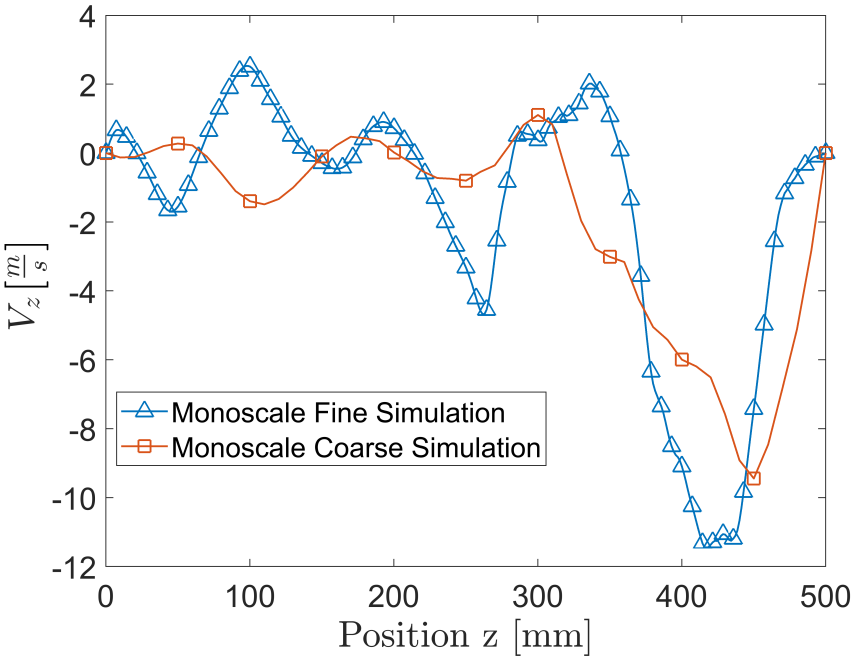

Figure 4.18: Comparison among the mono-scale fine simulation, and the coarse simulation at t = 0.125 ms. After the wave rebound the coarse scale can not track the particle velocity along the bar.

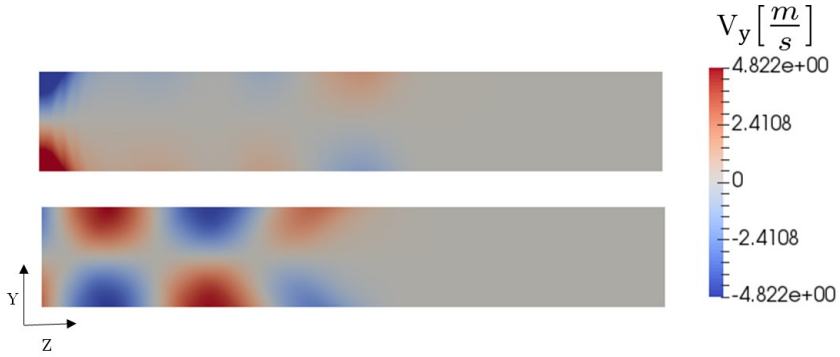

Figure 4.19: Contour plot of lateral velocity for coarse (top) and fine (bottom) simulation at t = 0.05 ms. The macro-scale simulation cannot capture the lateral motion of the bar.

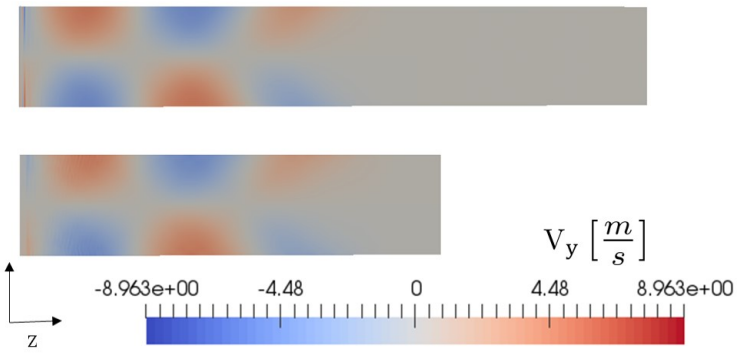

Figure 4.20: Contour plot of lateral velocity for fine mono-scale (top) and multi-scale (bottom) simulation at t = 0.05 ms. The two simulations show similar results.

4.3. The coarse scale mesh is used as basis for a multi-scale simulation, where the pre-defined error tolerance requires a refinement factor of 7 such that the lateral motion of the bar will be well represented. The multi-scale and the fine mono-scale simulation are compared in terms of longitudinal velocities along the central axis of the bar at $t = 0.05\ ms$ in figure 4.21 and $t = 0.125\ ms$ in figure 4.22 showing a perfect correlation among them, validating the results predicted by the multi-scale simulation. For further verification, figure 4.20 compares the lateral velocities obtained again from the fine mono-scale and the multi-scale simulation, presenting perfect agreement. Therefore, the proposed coupling among the different scales is able to represent the structural behaviour of the structure, without creating numerical artefacts. Differently from the previous testing case in section 4.5.1, the error in the coarse scale is

Coarse mono-scale simulation	1
Multi-scale simulation	52.75
Fine mono-scale simulation	90.25

Table 4.3: Comparison of the computational time for the simulation of the square bar, including lateral inertia effects. Even if the refined domain grows at every time-step until it encloses the whole computational domain, the computational time is still lower than the one for mono-scale fine simulation.

not distributed over a limited portion of the computational domain, instead all the elements that are behind the wave front are highlighted for refinement. In particular, the figure 4.20 is a snapshot of the coarse and fine scale domains at $t = 0.05ms$. Taking in consideration the longitudinal velocity of sound in the material expressed as $c = \sqrt{\dfrac{E(1-\nu)}{\rho(1+\nu)(1-2\nu)}} = 6295m/s$, the wave front will be at $z = ct = 314mm$ in the Z direction, which explains why more than half of the total coarse scale domain of $500mm$ is refined at a finer scale. The growing nature of the multi-scale simulation affects its computational time, nevertheless is still 60% smaller when compared to the mono-scale fine simulation. The three computational times are compared in table The previous simulations presented an absence of numerical spurious oscillations due to the weighting parameter function α applied over a coupling volume, always selected as one macro-scale element. However, the behaviour of the weighting function, even if prescribed a priori, can be modified. For the case under examination, three different weighting functions are compared. Using the same notation of the 1D validation case depicted in figure 3.6, defining the characteristic length of Ω_C as ℓ_c and ξ_c as the direction that points from Ω_m to Ω_M the three proposed couplings are

$$\begin{cases} \alpha_m^L & = \frac{\xi_c}{\ell_c} \\ \alpha_m^C & = 1 \\ \alpha_m^P & = \left(\frac{\xi_c}{\ell_c}\right)^4 \end{cases} \tag{4.18}$$

in which α_m^L represents the a linear weighting function (used for all the simulations) over ξ_c, α_m^C represents a constant function and α_m^P a power law function with exponent 4. The three proposed functions are represented in figure 4.23.

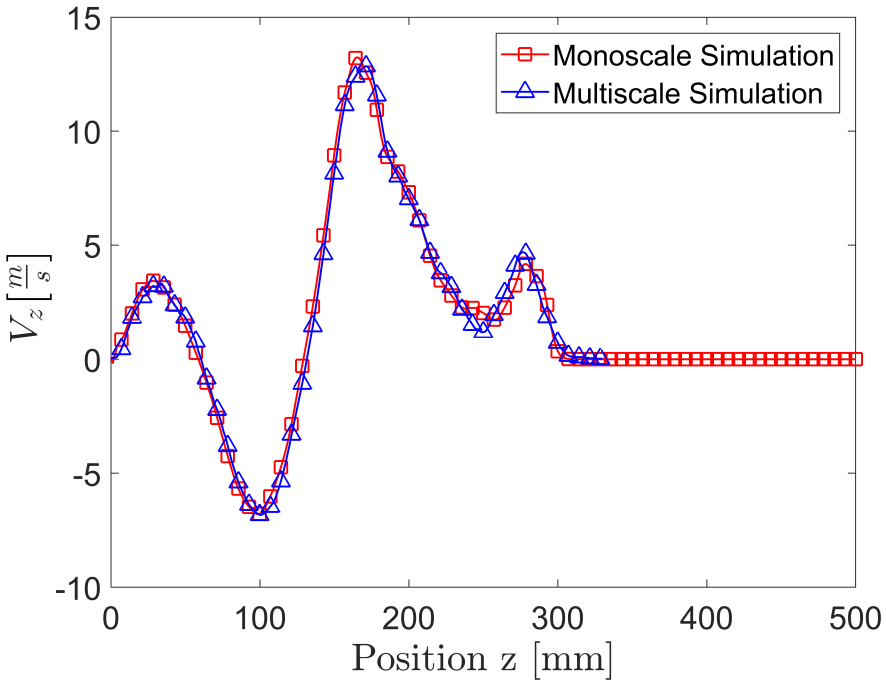

Figure 4.21: Comparison among the multi-scale simulation and the mono-scale fine simulation at t = 0.05 ms. The elements flagged for refinement are the ones behind the wave front.

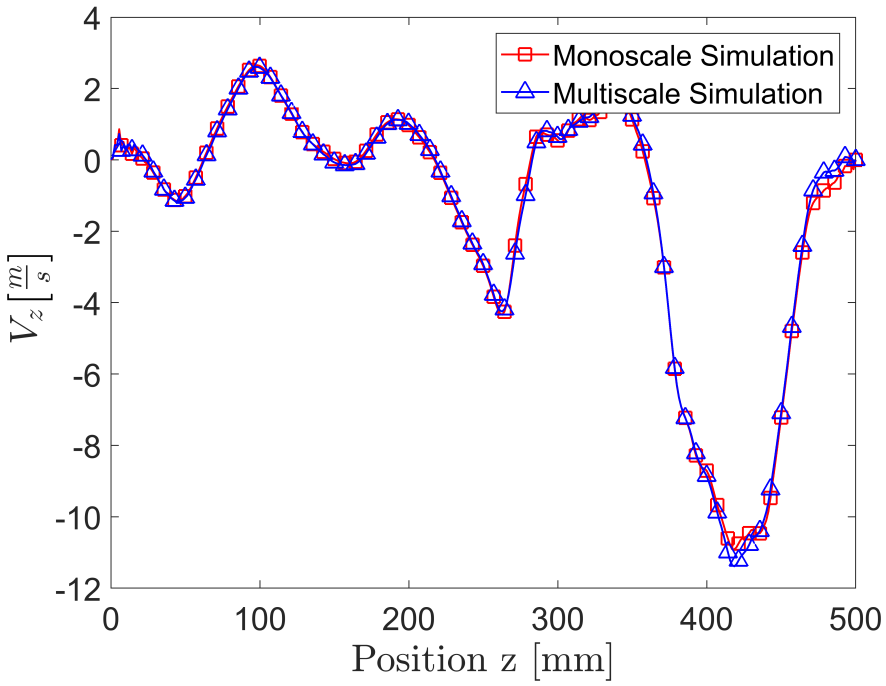

Figure 4.22: Comparison among the multi-scale simulation and the mono-scale fine simulation at t = 0.125 ms (after the reflection). At this time-step the whole bar has been flagged for refinement.

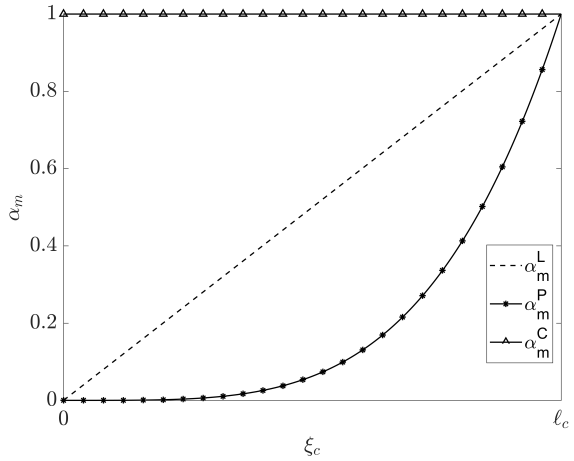

Figure 4.23: Plot of the proposed weights for the parametric study of the weighting function α_m.

Figure 4.24 and 4.25 compare the three different couplings in terms of longitudinal velocities along the bar at $t = 0.05\ ms$. In figure 4.24 the solution of the linear coupling and constant coupling are compared. When using α_m^C even if the simulation still results stable, a spurious wave propagates in the computational domain generating an artificial high frequency oscillations of the solution. Figure 4.25 compares the use of α_m^L and α_m^P from which it is evident that there is not a substantial difference between the two simulations.

This parametric study shows that the effect of the blending function α_m is fundamental for the correct coupling of the two domains and proves that the selection of the weighting parameters is not trivial, as it can result in spurious wave reflection. Considering the parametric studies carried out in this research, a suggestion for a general form of a correct coupling can be expressed as

$$\alpha_m = \left(\frac{\xi_c}{\ell_c}\right)^{\gamma} \quad 0 < \gamma \leq 4 \tag{4.19}$$

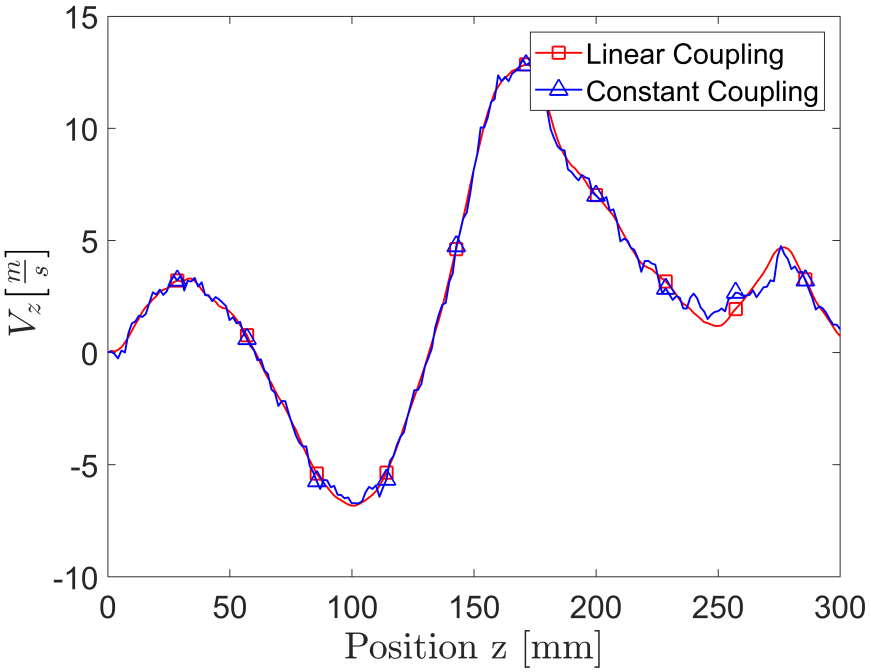

Figure 4.24: Comparison among the multi-scale simulations for two different weighting parameters, namely α_m^C and α_m^L at t = 0.05 ms. The constant coupling shows a significant amount of spurious wave reflections.

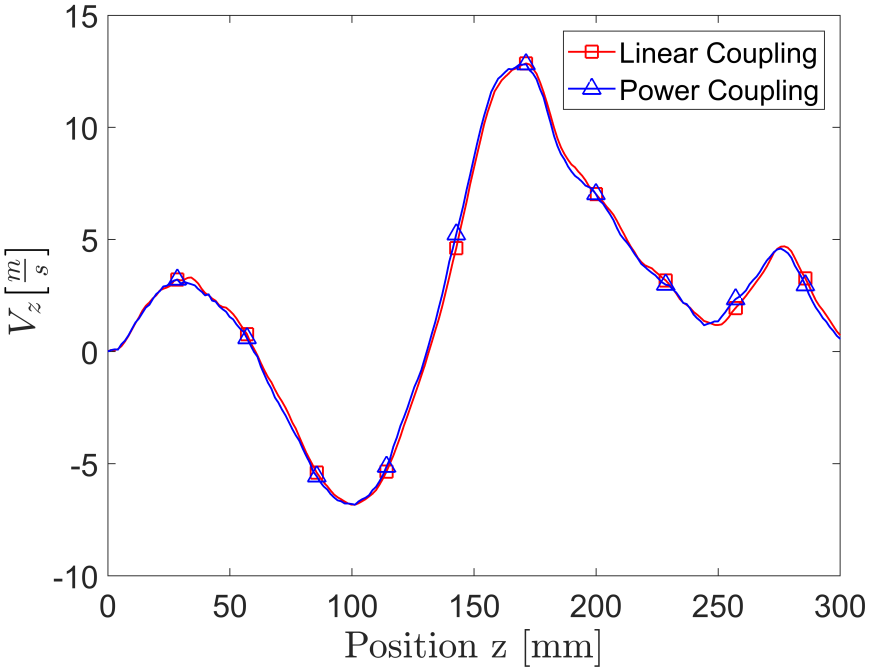

Figure 4.25: Comparison among the multi-scale simulations for two different weighting parameters, namely α_m^L and α_m^P at t = 0.05 ms. The two couplings show very similar performances without the generation of spurious waves.

4.5.3 Slender Circular bar

As it was mentioned in previous section, stress propagation in real bars always presents a component of lateral inertia that creates a physical wave dispersion. Such dispersive effect invalidate the planar and one dimensional propagation hypothesis, however in some cases such dispersion is negligible and 1D theories are still valid. In particular, lateral inertia components are negligible, when the ratio between the diameter of the bar D and the total length of the loading pulse Λ represented in figure 2.1 is smaller then 0.2 [105]. Therefore the simulation of planar waves using a standard explicit finite element formulation can result in a wrong estimation of the stresses and velocities in the bar when using coarse computational meshes.

E	$210\,GPa$
ρ	$7.85e*10^{-6}\,\frac{kg}{mm^3}$
ν	0.33
L	$500\,mm$
D	$10\,mm$

Table 4.4: Material and geometry used for the simulation of the slender circular bar.

As an example consider a circular steel bar whose geometrical and material properties are reported in table 4.4. The bar is hit on side and the contact is modelled with a quarter sinusoidal wave of period $T = 0.06\,ms$ and amplitude $A = 12\,\frac{m}{s}$, while the bar is supported on the other side. It is possible to verify that this configuration respects the hypothesis of planar wave propagation. The mesh along the cross section of the bar is depicted in figure 4.26. Two parameters are used to define the mesh, namely the number of divisions along one edge of the internal square n_{sq} and the number of divisions along the diagonal n_{diag}. Subsequently the 2D mesh is extruded along the direction orthogonal to the plane according to a parameter n_{thick} obtaining a hexahedral mesh for the whole computational domain.

Fig 4.27 compares the solution of the coarsest and the finest computational meshes in terms of longitudinal stress along the central axis of bar, with increasing number

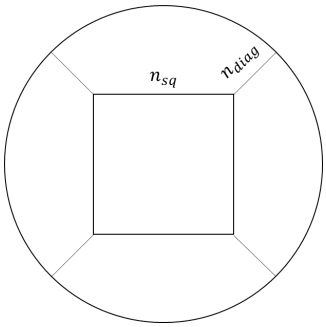

Figure 4.26: Geometrical divisions for a section of a square circular bar. The cross section mesh is defined by the number of divisions in the square n_{sq} and the number of divisions on the diagonal n_{diag}.

of elements at $t = 0.05ms$. Increasing the elements in both the cross section and along the bar axis, improves the quality solution. The recovered error for these simulations, reported in table 4.5, shows a decreasing trend whose rate is similar to the 1D constant strain element. However, as expected, the computational time increases when decreasing the mesh size.

n_{sq} x n_{diag} x n_{thick}	Computational time	Recovered Error * $[kN * mm]$
5x2x25	1	0.02867
5x2x50	2	0.01703
15x6x100	10.5	0.003186
15x6x150	55	0.002386
20x24x200	200	0.001529

Table 4.5: Study on the computational time and error trends varying the mesh size for wave propagation in a slender circular bar.* The recovered error is computed at time $t = 0.05ms$

The coarsest mesh ($5x2x25$) is used as basis for an adaptive concurrent multi-scale simulation aimed at an error less or equal than 0.2‰, corresponding to a refinement factor of 5.

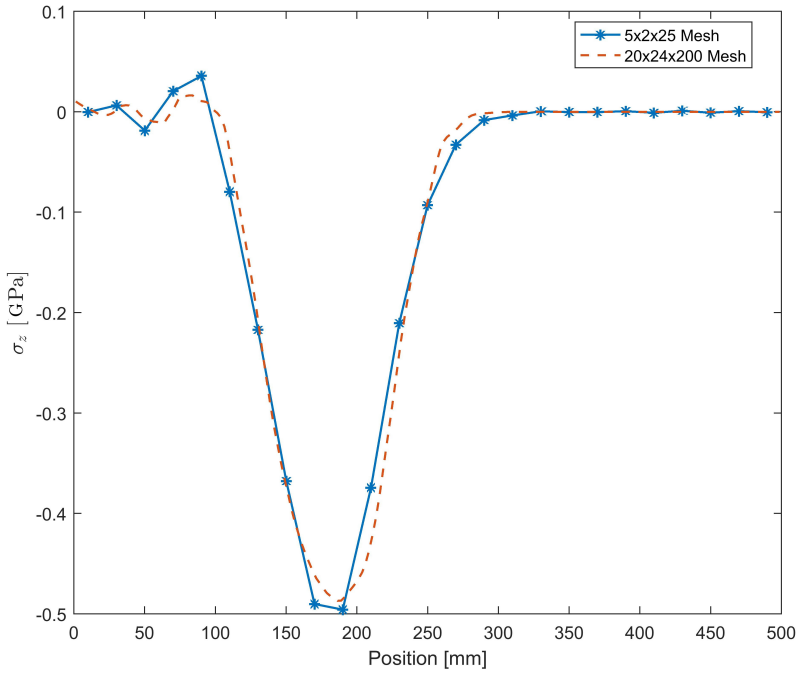

Figure 4.27: Comparison of the axial stress along the bar at $t = 0.05ms$. The coarser mesh present a higher amount of numerical error when compared to the solution with a finer mesh.

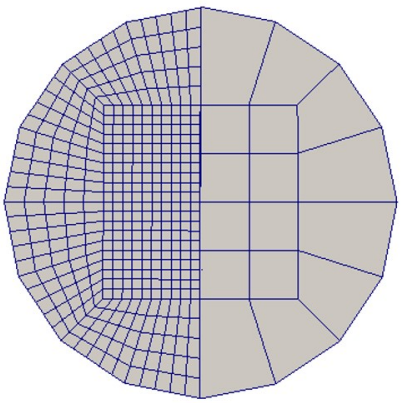

Figure 4.28: Cross section of the refined geometry and coarse scale. The proposed refinement algorithm can efficiently refine complex shapes, however it cannot represent the real geometry.

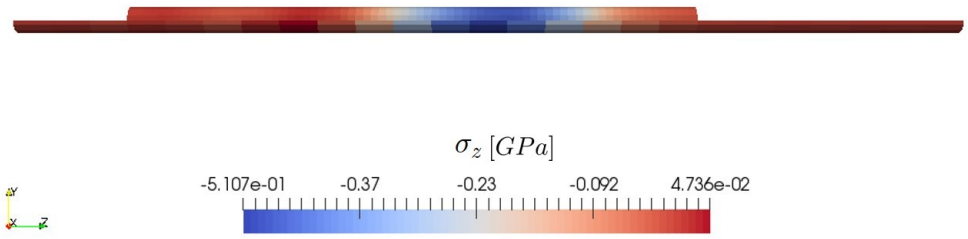

Figure 4.29: Comparison of the longitudinal stress at the small refined scale (upper mesh) and the coarse scale simulation (lower mesh) at t = 6.36e-2 ms. The refinement criterion highlights the elements interested by the wave, and triggers a multi-scale simulation whose results are reported in the top half of the image. Since the finer mesh can capture with a better resolution the evolution of the longitudinal stress over the computational domain, it is respresented with a smoother variation when compared with the coarse scale simulation in the bottom half.

Figure 4.28 shows a comparison among the refined and the original coarse scale mesh. The proposed refinement algorithm does not create distorted, or badly shaped elements, so the simulation is carried out without additional error due to highly distorted elements. However, the procedure is not able to recover the initial round geometry, reproducing the linear approximation of a circle around the edge of the circular section. The error estimator triggers at the coarse scale only the elements excited by the wave at each time step. The subsequent fine scale simulation, represented in the top half of figure 4.29, presents a smoother variation of the stress gradient given by the better resolution achievable with the bigger number of elements. This is compared against the coarse scale simulation, reported in the bottom half of figure 4.29, where the smaller resolution in the longitudinal stress is qualitatively noticeable in the less smooth transitions among different elements in the Z direction. From a quantitative point of view the solutions of the multi-scale and coarse scale simulations are compared in figure 4.30,4.31,4.32 and 4.33 in terms of axial velocity before

and after the reflection on the supported side of the bar. The multi-scale simulation represents a closer solution to the numerical solution predicted by the fine scale simulation presented in figure 4.27. As expected, after the reflection the wave changes from positive velocities to negative velocities of same magnitude to ensure that on the supported end of the bar the velocities are always zero. Both the mono-scale and the multi-scale simulations are able to capture the magnitude of the wave, however the mono-scale simulation results in an artificial increment of velocity after the pass of the wave due to numerical dispersion, as shown in 4.33. At the reflection, the coarse scale simulation presents a high error localized at $z = 500mm$, that is alleviated by the multi-scale simulation as shown in figure 4.37.
The stability of the multi-scale simulation is proved comparing the elastic and kinetic energy in the case of mono fine and multi-scale simulation in figure 4.34 and 4.35, whose trends show a very good agreement. Finally the multi-scale when compared to the mono-scale fine simulation presents an improvement in computational cost of 133 %.

The multi-scale response of the bar is compared with a fine mono-scale simulation in figure 4.36. The longitudinal velocities at $t = 0.637\ ms$ are compared, and the two solutions show perfect agreement. The delay of the multi-scale simulation with respect to the mono-scale simulation is only caused by a small difference in the numerical time step. It is interesting to note that for this particular configuration, in which the lateral inertia effects do not make a significant contribution, the presence of cusps along the outer edge of the multi-scale simulation does not alter the correctness of the solution.

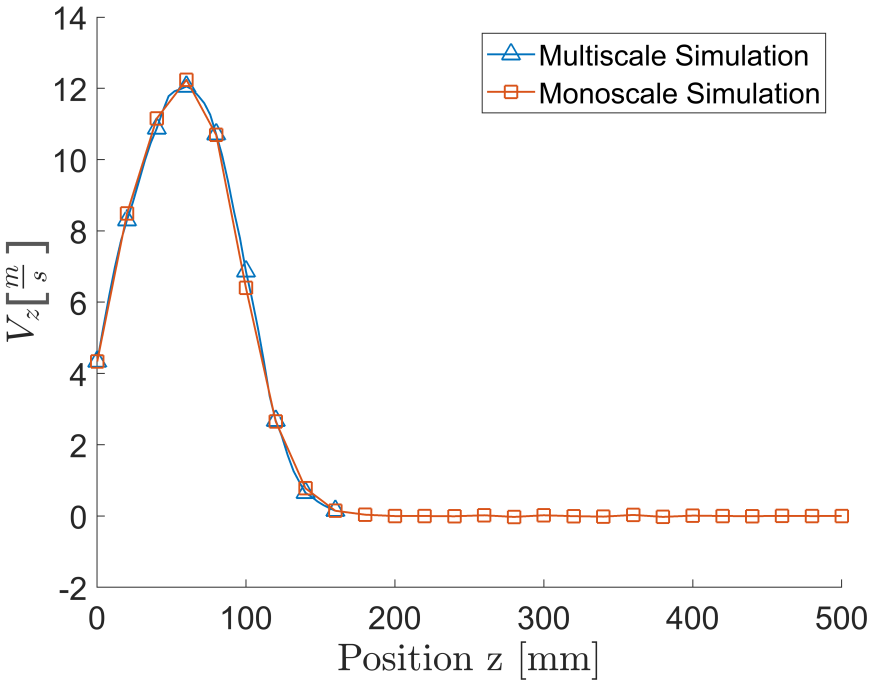

Figure 4.30: Case of slender circular bar. Comparison of longitudinal velocities for conventional and multi-scale simulation at t = 2.53e-2 ms

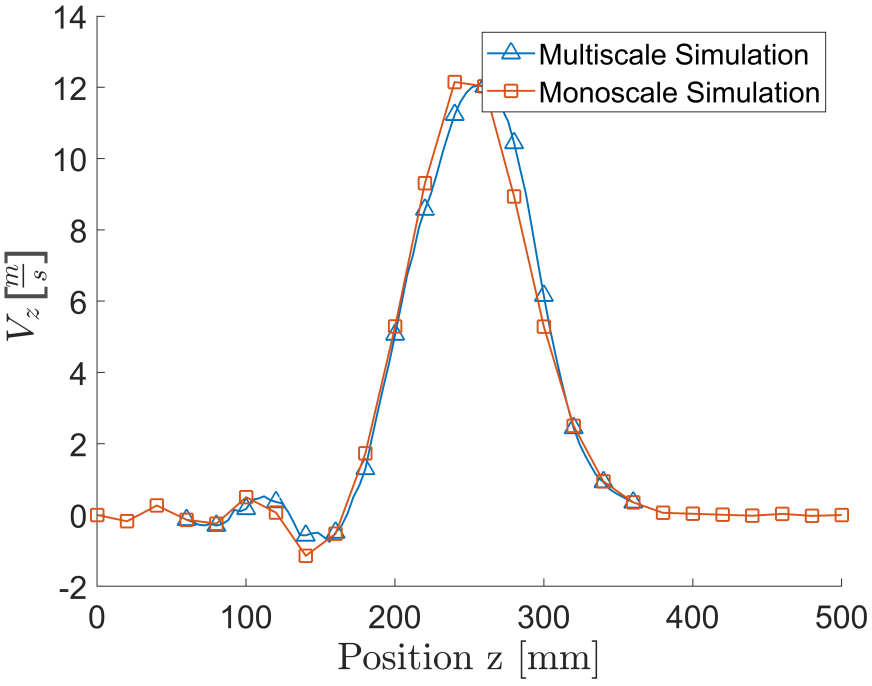

Figure 4.31: Case of slender circular bar. Comparison of longitudinal velocities for conventional and multi-scale simulation at t = 6.37e-2 ms

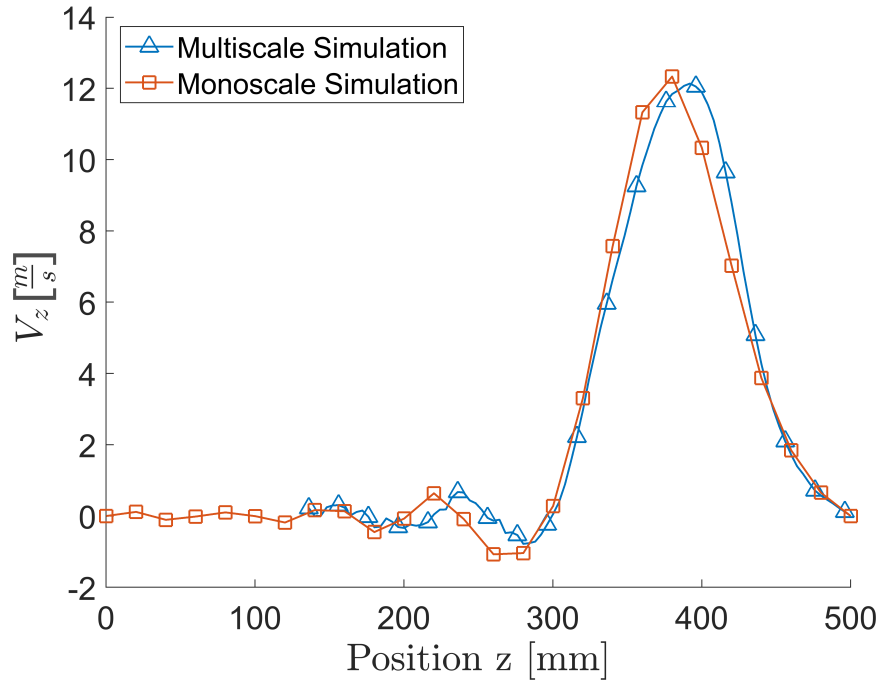

Figure 4.32: Case of slender circular bar. Comparison of longitudinal velocities for conventional and multi-scale simulation at t = 8.91e-2 ms.

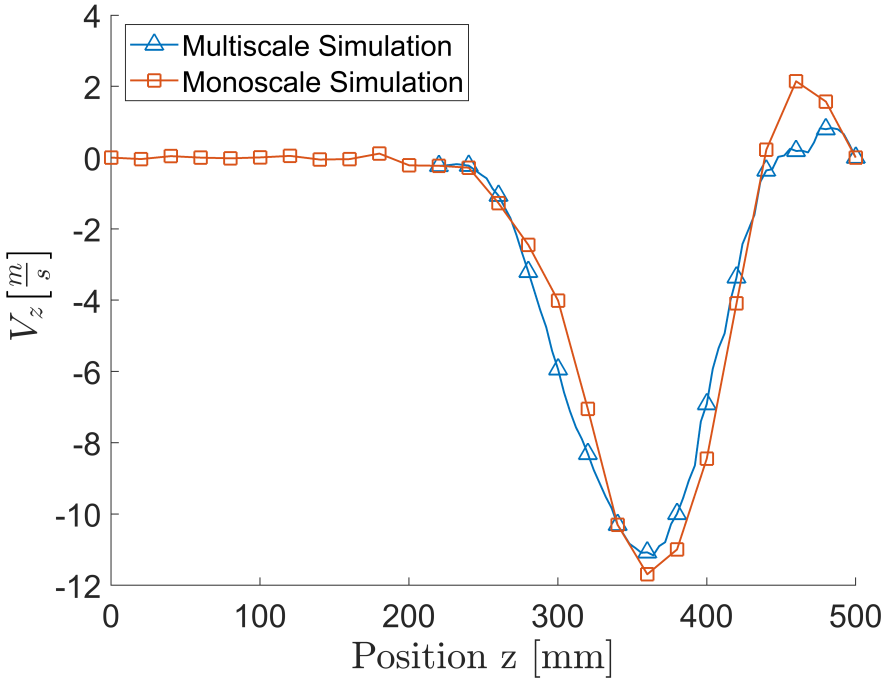

Figure 4.33: Case of slender circular bar. Comparison of longitudinal velocities for conventional and multi-scale simulation at t = 1.40e-01 ms.

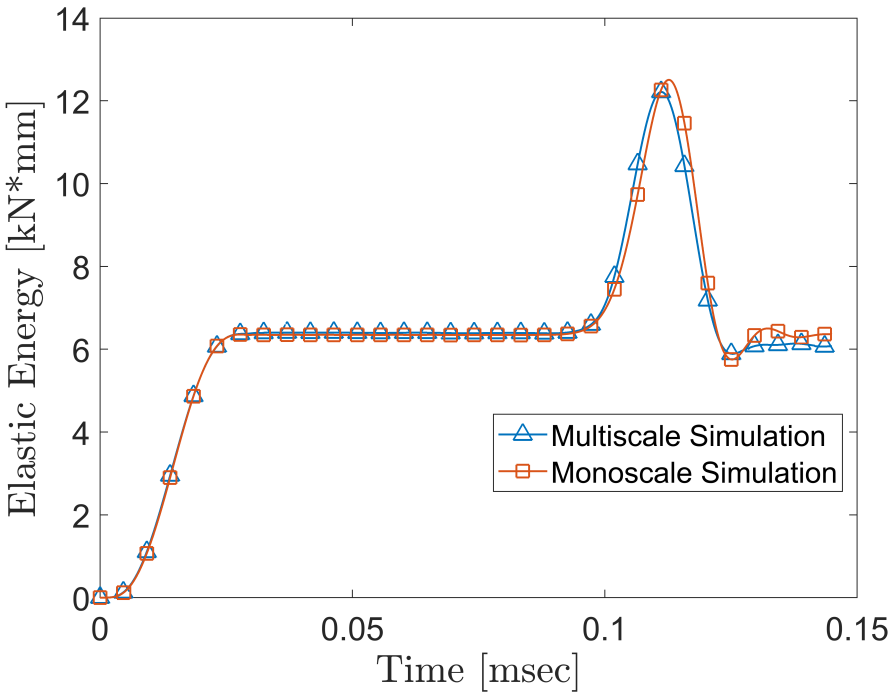

Figure 4.34: Elastic Energy for the whole domain as function of time, in the case of a slender bar. The similar trends show that the multi-scale simulation is stable.

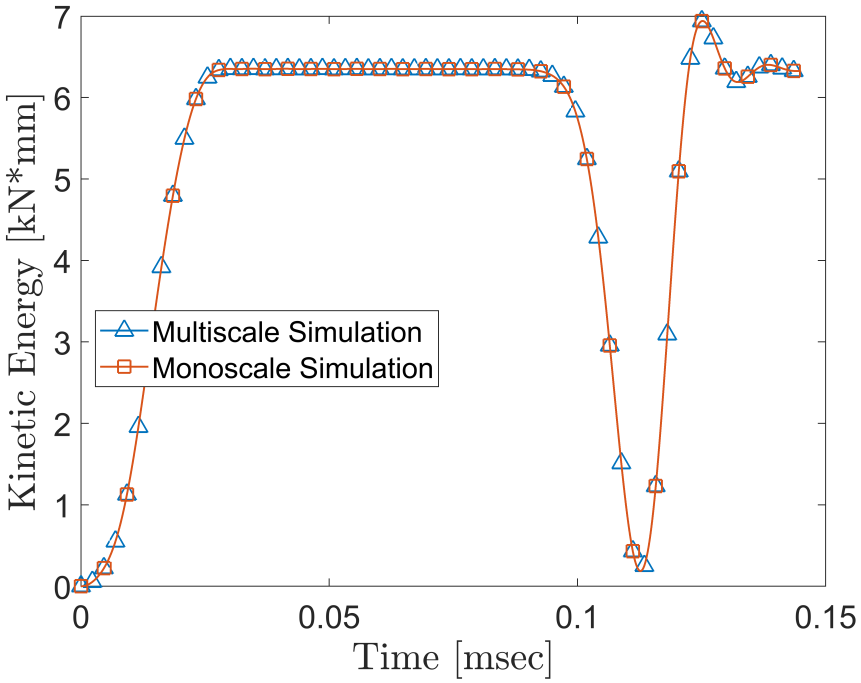

Figure 4.35: Kinetic Energy for the whole domain as function of time, in the case of a slender bar. The similar trends show that the multi-scale simulation is stable.

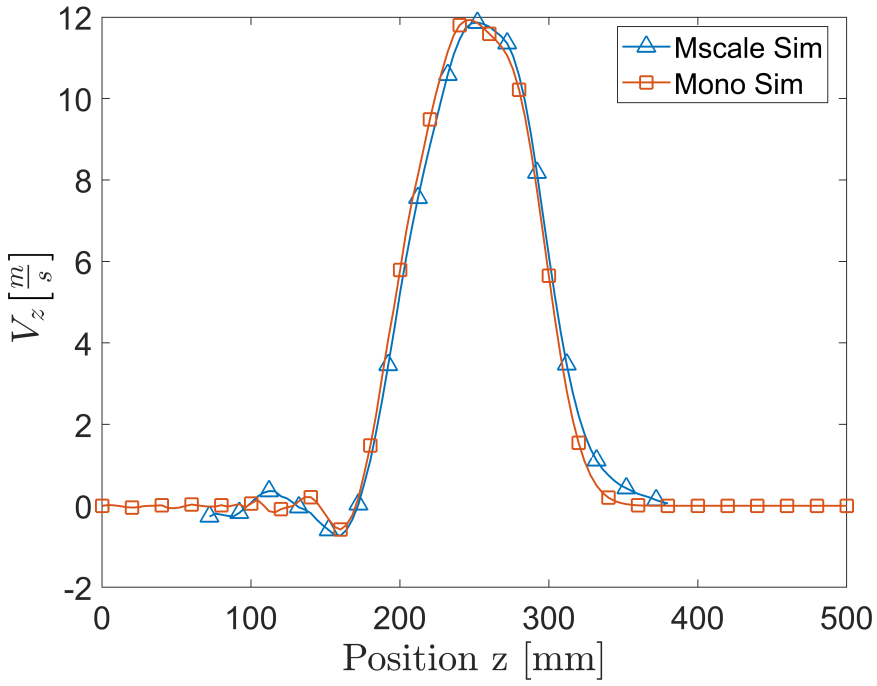

Figure 4.36: Comparison between multi-scale simulation and mono-scale fine simulation in terms of longitudinal velocities at $t = 6.37e^{-2}\ ms$. The two simulations show perfect agreement, confirming the validity of the proposed framework.

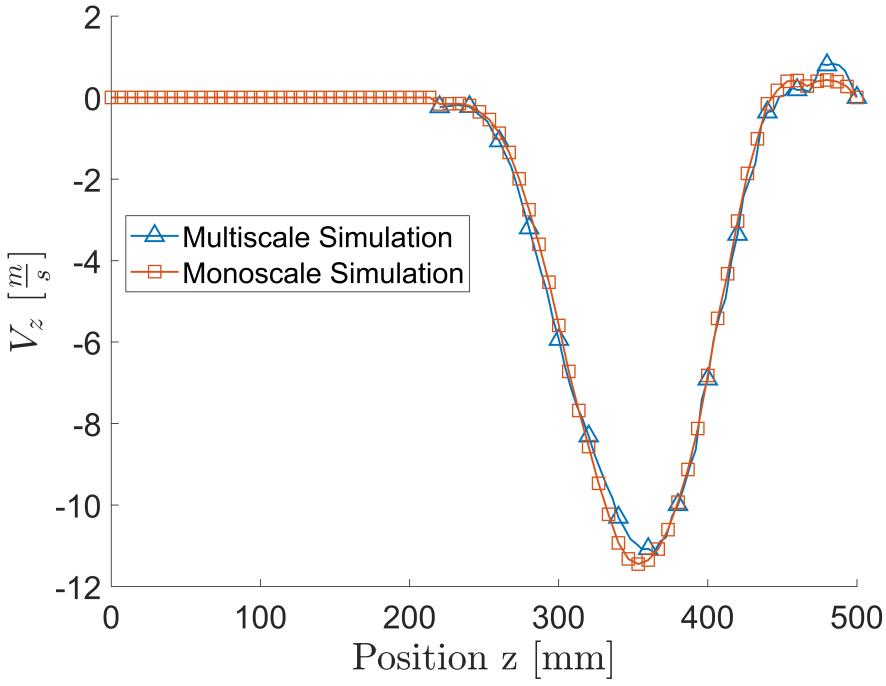

Figure 4.37: Case of slender circular bar. Comparison of longitudinal velocities for conventional and multi-scale simulation at t = 1.4e-1 ms.

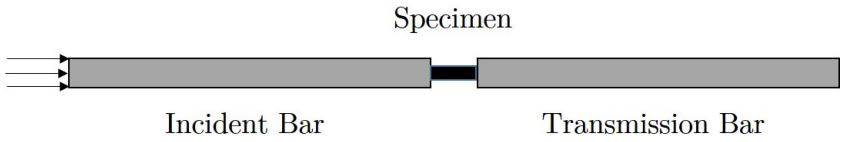

Figure 4.38: Split Hopkinson Bar apparatus configuration. A tensile pulse is generated in the incident bar which loads the specimen. The transmission bar serves as momentum trap for the apparatus.

4.5.4 Dynamic plastic localisation in dog-bone specimen

The characterisation of dynamic tensile properties of materials is generally accomplished with a device called tensile split Hopkinson pressure bar. The experimental set-up is composed by two elastic bars so called incident and transmission bars as it is schematically shown in figure 4.38. The specimen is mechanically gripped between both bars and the incident bar is pulled to produce an elastic tensile pulse which propagates towards the specimen. Once the compressive pulse reaches the interface between the incident bar and the specimen, part of it is reflected into the bar and part of it is transmitted to the specimen and afterwards into the transmission bar [106].

Test results are validated and interpreted following the main general assumptions. First and foremost, the incident and the transmission bars have to remain elastic through the whole test. Moreover, a purely one-dimensional, planar wave propagation is enforced in the incident and transmission bars assuring a ratio of $\frac{\Lambda}{D} << 0.2$. In order to assess the validity of the tests dynamic force equilibrium within the specimen is required. This ensures deformation is uniform across the specimen and initial inertia effects are overcome. Such condition is generally verified after the test, checking that the value of the axial forces at the bar ends have the same value within a tolerance. As a rule of thumb between four or five reflections of the wave are required to ensure dynamic equilibrium. The original Kolsky bar apparatus has been modified heavily to apply not only compressive but even tensile and torsion loading condition [106].

The application under consideration is the dynamic tensile test of a steel specimen in a tensile split Hopkinson bar. The focus of the application will be the correct

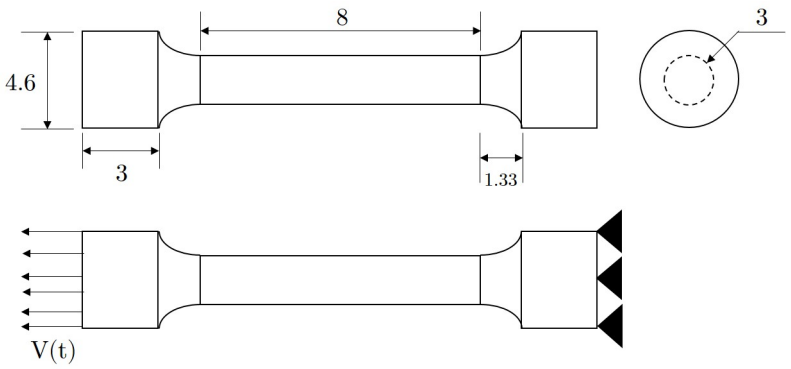

Figure 4.39: Specimen design for the simulation of dynamic plastic localisation in dog-bone specimen, with dimensions in millimetres (above). The specimen is pulled from one face while axially supported on the opposite face (below).

simulation of the evolution of the elastic and plastic response of the specimen. The specimen is the only modelled part of the whole apparatus, while the response of the bars is taken in account through the application of suitable boundary condition at the opposite sides of the specimen. Such approach for the simulation of split Hopkinson bar has been validated in [107]. The presence of a fillet between the shoulder and the gauge section avoids the formation of interface waves between the different sections as shown in figure 4.39. The interaction of the incident bar on the specimen is modelled through an applied velocity boundary condition over one face of the specimen, while the interaction with the transmission bar is approximated as an axial support.

Given the relative dimensions between the bar and the specimen, the applied velocity boundary condition can be idealised as a constant function in time with amplitude $A = 10\ \frac{m}{s}$. In dynamic simulations sharp rising times in the boundary conditions are generally smoothed as they could lead to excessive noise in the simulation. The application of a smoothing function results in the boundary condition

$$\begin{cases} V = A\tau^3(10 - 15\tau + 6\tau^2) & if \quad \tau \leq 1, \\ V = A & if \quad \tau > 1, \end{cases} \tag{4.20}$$

in which $\tau = \frac{t}{t_s}$ is defined as the ratio between the actual time and a smoothing time $t_s = 0.013\ ms$. This particular smoothing function is widely used and documented in [108]. The resulting boundary condition is depicted in figure 4.40.

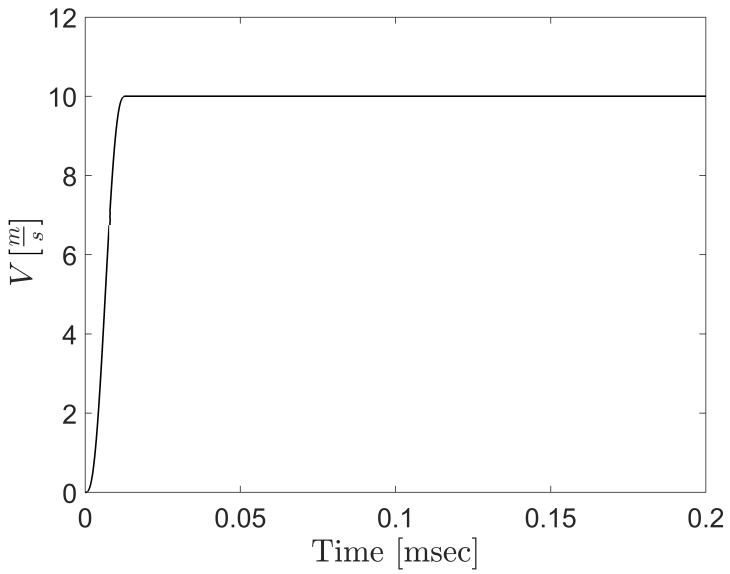

Figure 4.40: Smoothed applied boundary condition for dog-bone dynamic plastic localisation.

E	$197\,GPa$
ρ	$7.85e*10^{-6}\,\frac{kg}{mm^3}$
ν	0.33
σ_{Y0}	$270\,MPa$
E_T	$250\,MPa$

Table 4.6: Elastic-plastic isotropic steel material properties used in the simulation of dog-bone specimen.

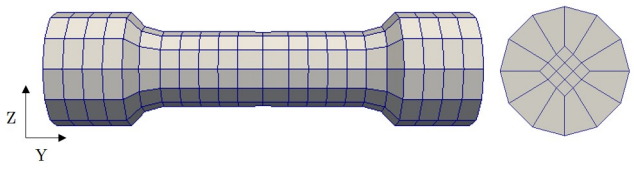

Figure 4.41: Coarse mesh for dog-bone specimen with $\ell_M = 0.7\ mm$.

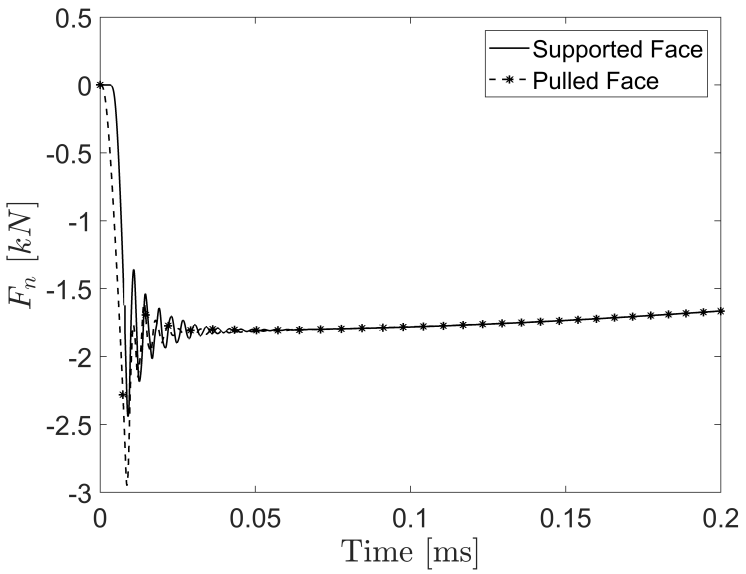

Figure 4.42: Comparison between the normal forces at the two opposite faces of the dog-bone specimen. When $t > 0.05\ ms$ the two forces are equal and opposite, therefore the condition of dynamic equilibrium is achieved.

	Coarse	Fine	multi-scale
Comp time	20	1263	1091
Final diameter	2.156	2.014	1.994
Maximum ϵ^P	6.422e-1	8.436e-1	8.421e-1

Table 4.7: Comparison between coarse, fine and multi-scale simulations. While the mono-scale fine simulation has a significantly bigger computational time than the coarse one, the multi-scale simulation yields to a solution in perfect agreement with the fine scale one with a saving, in terms of computational time, of 14%.

The material used for this simulation is silver steel, whose plastic behaviour is approximated with an isotropic strain-independent linear hardening. The material parameters are reported in table 4.6. The presented geometry is meshed using linear hexahedrons with two different mesh densities. The coarse mono-scale simulation presents an approximate mesh size of 0.7 mm as shown in figure 4.41 meanwhile the fine mono-scale simulation presents a characteristic length size of 0.23 mm. The dynamic equilibrium is verified summing the nodal forces on the nodes of the pulled face compared against the ones of the supported face. From figure 4.42 it is possible to verify that dynamic equilibrium is achieved at $t \approx 0.05\ ms$. Significant and localised

lateral displacement cause necking of the specimen at $t = 0.2\ ms$. Different predictions were obtained for the coarse and the fine mono-scale simulations as compared in table 4.7. The coarse mono-scale simulation predicts a final diameter of 2.15 mm and a maximum plastic strain of 0.6422, as shown in picture 4.43, meanwhile the fine scale simulation predicted a final diameter of 2.014 mm an a maximum equivalent plastic strain of 0.8436 as shown in picture 4.44. The coarse mesh results in a stiffer behaviour of the specimen, but it presents a sensible lower cost in terms of computational time.

The coarse scale mesh is used as a basis for a multi-scale simulation in which the focus is to correctly represent the elastic and plastic behaviour of the specimen. To this aim a different criterion for flagging the elements based on the plastic strain level is implemented in the developed framework, and set at a value of 0.02 equivalent plastic strain. At every time-step of the coarse scale simulation the current plastic strain of the macro-scale element is compared against the user-defined value. If the plastic strain is bigger than the given threshold, the element is flagged for refinement, together with its first neighbours, starting the multi-scale process. Once the elements of the coarse scale are flagged and refined the elastic part of the solution is interpolated on the new mesh using the scheme proposed in section 4.2 while the only state variable (the equivalent plastic strain) of the constitutive model is linearly interpolated from the integration points of the old mesh to the integration points of the new mesh.

In the multi-scale simulation the first elements to be flagged are the ones at the interface between the fillet and the gauge length close to the pulled side of the specimen. Here the plastic wave is generated and in the subsequent time-steps expands in the gauge until it reaches the fillet on the opposite side. Figure 4.45 depicts the evolution of the plastic wave on both the coarse and the fine scale. In particular it is possible to notice that the coupling, once the plastic wave has fully developed, is enforced over the fillet regions.

The multi-scale simulation results at $t = 0.02$ ms, in terms of maximum plastic strain and final diameter of the bar are shown in picture 4.46. When compared with the fine mono-scale the differences in these two parameters are negligible. The difference in the equivalent plastic strain, between the fine mono-scale simulation and the multi-scale simulation are shown in figure 4.47. Moreover the multi-scale simulation is 14% faster than the mono-scale fine simulation.

The relatively small gain in terms of computational time, is due to the fact that almost the whole computational domain is flagged for refinement at each coarse scale time-step, based on the user input threshold ϵ_*^P. In picture 4.48 three different multi-scale simulation with different threshold parameters are compared over time. When increasing the threshold parameter the time-step at which the multi-scale simulation starts shifts forward in time. Moreover, the portion of the coarse scale domain highlighted for refinement becomes smaller, and in the case in which $\epsilon_*^P > 0.3$, the multi-scale simulation is activated once the plastic wave has fully developed. The simultaneous action of these effects contributes to lower the overall computational cost of the multi-scale simulation, however the accuracy degrades as shown in figure 4.49.

Figure 4.50 quantifies the effects of the choice of ϵ_*^P in terms of accuracy and computational time. In this graph the error is measured as the difference between te maximum equivalent plastic strain at $t = 0.02$ and the same value for the fine mono-scale simulation. A small value of ϵ_*^P leads to small savings in terms of computational time, with respect to the mono-scale fine simulation. When $0.01 \leq \epsilon_*^P \leq 0.2$ the error is smaller than 5 % and the maximum saving of computational time is bigger than 60 %. This can be explained looking at both the propagation and localisation of the plastic wave. In these cases the threshold is sufficiently small to capture both the propagation an localisation of the computational domain and sufficiently high to highlight only the area where the plastic behaviour is more important. If $\epsilon_*^P > 0.2$, the propagation of the plastic wave is not captured and the multi-scale process only

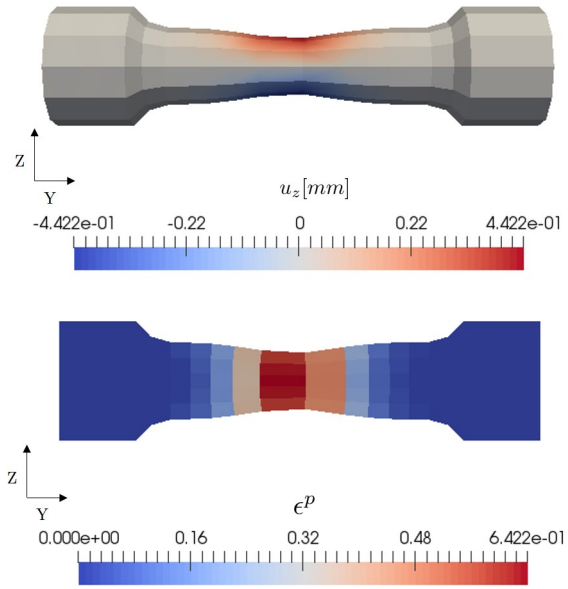

Figure 4.43: Results of the coarse scale simulation of the dog-bone specimen at t = 0.2 ms. The maximum displacement in the z direction is of 0.44 mm (above). The maximum value of equivalent plastic strain is registered in the middle of the specimen with a value of 0.64 (below).

captures the localisation. When this happens the error of the multi-scale simulation grows at a higher rate. It is important to note that the coarse scale and the fine scale represent respectively an upper and a lower bound for the multi-scale simulations. Based on this discussion for this particular configuration, the optimum value of ϵ_*^P is 0.2, which represents a simulation 66% faster than the fine mono-scale and an error smaller than 5%.

4.6 Concluding Remarks

This chapter has described the extension of the novel adaptive concurrent multi-scale framework proposed in chapter 3 to a three dimensions environment using the most popular element type, namely the uniform strain hexahedrons. The first key difference among the 1D and 3D applications is in the topology of the computational mesh which requires handling of the shared faces and edges among the the different elements when refining them on a lower scale. At the same time 3D mesh, especially

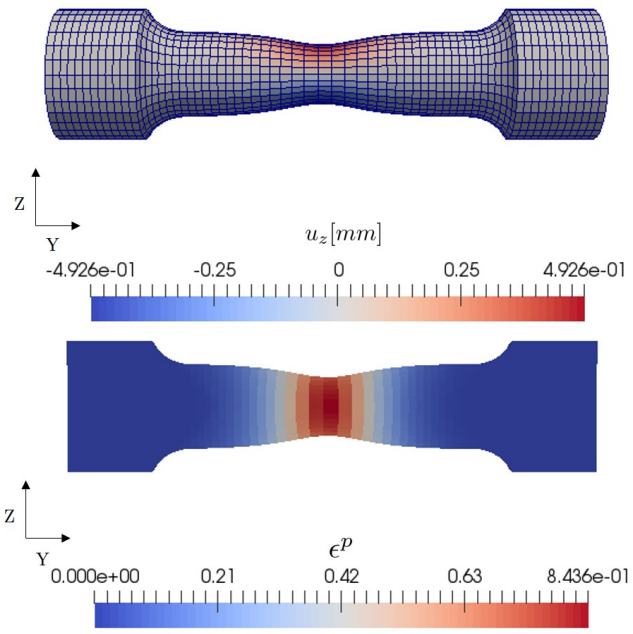

Figure 4.44: Results of the fine scale simulation of the dog-bone specimen at t = 0.2 ms. The maximum displacement in the z direction is of 0.4926 mm (above). The maximum equivalent plastic strain is registered in the middle of the specimen with a value of 0.8436 (below).

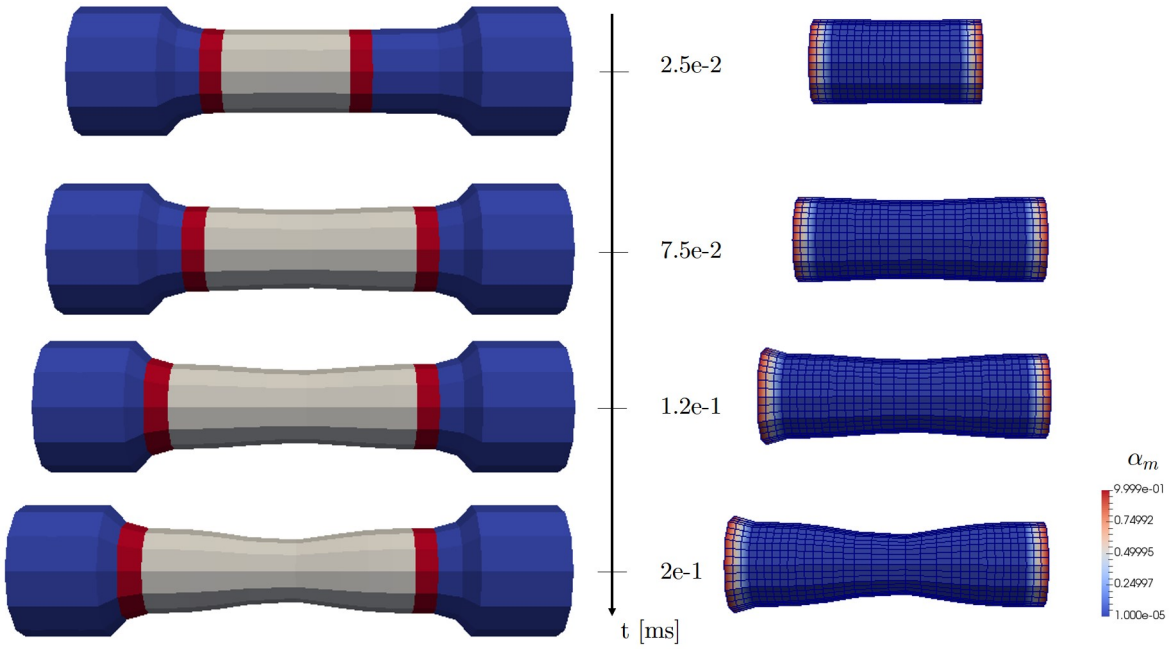

Figure 4.45: Evolution of the plastic wave over time, alongside the refined mesh. On the left side the elements of the coarse scale are flagged over time, and the boundaries of the highlighted area are used to enforce the coupling at the micro-scale through α_m.

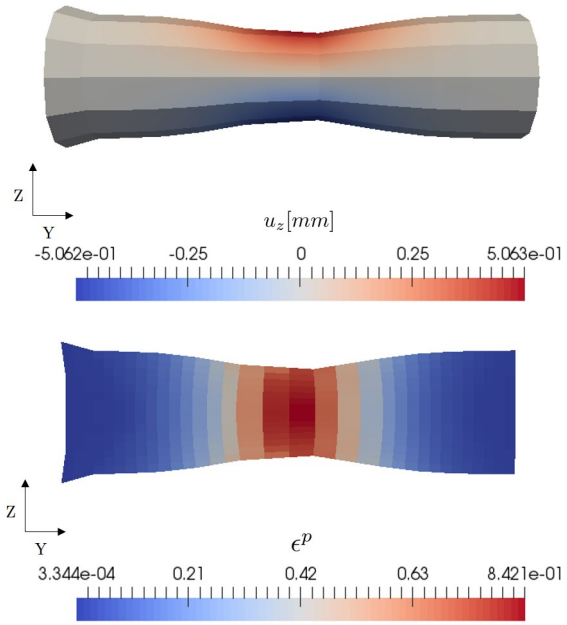

Figure 4.46: Results of the multi-scale simulation of the dog-bone specimen at t = 0.2 ms. The maximum displacement in the z direction is of 0.506 mm (above). The maximum equivalent plastic strain is registered in the middle of the specimen with a value of 0.8421 (below). The differences with the fine mono-scale simulation are less than 2%.

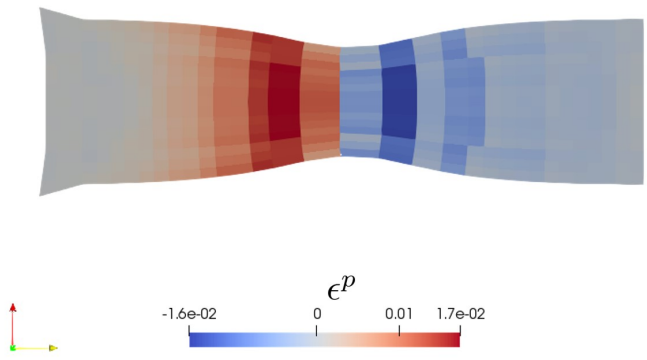

Figure 4.47: Comparison of the multi-scale simulation of the dog-bone specimen at t = 0.2 ms. The figure is obtained computing for every integration point the difference of the plastic equivalent strain between the fine mono-scale simulation and the multi-scale simulation.

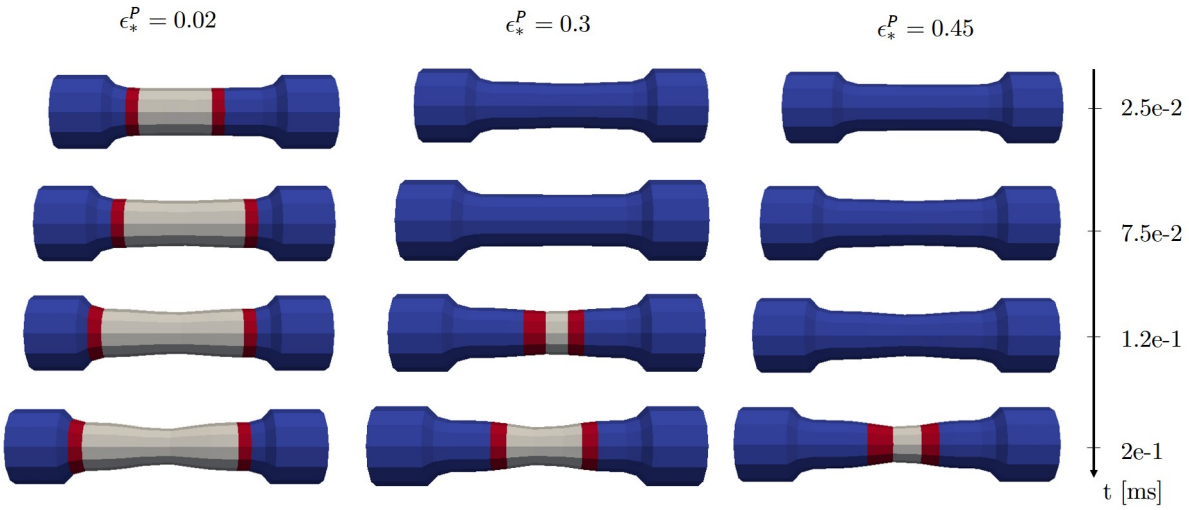

Figure 4.48: Flagging process of the coarse domain with different choices of the threshold parameter ϵ_*^P. Increasing the threshold value the multi-scale process starts later in time. Moreover the highlighted portion of the domain becomes smaller.

in updated Lagrangian frameworks, can contain highly distorted elements which can hinder their refinement due their shape. These two different aspects have been tackled simultaneously proposing an efficient refinement strategy that first refines the coarse scale elements in their parent element domain, and subsequently maps them on the deformed configuration. The proposed algorithm is demonstrated to generate well shaped computational meshes, in a range of applications.

Particular attention in this chapter is also given to the data transfer form the original coarse mesh to the refined one. In Chapter 3 the hermitian interpolant has been demonstrated to minimise diffusion while ensuring a correct equilibrium between the internal external and inertia forces at the fine scale, however its extension is not trivial given the big number of coefficients needed to interpolate a full polynomial in 3 dimensions. In this chapter an extension of such interpolant is proposed developing a reduced scheme in which the number of unknown coefficient equals exactly the number of conditions that can be imposed over a eight nodes hexahedron. Such polynomial takes into account not only the value of the kinematic variables to interpolate at the lower scale but their derivatives as well, creating fields that do not present discontinuities in their derivatives which are common when linear shape functions are

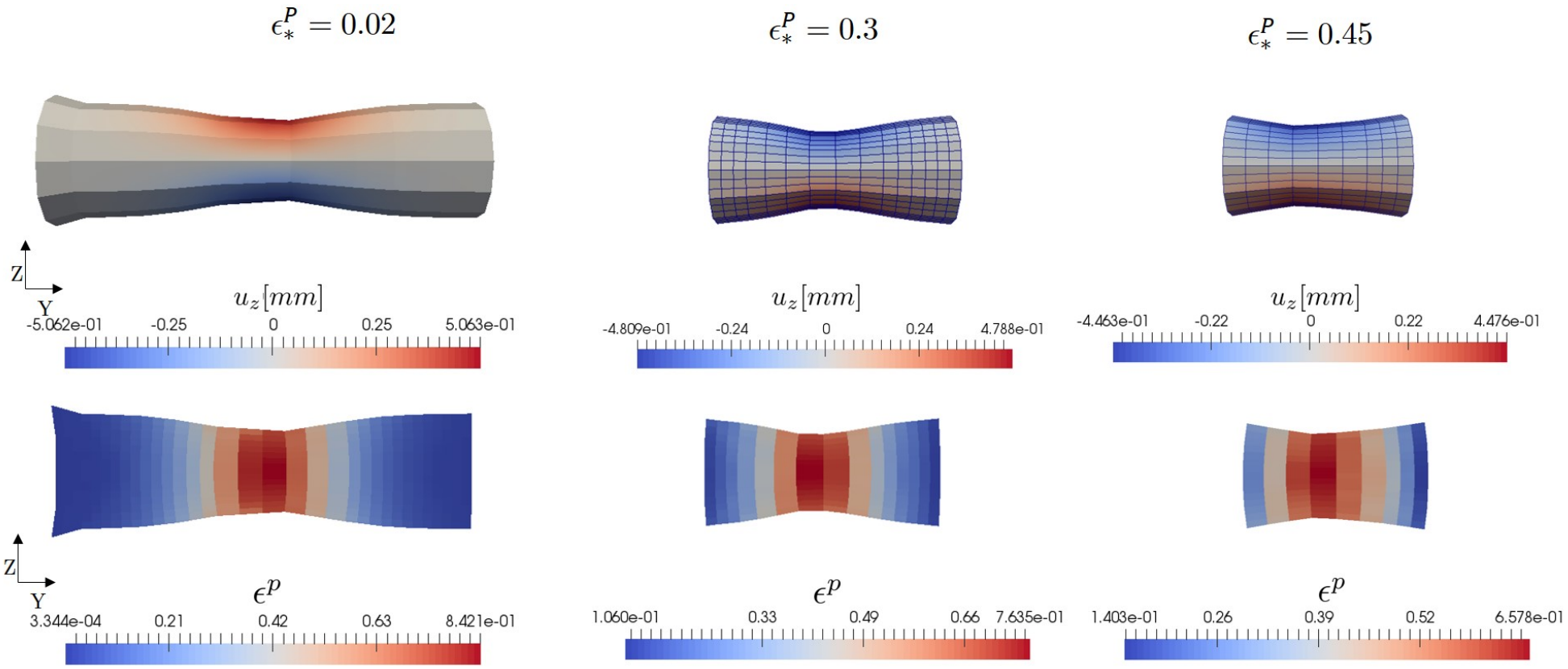

Figure 4.49: Results of the multi-scale simulations with different values of ϵ_*^P at t = 0.2 ms. The highlighted are for refinement is smaller at higher values of the threshold, however the accuracy of the simulation decreases.

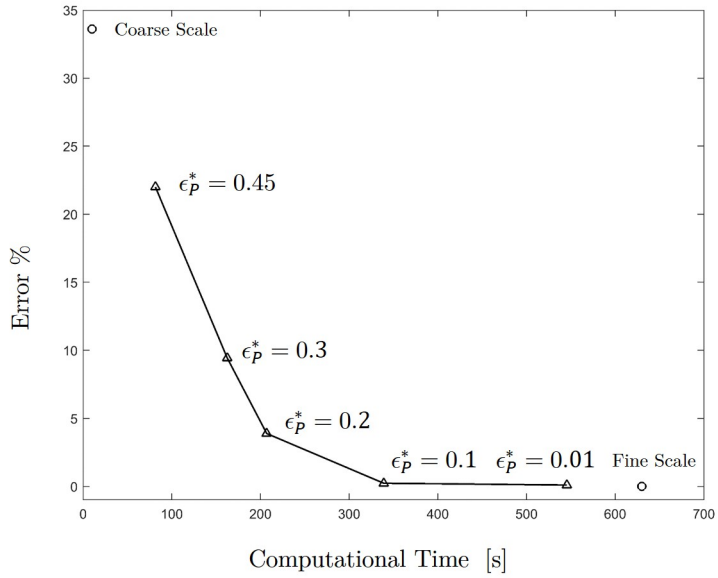

Figure 4.50: Parametric study of the Threshold parameter for the multi-scale simulation. Small values of ϵ_*^P result in high computational cost and low error. On the other hand high values result in an error close to the coarse mono-scale simulation. The non linear behaviour of the error highlights at optimum value of the threshold value of 0.2.

employed.

The mathematical developments, are implemented in a novel framework, in which particular attention is given to the computationally efficiency and the versatility. This is accomplished by idealising the different areas of an adaptive concurrent multi-scale simulation as separate modules comprising the framework, that once validated can be further extended to reach the objectives of this research.

The developed 3D framework has been tested with various dynamic applications ranging from elastic to elastic-plastic wave propagation in a range of different geometries. In the first application, the framework has been validated using a simulation with a null Poisson's ratio. The presence of lateral inertia was studied in Section 4.5.2. In particular, through a parametric study of the coupling function, it has been demonstrated that the proposed coupling only affects the spurious waves and does not modify the mechanical response of the structure. Subsequently, the multi-scale framework has been used to simulate a slender circular bar, in a configuration where

the wave propagation could be considered planar. In this case, even if the refinement procedure is not able to reproduce the rounded geometry, the multi-scale simulation can still correctly simulate the wave propagation with a computational time saving of 113%.

In the last section,the framework has been applied to a case of dynamic plastic localisation of a dog-bone specimen. In this case the multi-scale computation is not based on the norm of the error, but rather on the accumulation of equivalent plastic strain in the elements. This scalar, defined a priori, determines the time at which the multi-scale procedure is started as well as the extent of the plastic area, directly affecting the accuracy and the computational time. Even if the multi-scale simulation has always a lower computational time when compared to the fine mono-scale simulation, an optimum can be achieved changing the value of the minimum equivalent plastic strain that activates the multi-scale procedure.

In these applications it has been demonstrated that the proposed coupling does not introduce spurious wave reflections at the interface between coarse and fine mesh, and that it does not affect the mechanical behaviour of the structures under consideration. Finally, it has been demonstrated that the proposed data transfer of the results between the coarse and fine scale meshes does not alter the equilibrium among the internal, external and inertial forces. This chapter provided a guideline for the construction of a stable coupling, however the approach followed is valid only for hexahedrons and cannot be readily applied to other element types (e.g., tetrahedrons, bars) unless hermitian polynomials are constructed for these other classes of elements.

Chapter 5

Conclusions and further work

This chapter draws the main conclusions of this doctoral thesis and summarizes the key contributions made to the field. Firstly, a summary highlights the main findings and novelties of the work. A list of contributions of this research to the field of concurrent multi-scale analysis is included. Finally, a list of research developments and future activities is suggested.

5.1 Summary

The aim of this doctoral thesis was to develop a dynamic concurrent multi-scale framework capable of adaptively refining the computational mesh, allowing the simulation of big structures with high detail and low computational cost. To accomplish this aim an extensive literature on multi-scale simulation techniques was provided. A clear distinction was made between hierarchical semi-concurrent and concurrent multi-scale techniques in both static and dynamic simulations.

In the context of dynamic concurrent multi-scale schemes the key problem is the correct representation of the stress waves travelling through the fine and coarse computational domains without generating numerical artefacts, known as spurious wave reflections. Different solutions to this problem have been reviewed, however they all require a substantial computational effort that becomes prohibitive when large domains are coupled. Such complications hinder the application of these schemes to

adaptive explicit frameworks and, as a result, none of the existing frameworks present a simultaneous treatment of different time and length scales, avoiding the generation of spurious reflection at the interfaces between the different domains.

This gap identified in the literature review served as basis for the formulation of a novel adaptive concurrent multi-scale framework presented in section 3.2, in which a high computational efficiency is achieved through the formulation of a coupling that does not require the assembling of matrices. The link among the different meshes is based on the evaluation of nodal forces that ensures continuity of the velocity and absence of spurious wave reflections over the coupled domains. Subsequently, in section 3.3.3 different error estimators are compared for the assessment of the quality of the solution of a mesh and a novel computationally efficient error estimator based on hermitian interpolation is proposed. The main advantage of the proposed estimator is that it can be used simultaneously to check the error and, if necessary, transfer the elastic kinetic and kinematic variables on the new generated mesh. Different simulations and parametric studies in section 3.3.4 and 3.3.5 were used to validate the developed framework in 1D.

In Chapter 4 the framework is extended to three dimensions using linear hexahedrons with one integration point. Section 4.2 highlights the main challenge in the extension of hermitian polynomials to the 3D space, given by the presence of 64 unknown coefficients and only 32 conditions for every hexahedron. A reduced third order interpolation scheme is proposed in which the number of unknowns equals the number of conditions. Subsequently in section 4.3, a novel refinement algorithm is developed for the generation of computational meshes with complex topologies at the macro-scale. This new algorithm avoids the generation of distorted meshes by refining every element in the parent element domain and then mapping the new nodes on the current configuration. These two features together with the previously developed coupling are the basis of the concurrent adaptive multi-scale 3D framework. In the last part of Chapter 4, various applications are examined ranging from elastic to

elastic-plastic dynamic wave propagation. It was found that the newly developed error estimator is suitable for the flagging of elements that present a relative high error and that the refinement algorithm proposed can generate valid meshes for real structures including specimen geometries. Different parametric studies concluded that the proposed nodal coupling is able to represent the fine scale behaviour filtering out only the non-physical spurious waves while retaining the real response of the fine scale. Finally in terms of computational cost, the adaptive concurrent multi-scale simulations always presented significant time savings when compared to a fine mono-scale simulation.

5.2 Contributions

The main contributions of this doctoral thesis are listed below.

- The coupling among the different discretisations is achieved through the definition of a coupling volume, in which a weighting parameter α_m blends the different contributions of the coupled scales to the total energy of the system. In this work the weight has been associated directly to nodal positions rather than to elements. The advantages of this new formulation are several. Firstly, the elements do not need to use modified integration rules to take into account the spatial distribution of the weighting parameter. In second instance, the evaluation of the the internal forces, coming from the constitutive model, does not have to explicitly include the weighting parameter and therefore, contrarily to other frameworks where overlapping volumes are used, the original constitutive material model can be used without modifications. Moreover, section 3.2 demonstrates that the stable time-step of the simulation is not affected by the use of nodal weights. Finally, the coupling is represented through the evaluation of nodal forces that do not make use of any matrix, making the coupling versatile and suitable for explicit simulations. The stability of the proposed

coupling has been verified both analytically in section 3.2.3 and through simulations in section 3.3.4 showing that it ensures a correct energy transfer between the scales.

- The adaptive process for elastic simulations is driven by a novel error estimator based on hermitian polynomials. The error estimation uses only data that are local to each element of the mesh, therefore it avoids neighbour searches that can become computationally expensive in complex meshes. The main advantage of such methodology resides in the computation of a higher order interpolation of both kinetic and kinematic quantities, as opposed to only kinetic quantities in the classical estimators. Moreover, the proposed methodology does not require the assembling and inversion of matrices resulting in high computational efficiency. The convergence rate of the proposed error estimator is compared against the classical ZZ procedure and the analytical error, in the case of 1D elastic wave propagation. It is found that the estimated error shows the same trends of the analytical error, justifying its application in dynamic problems. In section 4.2 the proposed estimator has been extended to three dimensions, using the crucial quintic order expansion of equation **??**. The use of such expansion reduced the order of unknown interpolation coefficients from 64 to 32, making possible the use of error estimators in 3D settings. The application in section 4.5.3 found that the rate of convergence of error for the 3D case is comparable to the 1D case.

- A consistent data transfer from the coarse scale to the fine scale is defined using the hermitian interpolation previously developed. In particular, the classic schemes use the shape functions to transfer both the kinetic and kinematic data, however it results in numerical diffusion and unbalanced internal and external forces. In the classical scheme the equilibrium at the fine scale is achieved through a balancing step. The use of the hermitian interpolation functions for

the transfer of kinetic and kinematic data presents two main advantages. In first instance, since by definition hermitian polynomials preserve the value of the function to interpolate together with its derivative, it reduces significantly the numerical diffusion at the lower scale. Secondly the balancing step is avoided since the kinetic quantities (in the hypothesis of elastic behaviour) are directly derived by the C^3 field of the displacements.

- Once the error has been assessed at the coarse scale and the refinement factor has been computed based on the previously verified rate of convergence, the highlighted elements are refined using a novel computationally efficient algorithm. The proposed procedure refines individually every element in its parent domain and subsequently maps the new nodes on the current configuration. An efficient lookup is implemented to take into account shared faces and edges among different elements. The biggest advantage of this procedure is that it is general and can handle different topologies, since the parent element domain is the same for every element. Moreover since the refinement procedure does not rely on geometric dimensions in the current configuration, the probability of generation of highly distorted elements is avoided altogether. The effectiveness and the computational efficiency of the procedure are verified in section 4.5, where different computational coarse meshes are refined using different refinement factors.

The different contribution in terms of mesh coupling, error estimation, data transfer and mesh refinement have been implemented in a single adaptive concurrent multiscale modelling framework for dynamic phenomena. The different advantages listed above together with a clever data structure implementation result in a versatile, easy to use and efficient framework as demonstrated in Chapter 4.

5.3 Limitations and proposed further work

The aim of this doctoral thesis was to create and validate a novel and efficient dynamic adaptive concurrent multi-scale framework. For such reason the main applications of this thesis have been focused to the simulation of dynamic events in homogeneous media.

The methodology, however, needs further improvement to be applied to problems involving heterogeneous materials and coupling between different element representations (e.g. hexahedra and beam elements in the same computational model) and multi-scale modelling involving different constitutive models. In particular, such limitations can be resumed in:

- As shown throughout this thesis, different functions need to be created fo every element to interpolate the solution between meshes. Such functions are provided in this dissertation for bar elements in 1-dimension and hexahedra in 3-dimensions. However for every element a new interpolation has to be derived, as described in Chapter 4, to ensure a consistent data transfer among coarse and fine scales.

- In cases in which the finer scale needs to be described with a different constitutive model from the coarse one, the proposed hermitian interpolation ceases to be valid because the macro-scale state does not hold information about micro-scale features, such as potential micro-fluctuations generated by micro-inertia and stiffness mismatches. While a direct interpolation strategy from the macro to micro-scale sounds appealing especially because of its reduced computational cost when compared to a balancing step methodology, the data transfer, for this class of problem, needs to be improved if not changed altogether.

- It has been demonstrated in this doctoral thesis that the proposed coupling dissipates a certain amount of energy in the low frequency regime. Even if such

effect diminishes with the increase of the coupling length its effects need to be examined when coupling different constitutive models at different scales, since the loss of energy may be significant and may affect the results.

- The proposed refinement scheme, based on divisions of the coarse-scale mesh, does not take in consideration the real geometry of the structure. For the applications considered in this thesis, this does not constitute a source of error, however for dynamic problem on real structures with complex geometries (e.g. engine blades) or contacts, the possibility of refining the computational mesh and the geometric representation of the body is paramount for a correct interpretation of the results.

The current limitations of the frameworks, if carefully addressed, could use the proposed framework as the basis of more complex dynamic problems such as:

- Continuum damage mechanics simulations in which the regularisation process, necessary to avoid mesh dependent results, leads to prohibitive element characteristic lengths. In this context the mesh size could be initially coarse enough to capture the elastic loading up to failure initiation and, once damage is detected, the mesh size could be refined in the proposed framework to ensure the correct energy dissipation.

- The adaptive coupling of heterogeneous materials in which the coarse scale is represented by a homogeneous material while the heterogeneities are explicitly represented at the micro-scale. In this scenario most of the research should be devoted to the data transfer among the two scales, because the current approach assumes that the displacements at the micro-scale can be directly interpolated from the macro-scale. However, when including heterogeneities this assumption does not hold true and one solution to account for micro-inertia and stiffness mismatches, at the micro-scale, could be the use of an intermediate balancing step.

- Enhancement of the proposed refinement algorithm to account for the real geometry of the structure in consideration. In this context, a future improvement could be the mapping of the new nodes on the real geometry in the current configuration. As an example, this could be achieved retaining the NURBS representation of the original geometry once the coarse scale mesh is built, allowing the nodes generated at the fine scale to be projected directly on the NURBS.

Appendix A

Hermitian interpolation in three dimensions

In this section the explicit form of the interpolation used defined in the equation 4.6 will be derived. The equations in section 4.2 are solved using the symbolic math toolbox of MATLAB since they involve heavy matrix operations, un-expensive for modern computers. The values of the obtained interpolation functions are validated verifying the Kronecker Delta property.

A.1 Code implementation and verification

The data transfer scheme in 3-dimensions makes use of a reduced hermitian interpolation polynomial introduced in section 4.2. The procedure requires the determination of the entries of the matrix $\boldsymbol{\mathcal{H}}(\boldsymbol{\xi})$ in equation 4.9 that cannot be accomplished by hand since it requires the solution of the system of equations represented by equation 4.14 and 4.16 in 32x32 unknowns. To this aim the whole procedure described in section 4.2 has been coded in MATLAB, using the symbolic math toolbox. In this environment the variables declared as symbolic through the use of the command `syms` are treated as mathematical entities allowing analytical differentiation, integration, simplification, transforms, and equation solving.

In particular, in the script A.1, the parent element domain space $\boldsymbol{\xi}$ is declared as symbolic on line 4. The exponents of the polynomial expressed in equation 4.11 are

stored in the variable `expon` and the coordinates of the hexahedron parent element domain reported in table 4.1 are stored in the variable `Csi`. The array matrix $\boldsymbol{G}$ of equation 4.11 that contains all the polynomial terms of the reduced expansion is constructed on line 54 using a `for` loop statement in which the coordinates are raised using their respective exponent. The coefficient matrix represented by the equations 4.14 and 4.16 is built in 4 different `for` loops. The $32x32$ matrix representing the union of the 32 $\boldsymbol{U}^{k}_{1x32}$ is assembled on line 80. Finally, the system of equation for $\boldsymbol{\mathcal{X}}$ is solved on line 86, and the matrix $\boldsymbol{\mathcal{H}}$ containing the entries of the reduced hermitian interpolation is determined through a simple matrix multiplication on the last line of the script.

```
1
2  clearvars
3  X = sym('X%d_%d', [32 32]);
4  syms x y z
5
6  % Coordinates of parent element hexahedron
7  Csi= [
8  -1  -1 -1;
9   1  -1 -1;
10  1   1 -1;
11 -1   1 -1;
12 -1  -1  1;
13  1  -1  1;
14  1   1  1;
15 -1   1  1;];
16
17
18 expon = [
19 0,0,0;
20 0,0,1;
21 0,1,0;
22 0,1,1;
23 1,0,0;
24 1,0,1;
25 1,1,0;
26 1,1,1;
27 2,0,0;
28 2,0,1;
29 2,1,0;
30 2,1,1;
31 3,0,0;
32 3,0,1;
```

```
3,1,0;
3,1,1;
0,2,0;
0,2,1;
0,3,0;
0,3,1;
1,2,0;
1,2,1;
1,3,0;
1,3,1;
0,0,2;
0,0,3;
0,1,2;
0,1,3;
1,0,2;
1,0,3;
1,1,2;
1,1,3];


for i = 1:length(expon)
G(1,i) = x^expon(i,1) * y^expon(i,2) * z^expon(i,3);
end

G = matlabFunction(G);
dGx = matlabFunction(diff(G,x));
dGy = matlabFunction(diff(G,y));
dGz = matlabFunction(diff(G,z));

for i =1:length(Csi)
C(i,:) = [G(Csi(i,1),Csi(i,2),Csi(i,3))]*X;
end


for i =1:length(Csi)
C(end+1,:) = [dGx(Csi(i,1),Csi(i,2),Csi(i,3))]*X;
end


for i =1:length(Csi)
C(end+1,:) = [dGy(Csi(i,1),Csi(i,2),Csi(i,3))]*X;
end

for i =1:length(Csi)
C(end+1,:) = [dGz(Csi(i,1),Csi(i,2),Csi(i,3))]*X;
end

U = eye(32,32);

equations = C == U;

[a,b] = equationsToMatrix(equations, X);

X_sol = reshape(a\b,[32,32])
```

```
87  H = G*X_sol;
```

Code A.1: MATLAB code for the determination of the reduced hermitian interpolation presented in Chapter 4

The proposed interpolation can be considered valid if it reproduces the values of the original field on the node of the hexahedron. This is ensured when the shape functions that interpolate the field have a value of 1 on one node and 0 on the others. In figure A.1, the value of the interpolation functions are summed at every nodal position. The proposed reduced hermitian scheme in three dimensions is therefore validated since the sum of the 32 interpolation functions present a value of 1 on the eight vertices of the hexahedron.

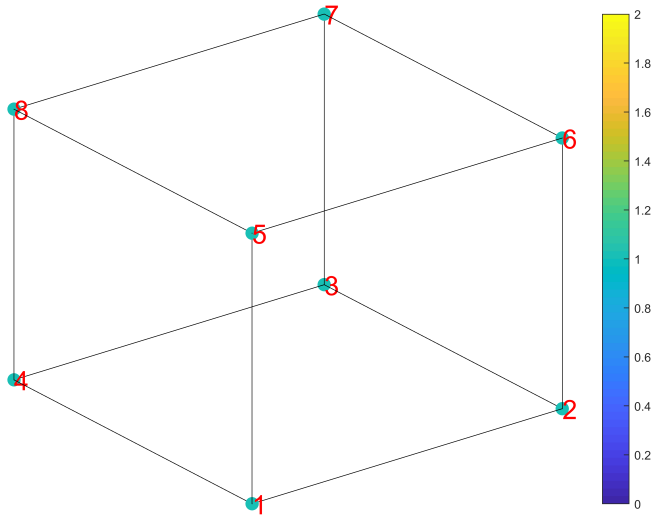

Figure A.1: Validation of the proposed hermitian interpolation scheme. The methodology is validated since the sum of proposed functions have a value of 1 on the vertices of the hexahedron.

References

[1] M. Geers, V.G. Kouznetsova, and W.A.M. Brekelmans. Multiscale first-order and second-order computational homogenization of microstructures towards continua. *International Journal for Multiscale Computational Engineering*, 1(4):371–386, 2003.

[2] A. Ghosh and P. Chaudhuri. Computational modeling of fracture in concrete using a meshfree meso-macro-multiscale method. *Computational Materials Science*, 69:204–215, 2013.

[3] L.P. Canal, C. González, J. Segurado, and J. LLorca. Intraply fracture of fiber-reinforced composites: Microscopic mechanisms and modeling. *Composites Science and Technology*, 72(11):1223–1232, 2012.

[4] M. Silani, H. Talebi, S. Ziaei-Rad, A. M. Hamouda, G. Zi, and T. Rabczuk. A three dimensional extended arlequin method for dynamic fracture. *Computational Materials Science*, 96:425–431, 2015.

[5] T. Belytschko and R. Mullen. Mesh partitions of explicit-implicit time integration. *Formulations and Computational Algorithms in Finite Element Analysis*, pages 673–690, 1976.

[6] A. Prakash and K.D. Hjelmstad. A feti-based multi-time-step coupling method for newmark schemes in structural dynamics. *International Journal for Numerical Methods in Engineering*, 61(13):2183–2204, 2004.

[7] L. Gigliotti and S.T. Pinho. Multiple length/time-scale simulation of localized damage in composite structures using a mesh superposition technique. *Composite Structures*, 121:395–405, 2015.

[8] S. Ghosh, J. Bai, and P. Raghavan. Concurrent multi-level model for damage evolution in microstructurally debonding composites. *Mechanics of Materials*, 39(3):241–266, 2007.

[9] N.E. Wiberg and X. Li. Adaptive finite element procedures for linear and non-linear dynamics. *International Journal for Numerical Methods in Engineering*, 46(10):1781–1802, 1999.

[10] O.C. Zienkiewicz and J.Z. Zhu. The superconvergent patch recovery and a posteriori error estimates. part 2: Error estimates and adaptivity. *International Journal for Numerical Methods in Engineering*, 33(7):1365–1382, 1992.

[11] D.Y. Kwak and Y.T. Im. Remeshing for metal forming simulations. part ii: Three-dimensional hexahedral mesh generation. *International Journal for Numerical Methods in Engineering*, 53(11):2501–2528, 2002.

[12] T. Belytschko, K. Liu, W, B. Moran, and K. Elkhodary. *Nonlinear Finite Elements for Continua and Structures*. John Wiley & Sons, 2013.

[13] Z.P. Bažant and Z. Celep. Spurious reflection of elastic waves in nonuniform meshes of constant and linear strain unite elements. *Computers & Structures*, 15(4):451–459, 1982.

[14] S.P. Xiao and T. Belytschko. A bridging domain method for coupling continua with molecular dynamics. *Computer Methods in Applied Mechanics and Engineering*, 193(17):1645–1669, 2004.

[15] W.J.T. Daniel. A study of the stability of subcycling algorithms in structural dynamics. *Computer Methods in Applied Mechanics and Engineering*, 156(1-4):1–13, 1998.

[16] J.L. Auriault. Heterogeneous medium. is an equivalent macroscopic description possible? *International Journal of Engineering Science*, 29(7):785–795, 1991.

[17] W. Voigt. Ueber die beziehung zwischen den beiden elasticitätsconstanten isotroper körper. *Annalen der Physik*, 274(12):573–587, 1889.

[18] A. Reuss. Berechnung der fließgrenze von mischkristallen auf grund der plastizitätsbedingung für einkristalle. *ZAMM-Journal of Applied Mathematics and Mechanics/Zeitschrift für Angewandte Mathematik und Mechanik*, 9(1):49–58, 1929.

[19] J.D. Eshelby. The determination of the elastic field of an ellipsoidal inclusion, and related problems. In *Proceedings of the Royal Society of London A: Mathematical, Physical and Engineering Sciences*, volume 241, pages 376–396. The Royal Society, 1957.

[20] Z. Hashin and S. Shtrikman. A variational approach to the theory of the elastic behaviour of multiphase materials. *Journal of the Mechanics and Physics of Solids*, 11(2):127–140, 1963.

[21] R1 Hill. A self-consistent mechanics of composite materials. *Journal of the Mechanics and Physics of Solids*, 13(4):213–222, 1965.

[22] S. Nemat-Nasser and M. Hori. *Micromechanics: overall properties of heterogeneous materials*, volume 37. Elsevier, 2013.

[23] Z. Hashin. Analysis of composite materials. *Journal of Applied Mechanics*, 50(2):481–505, 1983.

[24] R. Hill. Continuum micro-mechanics of elastoplastic polycrystals. *Journal of the Mechanics and Physics of Solids*, 13(2):89–101, 1965.

[25] F. Feyel and J. Chaboche. Fe 2 multiscale approach for modelling the elastoviscoplastic behaviour of long fibre sic/ti composite materials. *Computer Methods in Applied Mechanics and Engineering*, 183(3):309–330, 2000.

[26] K. Matsui, K. Terada, and K. Yuge. Two-scale finite element analysis of heterogeneous solids with periodic microstructures. *Computers & Structures*, 82(7):593–606, 2004.

[27] C. McVeigh, F. Vernerey, W.K. Liu, and L.C. Brinson. Multiresolution analysis for material design. *Computer Methods in Applied Mechanics and Engineering*, 195(37):5053–5076, 2006.

[28] I. Temizer and T.I. Zohdi. A numerical method for homogenization in non-linear elasticity. *Computational Mechanics*, 40(2):281–298, 2007.

[29] I. Temizer and P. Wriggers. On the computation of the macroscopic tangent for multiscale volumetric homogenization problems. *Computer Methods in Applied Mechanics and Engineering*, 198(3):495–510, 2008.

[30] M. Hain and P. Wriggers. Computational homogenization of micro-structural damage due to frost in hardened cement paste. *Finite Elements in Analysis and Design*, 44(5):233–244, 2008.

[31] Z. Yuan and J. Fish. Toward realization of computational homogenization in practice. *International Journal for Numerical Methods in Engineering*, 73(3):361–380, 2008.

[32] E. Bosco, V.G. Kouznetsova, E.W.C. Coenen, M.G.D. Geers, and A. Salvadori. A multiscale framework for localizing microstructures towards the onset of macroscopic discontinuity. *Computational Mechanics*, 54(2):299–319, 2014.

[33] E. Bosco, V.G. Kouznetsova, and M.G.D. Geers. Multi-scale computational homogenization–localization for propagating discontinuities using x-fem. *International Journal for Numerical Methods in Engineering*, 102(3-4):496–527, 2015.

[34] T.P. Fries and T. Belytschko. The extended/generalized finite element method: an overview of the method and its applications. *International Journal for Numerical Methods in Engineering*, 84(3):253–304, 2010.

[35] T. Belytschko, R. Gracie, and G. Ventura. A review of extended/generalized finite element methods for material modeling. *Modelling and Simulation in Materials Science and Engineering*, 17(4):043001, 2009.

[36] S. Loehnert and T. Belytschko. A multiscale projection method for macro/microcrack simulations. *International Journal for Numerical Methods in Engineering*, 71(12):1466–1482, 2007.

[37] K. Matouš, M.G.D. Geers, V.G. Kouznetsova, and A. Gillman. A review of predictive nonlinear theories for multiscale modeling of heterogeneous materials. *Journal of Computational Physics*, 330:192–220, 2017.

[38] C. Farhat and F.X. Roux. A method of finite element tearing and interconnecting and its parallel solution algorithm. *International Journal for Numerical Methods in Engineering*, 32(6):1205–1227, 1991.

[39] C. Farhat, J. Mandel, and F.X. Roux. Optimal convergence properties of the feti domain decomposition method. *Computer Methods in Applied Mechanics and Engineering*, 115(3-4):365–385, 1994.

[40] P. Kerfriden, O. Allix, and P. Gosselet. A three-scale domain decomposition method for the 3d analysis of debonding in laminates. *Computational Mechanics*, 44(3):343–362, 2009.

[41] M. Hautefeuille, J.B. Colliat, A. Ibrahimbegovic, H.G. Matthies, and P. Villon. A multi-scale approach to model localized failure with softening. *Computers & Structures*, 94:83–95, 2012.

[42] T. Zohdi and P. Wriggers. A domain decomposition method for bodies with heterogeneous microstructure basedon material regularization. *International Journal of Solids and Structures*, 36(17):2507–2525, 1999.

[43] I.M. Gitman, H. Askes, and L.J. Sluys. Coupled-volume multi-scale modelling of quasi-brittle material. *European Journal of Mechanics-A/Solids*, 27(3):302–327, 2008.

[44] H.B. Dhia and G. Rateau. The arlequin method as a flexible engineering design tool. *International Journal for Numerical Methods in Engineering*, 62(11):1442–1462, 2005.

[45] P.A. Guidault and T. Belytschko. On the l2 and the h1 couplings for an overlapping domain decomposition method using lagrange multipliers. *International Journal for Numerical Methods in Engineering*, 70(3):322–350, 2007.

[46] P.T. Bauman, H.B. Dhia, N. Elkhodja, J.T. Oden, and S. Prudhomme. On the application of the arlequin method to the coupling of particle and continuum models. *Computational Mechanics*, 42(4):511–530, 2008.

[47] P.T. Bauman, J.T. Oden, and S. Prudhomme. Adaptive multiscale modeling of polymeric materials with arlequin coupling and goals algorithms. *Computer Methods in Applied Mechanics and Engineering*, 198(5):799–818, 2009.

[48] S. Prudhomme, H.B. Dhia, P.T. Bauman, N. Elkhodja, and J.T. Oden. Computational analysis of modeling error for the coupling of particle and continuum models by the arlequin method. *Computer Methods in Applied Mechanics and Engineering*, 197(41):3399–3409, 2008.

[49] A.C. Eringen and E.S. Suhubi. Nonlinear theory of simple micro-elastic solidsâĂŤi. *International Journal of Engineering Science*, 2(2):189–203, 1964.

[50] K. Pham, V.G. Kouznetsova, and M.G.D. Geers. Transient computational homogenization for heterogeneous materials under dynamic excitation. *Journal of the Mechanics and Physics of Solids*, 61(11):2125–2146, 2013.

[51] E.A. De Souza Neto, P.J. Blanco, P.J. Sánchez, and R.A. Feijóo. An rve-based multiscale theory of solids with micro-scale inertia and body force effects. *Mechanics of Materials*, 80:136–144, 2015.

[52] A. Sridhar, V.G. Kouznetsova, and M.G.D. Geers. Homogenization of locally resonant acoustic metamaterials towards an emergent enriched continuum. *Computational Mechanics*, 57(3):423–435, 2016.

[53] M.C.C. Bampton and Roy R. Craig, J.R. Coupling of substructures for dynamic analyses. *AIAA Journal*, 6(7):1313–1319, 1968.

[54] T. Belytschko and R. Mullen. Stability of explicit-implicit mesh partitions in time integration. *International Journal for Numerical Methods in Engineering*, 12(10):1575–1586, 1978.

[55] T. Belytschko, H-J Yen, and R. Mullen. Mixed methods for time integration. *Computer Methods in Applied Mechanics and Engineering*, 17:259–275, 1979.

[56] M.O. Neal and T. Belytschko. Explicit-explicit subcycling with non-integer time step ratios for structural dynamic systems. *Computers & Structures*, 31(6):871–880, 1989.

[57] M. Klisinski and A. Moström. On stability of multitime step integration procedures. *Journal of Engineering Mechanics*, 124(7):783–793, 1998.

[58] Y.S. Wu and P. Smolinski. A multi-time step integration algorithm for structural dynamics based on the modified trapezoidal rule. *Computer Methods in Applied Mechanics and Engineering*, 187(3-4):641–660, 2000.

[59] W.J.T. Daniel. Subcycling first-and second-order generalizations of the trapezoidal rule. *International Journal for Numerical Methods in Engineering*, 42(6):1091–1119, 1998.

[60] F. Casadei and J. Halleux. Binary spatial partitioning of the central-difference time integration scheme for explicit fast transient dynamics. *International Journal for Numerical Methods in Engineering*, 78(12):1436–1473, 2009.

[61] C. Farhat, L. Crivelli, and F.X. Roux. A transient feti methodology for large-scale parallel implicit computations in structural mechanics. *International Journal for Numerical Methods in Engineering*, 37(11):1945–1975, 1994.

[62] A. Gravouil and A. Combescure. Multi-time-step explicit–implicit method for non-linear structural dynamics. *International Journal for Numerical Methods in Engineering*, 50(1):199–225, 2001.

[63] N. Mahjoubi, A. Gravouil, A. Combescure, and N. Greffet. A monolithic energy conserving method to couple heterogeneous time integrators with incompatible time steps in structural dynamics. *Computer Methods in Applied Mechanics and Engineering*, 200(9):1069–1086, 2011.

[64] O. Bettinotti, O. Allix, and B. Malherbe. A coupling strategy for adaptive local refinement in space and time with a fixed global model in explicit dynamics. *Computational Mechanics*, 53(4):561–574, 2014.

[65] A. Gravouil, A. Combescure, and M. Brun. Heterogeneous asynchronous time integrators for computational structural dynamics. *International Journal for Numerical Methods in Engineering*, 102(3-4):202–232, 2015.

[66] N. Holmes and T. Belytschko. Postprocessing of finite element transient response calculations by digital filters. *Computers & Structures*, 6(3):211–216, 1976.

[67] Zdeněk P. BazÌĘant. Spurious reflection of elastic waves in nonuniform finite element grids. *Computer Methods in Applied Mechanics and Engineering*, 16(1):91–100, 1978.

[68] J. Marchais, L. Chamoin, and C. Rey. Wave filtering through a selective perfectly matched layer in multiscale couplings with dynamically incompatible models. *International Journal for Numerical Methods in Engineering*, 110(8):745–775, 2016.

[69] J.P. Berenger. A perfectly matched layer for the absorption of electromagnetic waves. *Journal of Computational Physics*, 114(2):185–200, 1994.

[70] F. Collino and P.B. Monk. Optimizing the perfectly matched layer. *Computer Methods in Applied Mechanics and Engineering*, 164(1-2):157–171, 1998.

[71] A. Ghanem, M. Torkhani, N. Mahjoubi, T.N. Baranger, and A. Combescure. Arlequin framework for multi-model, multi-time scale and heterogeneous time integrators for structural transient dynamics. *Computer Methods in Applied Mechanics and Engineering*, 254:292–308, 2013.

[72] A. Fernier, V. Faucher, and O. Jamond. Multi-model arlequin method for transient structural dynamics with explicit time integration. *International Journal for Numerical Methods in Engineering*, 112(9):1194–1215, 2017.

[73] H. Talebi, M. Silani, S.P.A. Bordas, P. Kerfriden, and T. Rabczuk. Molecular dynamics/xfem coupling by a three-dimensional extended bridging domain with applications to dynamic brittle fracture. *International Journal for Multiscale Computational Engineering*, 11(6):527–541, 2013.

[74] S. Ghosh, K. Lee, and S. Moorthy. Multiple scale analysis of heterogeneous elastic structures using homogenization theory and voronoi cell finite element method. *International Journal of Solids and Structures*, 32(1):27–62, 1995.

[75] F.J. Vernerey and M. Kabiri. An adaptive concurrent multiscale method for microstructured elastic solids. *Computer Methods in Applied Mechanics and Engineering*, 241:52–64, 2012.

[76] F. Larsson and K. Runesson. On two-scale adaptive fe analysis of micro-heterogeneous media with seamless scale-bridging. *Computer Methods in Applied Mechanics and Engineering*, 200(37):2662–2674, 2011.

[77] F. Greco, L. Leonetti, P. Lonetti, and P.N. Blasi. Crack propagation analysis in composite materials by using moving mesh and multiscale techniques. *Computers & Structures*, 153:201–216, 2015.

[78] Ahmad Akbari R., P. Kerfriden, and S. Bordas. Scale selection in nonlinear fracture mechanics of heterogeneous materials. *Philosophical Magazine*, 95(28-30):3328–3347, 2015.

[79] O.C. Zienkiewicz and J.Z. Zhu. A simple error estimator and adaptive procedure for practical engineerng analysis. *International Journal for Numerical Methods in Engineering*, 24(2):337–357, 1987.

[80] I. Temizer and P. Wriggers. An adaptive multiscale resolution strategy for the finite deformation analysis of microheterogeneous structures. *Computer Methods in Applied Mechanics and Engineering*, 200(37):2639–2661, 2011.

[81] O.C. Zienkiewicz and Y.M. Xie. A simple error estimator and adaptive time stepping procedure for dynamic analysis. *Earthquake engineering & structural dynamics*, 20(9):871–887, 1991.

[82] N.E. Wiberg and X.D. Li. A postprocessed error estimate and an adaptive procedure for the semidiscrete finite element method in dynamic analysis. *International Journal for Numerical Methods in Engineering*, 37(21):3585–3603, 1994.

[83] I. Romero and L.M. Lacoma. A methodology for the formulation of error estimators for time integration in linear solid and structural dynamics. *International Journal for Numerical Methods in Engineering*, 66(4):635–660, 2006.

[84] Z. Yue and D.H. Robbins. Adaptive superposition of finite element meshes in elastodynamic problems. *International Journal for Numerical Methods in Engineering*, 63(11):1604–1635, 2005.

[85] Z. Yue and D.H. Robbins. Adaptive superposition of finite element meshes in non-linear transient solid mechanics problems. *International Journal for Numerical Methods in Engineering*, 72(9):1063–1094, 2007.

[86] R. Gracie and T. Belytschko. An adaptive concurrent multiscale method for the dynamic simulation of dislocations. *International Journal for Numerical Methods in Engineering*, 86(4-5):575–597, 2011.

[87] P. Moseley, J. Oswald, and T. Belytschko. Adaptive atomistic-to-continuum modeling of propagating defects. *International Journal for Numerical Methods in Engineering*, 92(10):835–856, 2012.

[88] D. Peric, C. Hochard, M. Dutko, and D.R.J. Owen. Transfer operators for evolving meshes in small strain elasto-placticity. *Computer Methods in Applied Mechanics and Engineering*, 3(137):331–344, 1996.

[89] P.H. Saksono and D. Perić. On finite element modelling of surface tension variational formulation and applications–part i: Quasistatic problems. *Computational Mechanics*, 38(3):265–281, 2006.

[90] M. Ortiz and J.J. Quigley. Adaptive mesh refinement in strain localization problems. *Computer Methods in Applied Mechanics and Engineering*, 90(1-3):781–804, 1991.

[91] P. Bussetta, R. Boman, and J.P. Ponthot. Efficient 3d data transfer operators based on numerical integration. *International Journal for Numerical Methods in Engineering*, 102(3-4):892–929, 2015.

[92] Klaus-Jürgen Bathe. *Finite element procedures*. Klaus-Jurgen Bathe, 2006.

[93] T.J.R. Hughes, K.S. Pister, and R.L. Taylor. Implicit-explicit finite elements in nonlinear transient analysis. *Computer Methods in Applied Mechanics and Engineering*, 17:159–182, 1979.

[94] Mei Xu and Ted Belytschko. Conservation properties of the bridging domain method for coupled molecular/continuum dynamics. *International Journal for Numerical Methods in Engineering*, 76(3):278–294, 2008.

[95] T. Grätsch and K.J. Bathe. A posteriori error estimation techniques in practical finite element analysis. *Computers & Structures*, 83(4):235–265, 2005.

[96] M.M. Hrabok and T.M. Hrudey. A review and catalogue of plate bending finite elements. *Computers & Structures*, 19(3):479–495, 1984.

[97] Ari Adini. *Analysis of shell strutures by the finite element method*. University of California, Berkeley, 1961.

[98] G.T. Camacho and M. Ortiz. Adaptive lagrangian modelling of ballistic penetration of metallic targets. *Computer Methods in Applied Mechanics and Engineering*, 142(3-4):269–301, 1997.

[99] Fubin Tu, Daosheng Ling, Lingfang Bu, and Qingda Yang. Generalized bridging domain method for coupling finite elements with discrete elements. *Computer Methods in Applied Mechanics and Engineering*, 276:509–533, 2014.

[100] E Oran Brigham. *The fast Fourier transform and its applications*, volume 448.

[101] D.P. Flanagan and T. Belytschko. A uniform strain hexahedron and quadrilateral with orthogonal hourglass control. *International Journal for Numerical Methods in Engineering*, 17(5):679–706, 1981.

[102] R. Schneiders. A grid-based algorithm for the generation of hexahedral element meshes. *Engineering with Computers*, 12(3-4):168–177, 1996.

[103] T. Belytschko and M. Tabbara. H-adaptive finite element methods for dynamic problems, with emphasis on localization. *International Journal for Numerical Methods in Engineering*, 36(24):4245–4265, 1993.

[104] H.P. Bui, S. Tomar, H. Courtecuisse, S. Cotin, and S. Bordas. Real-time error control for surgical simulation. *IEEE Transactions on Biomedical Engineering*, 2017.

[105] W.W. Chen and B. Song. *Split Hopkinson (Kolsky) bar: design, testing and applications*. Springer Science & Business Media, 2010.

[106] R. Gerlach, C. Kettenbeil, and N. Petrinic. A new split hopkinson tensile bar design. *International Journal of Impact Engineering*, 50:63–67, 2012.

[107] B.T. Spencer Cousins. *Development of Improved Numerical Techniques for High Strain Rate Deformation Behaviour of Titanium Alloys*. PhD thesis, University of Oxford, 2016.

[108] Ver ABAQUS. 6.14 documentation. *Dassault Systemes Simulia Corporation*, 2014.